Unraveling the synthesis, structure, and properties of nanoscale zirconia

Inauguraldissertation

zur

Erlangung der Würde eines Doktors der Philosophie

vorgelegt der

Philosophisch-Naturwissenschaftlichen Fakultät

der Universität Basel

von

Rohan Pokratath

aus Indien

2023

Genehmigt von der Philosophisch-Naturwissenschaftlichen Fakultät

auf Antrag von

Erstbetreuer: Prof. Dr. Jonathan De Roo

Zweitbetreuerin: Prof. Dr. Catherine Housecroft

Externer Expertin: Prof. Dr. Delia Milliron

Basel, den 20.06.2023 Prof. Dr. Marcel Mayor (Dekan)

Acknowledgements

Life is a process of continuous learning. Starting from the moment of our birth, we begin to explore and understand the world around us, gaining new skills, knowledge, and experiences that shape our perspectives and behavior. I dedicate my dissertation to all those who have contributed to my own learning experience.

In my opinion, the Ph.D. experience heavily relies on the supervisor, and I consider myself fortunate to have had Jonathan as mine. I am deeply appreciative of him for providing me with the opportunity and for his valuable guidance and support throughout my Ph.D. studies. His insightful feedback and constructive criticism played a pivotal role in shaping my research project and refining my academic skills. I sincerely want to convey my gratitude to my second supervisor Catherine, for her consistent encouragement and support. Even though our interactions were limited, I genuinely appreciated our yearly meetings and conversations. The development of my skill set for performing PDF analysis was a critical component of my Ph.D. studies, and I credit my success in this area to the guidance of Simon. I am extremely grateful to him for welcoming me into his group at Columbia University, introducing me to the field of synchrotron science, and teaching me how to tackle complex structural problems in materials.

I am deeply grateful for the invaluable contributions of my collaborators to this thesis. Their expertise, dedication, and willingness to collaborate have been pivotal in achieving our shared goals. I want to express my gratitude to Kirsten for her support in beamline proposals, data analysis, and fruitful discussions. I am also grateful to her students Jette and Susan for their contributions. Our beamtime during COVID was an enjoyable experience, and I still have the princess with me. Furthermore, I extend my thanks to Benjamin and Laurent for their efforts in measuring and analyzing a significant amount of our samples. Their contributions were essential in making my research a success. I also want to express my appreciation to Gustau and Kumara for their support in characterizing

ferroelectricity, which was crucial in achieving the desired outcomes of my favorite chapter in my thesis. I would like to mention the contributions of Stefano, Valérie, Soham, Songsheng, Mike, Markus, Maryame, and Guillaume to this work. I appreciate their involvement in this project, which significantly enhanced the quality of our results.

I would like to extend my heartfelt gratitude to the members of the De Roo lab for their constant support and encouragement. In particular, I want to extend my gratitude to Dietger, whose assistance and collaboration during the early stages of my research were invaluable. I am also grateful to Ajmal (Aju) for his support inside and outside of work. Your presence and companionship made the process of writing my thesis more manageable, and I am deeply grateful for the quality time we spent together. A special thanks to Mahsa for her support throughout. I really liked your company even though you never liked my Instagram posts. I also want to give a special mention to Nico/Rico for being a great workout buddy and for our meaningful conversations that extended beyond our work. I would like to express my gratitude to my two wonderful lab buddies, Car(lotta) and Jikson (Chickson), who have been great companions and colleagues during my research journey. I also extend my regards to other members of the lab, including Evert, Chris, Ramon, Eline, Liza, Jibin, Leonie, Ale, Antonia, and Loren. I appreciate your contributions to the lab and the positive atmosphere you have created. Special thanks to Isa, Claudia, and Marina for their hard work in dealing with all the administrative tasks and keeping things organized. I am grateful to all the group members for the quality time we spent together during work, lunch breaks, group trips, and parties. A special thanks to the social chair and everyone who brought a delicious cake.

I would like to express my gratitude to the Bilinge group members, including Songsheng, Sani, Emil, Yevgeny, Yang, Tim, Martin, and Berrack, for their warm welcome during my visit. It was a memorable experience to spend time with all of you. Additionally, I extend my thanks to Columbia University for hosting me during my research stay.

I am grateful for the help and support of my other colleagues from the university. I would like to give a special mention to Jasmin, Bjorn, and Polina for being part of the international cooking team and spending free time. I would also like to thank all members of the chemistry football team for playing and spending quality time together. Thanks to PCC for organizing various activities. I am grateful to the Werkstatt team for their constant support. Thanks to Philipp for designing the complicated tools. I extend my sincere appreciation to UniBasel and SNF Eccellenza for funding my research and enabling me to pursue my academic aspirations.

I am thankful to Sabine for her exceptional support and assistance during my time in Basel. Without her help, my life in Basel would have been unbearable. I would also like to express my gratitude to Tobi, Lei, Lara, and Winnie-pooh for the enjoyable moments we shared together. Thank you all so much!

I am immensely grateful to my dear friends Anupa (Chechi), Devi (****), and Blesson (Mallu) for their constant support, presence, and for standing by me through the highs and lows of my Ph.D. journey.

Achan, Amma, and Malu without you, I don't know what will happen to me, but definitely, the journey would have been drastically different. I am at a loss for words to adequately convey the depth of my gratitude towards you. My heartfelt thanks to my cousins Suresh, Ritwik, and Akhil for their support and encouragement.

Finally, I want to thank my partner Geraldine for her unconditional love, unwavering support, and incredible patience throughout our journey. Love you!

Abstract

Energy and memory storage systems are critical components in various applications, ranging from consumer electronics to renewable energy. Research is progressing for enhancing the performance and capabilities of these technologies as well as enabling new applications. Materials exhibiting switchable polarization behaviors such as ferroelectricity have the potential to improve developments in this field. Nanomaterials possess unique physical, chemical, and biological properties that differ from their bulk counterparts, making them attractive for a wide range of applications. Their properties are often determined by size, shape, and structure, so understanding the relationship between synthesis and structure is crucial for optimizing their properties. In this dissertation, we investigate the formation mechanism of zirconia nanocrystals using a powerful combination of X-ray scattering, NMR spectroscopy, quantum chemical calculations, and chromatography. We identify the active precursor species and amorphous intermediate in the reaction mixture. Based on these results, we hypothesized an alternative mechanism for precursor decomposition and nanocrystal formation. By using various precursor combinations, the kinetics of the reaction can be controlled. We demonstrated several strategies for size tuning, which is particularly challenging for group 4 and 5 metal oxides. Furthermore, we carried out a thorough structural characterization of zirconia nanocrystals using pair distribution function analysis. Our findings revealed a distinct local structure distortion in the material. Interestingly the distortion induces switchable polarization properties to ZrO_2.

Contents

List of Figures

List of Tables

Abbreviations

AFM Atomic Force Microscopy.

CIF Crystallographic Information File.

COPASI Complex Pathway Simulator.

CT Computed Tomography.

DC Direct Current.

DFT Density Functional Theory.

diffpy-CMI Diffpy - Complex Modeling Infrastructure.

DLS Dynamic Light Scattering.

FeRAM Ferroelectric Random Access Memory.

FWHM Full Width at Half Maxima.

GC-FID Gas Chromatography - Field Ionization Detection.

HfO_2 Hafnium Dioxide.

ICP Inductively Coupled Plasma.

LED Light Emitting Diode.

NC Nanocrystal.

nm Nanometer.

NMR Nuclear Magnetic Resonance.

PDF Pair Distribution Function.

PDFgui Pair Distribution Function graphical user interface.

RFID Radio Frequency Identification.

RMCProfile Reverse Monte Carlo Profile.

Rw Goodness of the fit.

SAXS Small Angle X-ray Scattering.

SS-PFM Switching Spectroscopy - Piezoelectric Force Microscopy.

TEM Transmission Electron Microscopy.

THF Tetrahydrofuran.

TiO_2 Titanium Dioxide.

TOPO Tri-n-octylphosphine Oxide.

TS Total Scattering.

XRD X-ray Diffraction.

YSZ Yttrium stabilized ZrO_2.

ZrO_2 Zirconium Dioxide.

"When you're curious, you find lots of interesting things to do"

- Walt Disney

Chapter 1

Introduction[†]

1.1 Properties of group 4 metals and their oxides

The group 4 metals share many chemical properties. The +IV oxidation state is predominant for all three metals, but titanium can also be reduced to Ti(+III). This is a recurring theme in group 4. All three are very similar whereas zirconium and hafnium almost react identically, titanium is the odd one out, see Table 1.1. A striking example is the ionic radius, which is 0.74 Å for Ti^{4+} but 0.83 Å and 0.84 Å for Hf^{4+} and Zr^{4+} respectively.[1] The similar size for hafnium and zirconium is ascribed to the lanthanide contraction and enables the formation of solid solutions; $Hf_xZr_{1-x}O_2$.[2] Zirconium and hafnium are often called the *twin metals*. Titanium usually has a coordination number of six, while zirconium and hafnium can reach a coordination number of eight.

Table 1.1 | Properties of the group 4 elements.

	Ti	Zr	Hf
Atomic number	22	40	72
Atomic radius (pm)[3]	140	155	155
Ionic radius (pm)[1]	74	84	83
Electronegativity (Pauling)[4]	1.54	1.33	1.3
Electronegativity (corrected)[5]	2.23	2.05	2.01
Maximum coordination number	6	8	8

The standard formation Gibbs free energy of all three oxides is highly negative and becomes more negative down the group, see Table 1.2. The oxides have also very high melting points, high dielectric constants, and high refractive indices. While the band gap of TiO_2 is close to the blue, the

[†]Part of this chapter is adapted from: Nonaqueous Chemistry of Group 4 Oxo Clusters and Colloidal Metal Oxide Nanocrystals. Dietger Van den Eynden, Rohan Pokratath, and Jonathan De Roo*, Chemical Reviews, 122, 11, 10538–10572, 2022, DOI: 10.1021/acs.chemrev.1c01008.

band gap of ZrO_2 and hafnia are deep in the ultraviolet. Given the increasing atomic mass, it is no surprise that the density of the oxides increases down the group.

Table 1.2 | Properties of the group 4 metal oxides.[6–10]

	TiO_2	ZrO_2	HfO_2
Density (g/cm^3)	3.83 (anatase) 4.17 (brookite) 4.24 (rutile)	5.56 (monoclinic) 5.8 (tetragonal) 5.99 (cubic)	9.97 (monoclinic) 10.36 (tetragonal) 10.69 (cubic)
Melting point (°C)	1870	2715	2758
Dielectric constant	80 (rutile)	25 (monoclinic)	25 (monoclinic)
Refractive Index at 632.8 nm	2.8	2.2	1.91
Band Gap (eV)	3 (rutile) 3.2 (anatase)	5.8	5.8
$\Delta G^0_{f,298}$ (kJ/mol)	-891.2	-1042	-1088

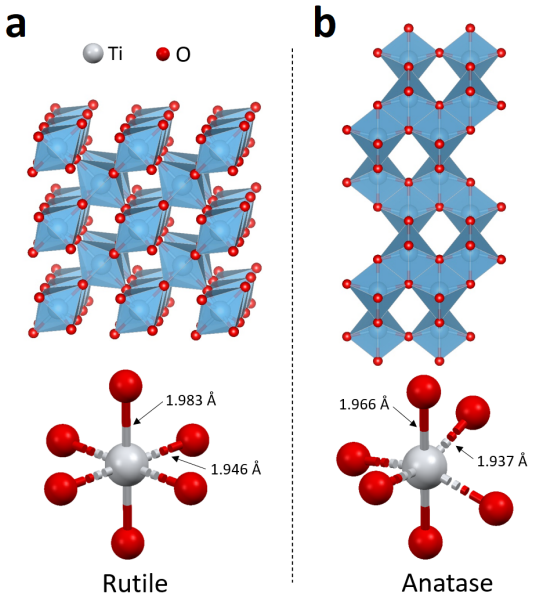

Fig. 1.1 | Structure of TiO_2. Illustration of corner and edge sharing octahedron assembly and Ti-O bond distances in **a** rutile and **b** anatase titanium oxide.

TiO_2 exists in three well-known polymorphs: tetragonal rutile ($P4_2/mnm$), tetragonal anatase ($I4_1/amd$), and orthorhombic brookite (Pbca). In addition, multiple metastable (e.g., the bronze phase) and high-pressure phases have also been reported.[11–18] In all structures, titanium is coordinated by six oxygen atoms with two axial and four equatorial bonds forming a distorted TiO_6 octahedron. These octahedrons build up the crystal lattice by either sharing edges or corners in a specific manner depending on the crystal structure. Fig. 1.1 clearly shows that rutile has more corner sharing compared to anatase where edge sharing is more prevalent. In rutile, the coordination of titanium is close to the D_{4h} symmetry, while in anatase, the octahedron is more distorted. However,

in both cases, we distinguish a longer axial bond and a shorter equatorial bond, with the bonds in rutile being longer than in anatase, see Fig. 1.1.[6] The other polymorphs have different Ti-O bond distances, as well as different octahedron assemblies.

Zirconium and hafnium oxide possess similar properties and are thus called twin oxides. The three most important polymorphs of the twin oxides are: cubic (Fm-3m), tetragonal ($P4_2/nmc$), and monoclinic ($P2_1/c$). The cubic phase is thermodynamically favored at high temperatures and is structurally equivalent to the calcium fluoride structure, see Fig. 1.2. The zirconium/hafnium atoms are eight–coordinated. At lower temperatures (2370-2600 °C, depending on the oxide), a slight distortion happens towards the tetragonal phase, but the metal atoms remain eight–coordinated. At room temperature, the monoclinic phase is most stable and can be considered a highly distorted calcium fluoride structure, see Fig. 1.2. In this monoclinic phase, the metal is seven–coordinate. The tetragonal to monoclinic phase transformation is accompanied by a large volume decrease, causing undesired cracking of the material upon cooling. To avoid the phase transformations during cooling, the cubic phase is often stabilized with dopants such as yttrium. Yttrium stabilized ZrO_2 (YSZ) is one of the prime examples of stabilized ZrO_2 and retains the cubic crystal structure at room temperature. The oxygen vacancies created by yttrium incorporation are leveraged in solid oxide fuels cells and in other catalytic processes.[19]

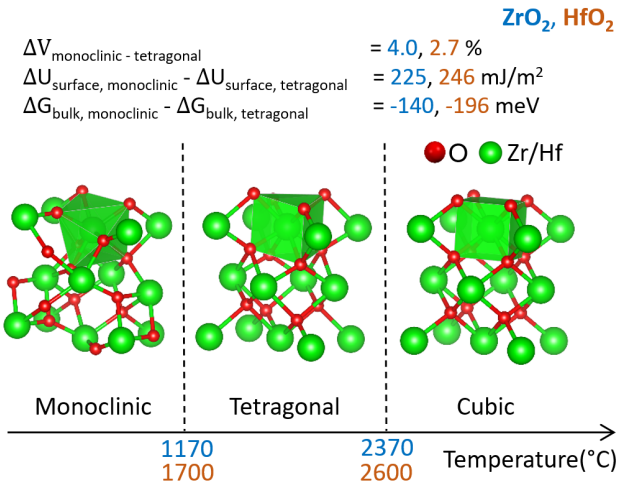

Fig. 1.2 | Phase transformation parameters for ZrO_2 and HfO_2.[20]

Given the significant difference in surface free energy for tetragonal and monoclinic ZrO_2, the tetragonal phase becomes stable at room temperature below a crystal size of 30 nm. Several colloidal syntheses for monodisperse ZrO_2 are indeed in agreement with this predicted critical size.[21,22] Surface

calculations of HfO_2 nanocrystals reported a critical size of 2 - 10 nm.[23–25] A more precise value (4 nm) was determined experimentally by a size tunable method to synthesize HfO_2 nanocrystals.[26]

Stabilizing tetragonal HfO_2 is relevant for its use as a gate dielectric since first principle studies predict that the dielectric constant for tetragonal HfO_2 is about four times the value of monoclinic HfO_2.[27] Even more polymorphs of HfO_2 are known. There are non-polar (centrosymmetric) phases like the cubic phase, but there exist also polar (non-centrosymmetric) phases.[28] These polar phases are responsible for the recently discovered ferroelectric behavior of HfO_2, and they are often stabilized as solid solutions with ZrO_2 or by the inclusion of dopants.[29–32]

1.2 Colloidal nanocrystals and synthetic approaches

Nanoparticles are tiny particles, typically on the scale of 1 to 100 nanometers, that are made up of a large number of atoms or molecules. Due to their small size and high surface area, they can exhibit unique optical, electrical, and magnetic properties and can have a diverse range of shapes and compositions. Depending on the material and synthetic approach, they can be crystalline or amorphous. If they can be uniformly dispersed in a solvent, often by attaching a ligand to the surface of the nanoparticle, called a colloidal nanoparticle. Among colloidal nanoparticles, metal oxide nanoparticles draw less attention likely due to the absence of an optical signature, although they are used in important applications. Since colloidal stability is a major prerequisite for many applications, including in electronics, photonics, catalysis, and biomedicine the synthetic methods to produce colloidally stable nanoparticles are actively researched. They are typically synthesized using wet chemical methods and can be stabilized in solution by a variety of surface ligands. In this section, we discuss the synthetic procedures for group 4 metal oxide nanocrystals by focusing on Zr and Hf. Nonaqueous strategies are very effective in producing highly crystalline oxide nanocrystals. A comprehensive, general overview of the different mechanisms in nonaqueous synthesis is provided elsewhere.[33,34] In the following discussion of group 4 oxide nanocrystals, we make a distinction between surfactant-free and surfactant-assisted strategies. We will discuss synthetic strategies, surface chemistry, and the current level of mechanistic insight.

1.2.1 Nonaqueous surfactant-free synthesis

In the absence of surfactants, nonaqueous chemistry often provides amorphous gels. However, under particular conditions, crystalline nanoparticles can be obtained. Benzyl alcohol turned out to be one of

the most versatile solvents in this respect.[35] A metal precursor is typically dissolved in benzyl alcohol and heated in a pressurized vessel (steel bomb or microwave vessel) and a nanocrystal powder is retrieved at the end of the reaction. Despite the fact that these syntheses result in aggregated powders it is often possible to functionalize the nanocrystal surface with ligands to obtain stable colloidal dispersions with minimal or no residual agglomeration. Stability in nonpolar solvent is typically provided by fatty acids,[36–40] and stability in polar solvents is achieved using 2-[2-(2-methoxyethoxy)ethoxy]acetic acid,[41–43] or 2-aminoethyl phosphoric acid.[44]

ZrO_2 nanocrystals

ZrO_2 NCs have been synthesized *via* an S_N1 nucleophile substitution mechanism. Smarsly *et al.* first synthesized $ZrCl_2(OR)_2$ from $ZrCl_4$ *via* two steps (Equations 1.1-1.2) or from $Zr(OR)_4$ and acetyl chloride.[45]

$$ZrCl_4 + \text{excess ROH} \longrightarrow ZrCl_3OR + HCl \tag{1.1}$$

$$2\,ZrCl_3OR + Zr(OR)_4 \longrightarrow 3\;ZrCl_2(OR)_2 \tag{1.2}$$

The resulting precursor is mixed with hexanol and benzyl alcohol and ZrO_2 NCs (2 - 2.5 nm) are formed in a few minutes at 200 °C under microwave radiation. Benzyl chloride was found as the main reaction by-product, confirming the mechanism. Only at an equal ratio of alkoxide to chloride, crystalline material (cubic ZrO_2) was obtained. The nanocrystals are dispersible in water, up to 45 wt% ZrO_2.

ZrO_2 NCs are also produced on a large scale by reacting $Zr(O\mathit{i}Pr)_4 \cdot \mathit{i}PrOH$ in benzyl alcohol for 2 days at 210 °C.[36,39] Benzyl ether and isopropanol were detected by NMR as the main reaction by–products, suggesting ligand exchange as a first step.

$$Zr(O\mathit{i}Pr)_4 + x\,BnOH \longrightarrow Zr(O\mathit{i}Pr)_{4-x}(OBn)_x + x\,\mathit{i}PrOH \tag{1.3}$$

In the second step, the alkoxide groups condense to form the oxide.

$$Zr{-}OBn + BnO{-}Zr \longrightarrow Zr{-}O{-}Zr + Bn{-}O{-}Bn \tag{1.4}$$

After synthesis, the particles can be easily dispersed in nonpolar solvents by the addition of carboxylic acids, e.g., octadecanoic acid. Using $Zr(O\mathit{i}Pr)_4$, the NCs are 3 - 4 nm in size and have a cubic

crystal structure. However, using the cheaper $Zr(OnPr)_4$ (70 w% in propanol), the NCs are 4.5 nm and a mixture of tetragonal and monoclinic ZrO_2.[42] The monoclinic fraction can be minimized by performing the reaction at 270 °C but the resulting particles cannot be dispersed with carboxylic acids. A note is in order regarding the distinction between the cubic and tetragonal phases of ZrO_2. Due to the broadening of the reflections, XRD cannot make the distinction, and other techniques such as Raman spectroscopy,[42] or X-ray Pair Distribution Function (PDF) analysis are required.[46] It is likely that most (if not all) of the cubic phases that are mentioned in this section are actually tetragonal.

The reaction of $Zr(OiPr)_4$ in benzyl alcohol can be accelerated under microwave heating and reaches full yield after 4 hours at 270 °C.[38] Here, 4 nm tetragonal (or cubic) ZrO_2 is obtained. At 230 °C, $Zr(OiPr)_4$, $Zr(OEt)_4$, or $Zr(OAc)_4$ yield tetragonal ZrO_2 while $ZrCl_4$ yields monoclinic ZrO_2. The difference in crystal structure was ascribed to the presence of HCl in the latter reaction mixture.[38] The presence of water can also steer the outcome of the synthesis and is even capable of transforming tetragonal ZrO_2 NCs into monoclinic NCs upon prolonged heat treatment at 210 °C.[47] Small amounts of water, generated by ZrO_2–catalyzed alcohol dehydration, cause monoclinic impurities in the final product. By adding sodium as a desiccant to the reaction mixture, phase pure tetragonal ZrO_2 was obtained.

HfO_2 nanocrystals

Monoclinic HfO_2 NCs were synthesized from $Hf(OEt)_4$ in benzyl alcohol at 200 °C. The NCs are ellipsoidal with a long axis of around 6 nm and a short axis of 3 nm. The by-products are mainly dibenzyl ether, with trace amounts of ethyl benzyl ether.[48] Diethyl ether was not detected. Therefore, it was concluded that the first step in this mechanism is ligand exchange between ethoxide and benzyl alcohol.

$$Hf(OEt)_4 + x\,BnOH \longrightarrow Hf(OEt)_{4-x}(OBn)_x + x\,EtOH \tag{1.5}$$

In the second step, the alkoxide groups condense to form the oxide.

$$Hf{-}OR + RO{-}Hf \longrightarrow Hf{-}O{-}Hf + R{-}O{-}R \tag{1.6}$$

Primary alcohols are ideal substrates for S_N2 reactions and benzyl alcohol is both reactive in a S_N1 and S_N2 mechanism. Since the ethyl ethers were hardly observed, the condensation reaction most likely proceeds through an S_N1 mechanism.

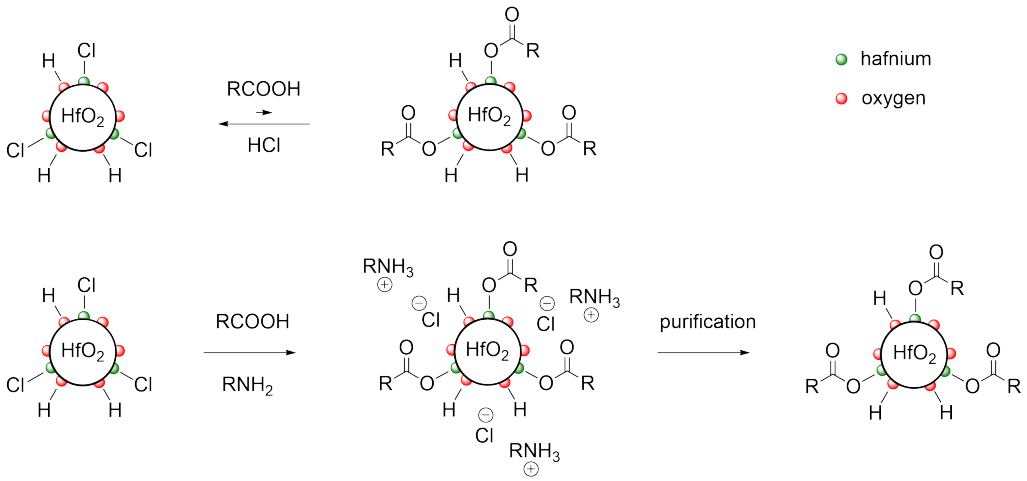

Fig. 1.3 | The exchange of HCl for carboxylic acids is unfavorable due to the pKa difference. By adding a base (amine), the proton transfer step is eliminated and carboxylate can replace chloride.

When $Hf(OtBu)_4$ is heated in benzyl alcohol at 300 °C, 3 nm monoclinic HfO_2 is obtained after 48 hours.[49] Similar particles (4 nm) are obtained by heating the mixture at 220 °C for 4 days.[43] When the same precursor is heated in benzylamine, 2.6 nm cubic HfO_2 is obtained.[49] Given the absence of an ether elimination mechanism in benzylamine, we speculate that the oxide is formed by an E1 mechanism. The oxygen deficient reaction mixture is most likely responsible for oxygen vacancies and thus stabilization of the cubic phase.

The synthesis of monoclinic HfO_2 NCs from $HfCl_4$ in benzyl alcohol at 220 °C also delivers large quantities of dibenzyl ether.[50,51] The process probably involves a ligand exchange, releasing HCl.

$$HfCl_4 + x\,BnOH \longrightarrow HfCl_{4-x}(OBn)_x + x\,HCl \tag{1.7}$$

The formed alkoxo ligands can undergo an ether elimination condensation. However, it cannot be fully excluded that benzyl chloride was transiently formed and subsequently reacted with benzyl alcohol to dibenzyl ether and HCl. The large excess of ether (up to 80% of the final reaction mixture) is due to the Williamson ether synthesis, catalyzed by HCl. When the reaction is performed over three days with conventional heating in a pressure bomb, the nanocrystals are slightly larger (5 nm) compared to three hours of microwave heating (4 nm).[50] In both cases, full yield was achieved. After microwave synthesis, the nanocrystal aggregates can be dispersed in ethanol or water, since they are charge stabilized by HCl (produced during synthesis). The aggregates can be broken up in chloroform by a combination of carboxylic acid ligands and a suitable base. The base is necessary to remove the initially present HCl from the surface. In nonpolar solvents, HCl cannot be displaced by carboxylic acids

because HCl is a stronger acid. However, under basic conditions, the carboxylate anion outcompetes the chloride ligand (Fig. 1.3).[37,52]

1.2.2 Nonaqueous surfactant-assisted synthesis

Surfactant-assisted syntheses generally lead to the highest quality of nanocrystals, especially regarding polydispersity and colloidal stability. For group 4, a popular and powerful strategy involves the reaction of metal halides with metal alkoxides in tri-*n*-octylphosphine oxide above 300 °C (Table 1.3). Other methods are typically based on nucleophilic substitution (ester or amide formation).

Table 1.3 | Synthetic procedures to synthesize group 4 oxide nanocrystal via surfactant assisted reactions between metal chloride and metal alkoxides.

MO_2	surfactant	Precursors	[M] (mol/kg)	Temp.	time	crystal phase	size (nm)	Ref
ZrO_2	5.8 eq TOPO	$ZrCl_4$ + $Zr(OiPr)_4$	0.45	340 °C	2 h	tetragonal	4.0	22
ZrO_2	5.8 eq TOPO	$ZrBr_4$ + $Zr(OiPr)_4$	0.45	340 °C	2 h	tetragonal	3.0	22
ZrO_2	5.8 eq TOPO	$ZrCl_4$ + $Zr(OiPr)_4$	0.45	340 °C	2 h	tetragonal	4.0	53
ZrO_2	5.8 eq TOPO	$ZrCl_4$ + $Zr(OiPr)_4$	0.45	340 °C	2.5 h	tetragonal	3.7	54
ZrO_2	6.5 eq TOPO	$ZrCl_4$ + $Zr(OiPr)_4$	0.4	340 °C	2 h	tetragonal	4.0	22
HfO_2	6.5 eq TOPO	$HfCl_4$ + $Hf(OiPr)_4$	0.4	360 °C	2 h	tetragonal[b]	5.5	2
HfO_2	6.5 eq TOPO	$HfCl_4$ + $Hf(OiPr)_4$	0.4	400 °C	2 h	monoclinic	3.4 × 7.6	2
HfO_2	6.5 eq TOPO	$HfBr_4$ + $Hf(OiPr)_4$	0.4	360 °C	2 h	monoclinic	3.7	2
HfO_2	6.5 eq TOPO	$HfCl_4$ + $Hf(OiPr)_4$	0.4	340 °C	2 h	monoclinic	2.4 × 6.9	21
HfO_2	6.5 eq TOPO	$HfCl_4$ + $Hf(OtBu)_4$	0.4	340 °C	2 h	monoclinic	2.3 × 13	20
HfO_2	6.5 eq TOPO	$HfCl_4$ + $Hf(OiPr)_4$	0.4	360 °C	2 h	monoclinic	3.5 × 9.2	55
HfO_2	1.5 eq OLAm	$HfCl_4$ + $Hf(OiPr)_4$	0.4	315 °C	2 h	monoclinic	2.6 × 10.5	55
HfO_2 : Ce	6.5 eq TOPO	$HfCl_4$ + $Ce(OtBu)_4$	0.4	340 °C	2 h	tetragonal	3.1	26
HfO_2 : La	6.5 eq TOPO	$HfCl_4$ + $La(OiPr)_4$	0.4	340 °C	2 h	tetragonal	3.3	26
$Zr_xHf_{1-x}O_2$	6.5 eq TOPO	$ZrCl_4$ + $Hf(OiPr)_4$	0.4	360 °C	2 h	tetragonal	4.3	2
$Zr_xHf_{1-x}O_2$	6.5 eq TOPO	$HfCl_4$ + $Zr(OiPr)_4$	0.4	360 °C	2 h	tetragonal	4.6	2
$Zr_xHf_{1-x}O_2$	6.5 eq TOPO	$HfCl_4$ + $Zr(OiPr)_4$	0.4	340 °C	2 h	tetragonal	5.6	21
$Zr_xHf_{1-x}O_2$	6.5 eq TOPO	$ZrCl_4$ + $Hf(OiPr)_4$	0.4	340 °C	2 h	tetragonal	5.6	21
$Zr_xHf_{1-x}O_2$	6.5 eq TOPO	$HfCl_4$ + $Zr(OtBu)_4$	0.4	340 °C	2 h	monoclinic	2.5 × 5.7	21
$Zr_xHf_{1-x}O_2$	6.5 eq TOPO	$ZrCl_4$ + $Hf(OtBu)_4$	0.4	340 °C	2 h	monoclinic	2.8 × 5.1	21

[a] with a small rutile impurity [b] with a small monoclinic impurity

Zirconium oxide nanocrystals

$ZrCl_4$ and $Zr(OiPr)_4 \cdot iPrOH$ complex are dissolved at 80 °C in pure, molten TOPO and heated to 340 °C for 2 hours to form 4 nm ZrO_2 NCs, see Fig. 1.4.[22] Smaller nanocrystals are obtained with $ZrBr_4$ (3 nm). While originally $ZrCl_4$ was used,[22] its polymeric structure causes irreproducibility in dissolution and instead the monomeric THF complex was introduced.[53]

$$1.25\ ZrCl_4 + Zr(OiPr)_4 \cdot iPrOH \xrightarrow[TOPO]{0.45\,mol/kg,\ 340\,^\circ C} 2.25\ ZrO_2 + 5\ iPrCl \qquad (1.8)$$

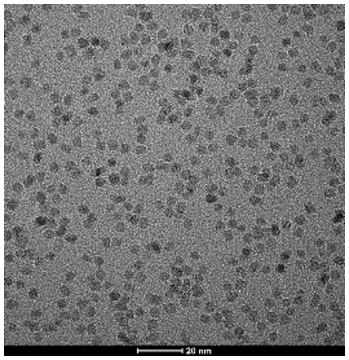

Fig. 1.4 | ZrO_2 nanocrystals synthesized in TOPO from $ZrCl_4$ and zirconium isopropoxide.

Unfortunately, the surface chemistry is highly complex. While it was initially assumed that TOPO was the sole ligand, small amounts of TOPO decompose to potent ligands; dioctylphosphinic acid and P,P'-(dioctyl) pyrophosphonic acid.[2,53] The latter is the self–condensation product of octylphosphonic acid. In addition, the reaction mixture contains large amounts of HCl. Consequently, the surface is covered by HCl, hydrogen bonded TOPO, dissociated dioctylphosphinic acid and deprotonated P,P'-(dioctyl) pyrophosphonate, see Fig. 1.5.[53] Under basic conditions (amine), oleic acid can replace chloride, TOPO, and dioctylphosphinic acid but not P,P'-(dioctyl) pyrophosphonate. A uniform ligand shell could only be obtained by ligand exchange for a phosphonic acid.[53] Phosphonic acids have a much higher binding affinity for oxide surfaces than carboxylic acids.[56]

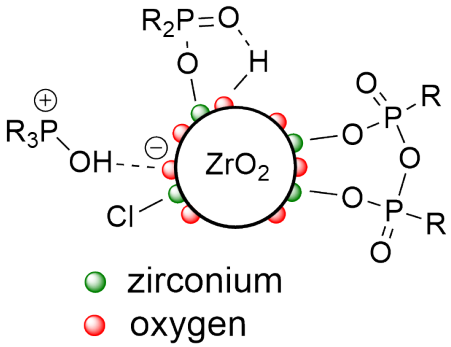

Fig. 1.5 | The surface chemistry of ZrO_2 NCs synthesized via an alkyl halide elimination in TOPO.

Hafnium oxide nanocrystals

HfO_2 nanocrystals were synthesized from $HfCl_4$ and $Hf(OiPr)_4 \cdot iPrOH$ complex in pure TOPO by Brus *et al.*[2] At 360 °C, quasi-spherical 5.5 nm HfO_2 NCs in the tetragonal crystal structure were obtained, although small impurities of monoclinic HfO_2 are present. Similar to the ZrO_2 case, smaller

NCs (3.7 nm) are obtained with $HfBr_4$. In addition, the crystal phase changed to a monoclinic structure. At 400 °C, HfO_2 nanorods (3.4 × 7.6 nm) are formed with the monoclinic crystal structure.[2]

In contrast to the original report of Brus *et al.*, other authors obtained monoclinic HfO_2 nanorods at temperatures varying from 315 - 360 °C.[21,55] Interestingly, the HfO_2 nanorods synthesized in TOPO exhibited paramagnetic behavior due to oxygen defects.[55] The defective nature of the nanorods was confirmed by TEM and UV-Vis (absorption below the band gap energy). Even more defected HfO_2 nanorods with a reduced bandgap were synthesized in octadecene and oleylamine at 315 °C. The latter nanorods feature a strong ferromagnetic component, next to a paramagnetic component, and have strong absorption in UV-Vis around 4.6 and 5.4 eV. Nanocrystals that were annealed at 750 °C displayed diamagnetic character, confirming the relation between oxygen defects and the magnetic properties. No ferromagnetic nanocrystals are obtained when oleic acid is added in addition to oleylamine. This is likely due to a change in the mechanism towards nucleophilic addition elimination. The authors briefly mention that ferromagnetic nanocrystals could be obtained in octadecene or benzyl ether at lower temperatures (200 - 300 °C) but no characterization is provided.[55] A word of caution is in place since octadecene has been shown to polymerize at these reaction temperatures and the resulting polymer impurity is difficult to separate from the formed nanocrystals.[57] Banerjee *et al.* reported the monoclinic crystal structure for different types of alkoxide precursors (Et, *i*Pr, *n*Bu, *t*Bu, 2-Et-Hex).[21] However, they observe large size differences.[20] For the primary alkoxides (Et, *n*Bu), the NCs are very small (2 - 3 nm). With increased branching (*i*Pr, *t*Bu), nanorods are obtained with increased aspect ratio. For $Hf(OtBu)_4$, nanorods 2.3 nm in diameter and 13 nm in length were obtained. The authors report a lower yield for the reaction with hafnium ethoxide compared to $Hf(OtBu)_4$. Therefore, the observed size differences are likely due to the faster kinetics of $Hf(OtBu)_4$. Furthermore, it was possible to grow even longer nanorods (2.9 × 32 nm) by periodically injecting the reaction mixture with small amounts of $Hf(OtBu)_4$ precursor, in an effort to keep the monomer concentration below the nucleation threshold and promote growth.[20] The final ratio of *tert*-butoxide to chloride increase is 10, and this seeded growth mechanism can be rationalized in the same way as for the case of ZrO_2. Structurally, the nanorods consist of multiple crystalline domains, separated by twinning planes. It is believed that the nanocrystals nucleate in the tetragonal structure and undergo a phase transformation upon cooling.[20]

Mixed metal oxide nanocrystals

Given the almost identical ionic radius of Zr^{4+} and Hf^{4+}, HfO_2 and ZrO_2 easily form solid solutions of any composition in bulk. Brus *et al.* synthesized $Hf_xZr_{1-x}O_2$ nanocrystals with compositions varying from x = 0.11 - 0.84 by adjusting the ratio of zirconium and hafnium precursors.[2] Care was taken to balance the number of isopropoxides and halides (disregarding the coordinated isopropanol). ICP analysis shows that the Zr/Hf ratio is consistently higher in the final nanocrystals, compared to the reagent mixture.[2,21] This indicates a higher reactivity of Zr compared to Hf and an incomplete reaction. The incorporation of hafnium seems to depend on the choice of precursor. For example, from an equimolar mixture of $HfCl_4$ and $Zr(OiPr)_4 \cdot iPrOH$, $Hf_xZr_{1-x}O_2$ nanocrystals are obtained with x = 0.35, while for an equimolar mixture of $Hf(OiPr)_4 \cdot iPrOH$ and $ZrCl_4$, x = 0.45.[2]

$Hf_xZr_{1-x}O_2$ NCs with $x < 0.5$ are quasi–spherical and have the tetragonal structure.[2] If $HfBr_4$ or $ZrBr_4$ are used, instead of the chlorides, the particles are smaller and still tetragonal. For $x < 0.5$, the reaction temperature does not have a significant effect on the morphology or phase of the NCs. In contrast, NCs with $x > 0.5$ form in the tetragonal structure at 360 °C, but the NCs are polydisperse and have irregular shapes. At 400 °C, monoclinic nanorods are formed, 3.4 nm in diameter and 7.6 nm in length.[2] Steigerwald *et al.* later explained the tetragonal to monoclinic phase transformation by a Martensitic transformation. In a Martensitic transformation all the atoms in a crystallite move simultaneously, in contrast to diffusion mediated transformations. They argue that tetragonal NCs already form at 340 °C after 10 min, and heating further to 400 °C takes 30 min. Therefore, the monoclinic nanorods must be formed by the transformation of previously formed NCs. The tetragonal to monoclinic transformation is associated with a 4% volume increase, resulting in nanorods with twinned structures.

From the above collection of results, we infer that the precursor conversion follows mostly an S_N1 mechanism for ZrO_2 and HfO_2. Consequently, the rate of the reaction increases with the branching of the alkoxide. Given the slower kinetics of Zr and Hf, this is most likely due to the incomplete reaction of the slower precursors. The nature of the halide has little influence on the rate but changes the NC size and sometimes even the crystal structure. There seems to be some disagreement on the structure of HfO_2 and $Hf_xZr_{1-x}O_2$ NCs, with some authors reporting a tetragonal structure below 360 °C and others a monoclinic structure.

1.3 Nucleation and growth models

It is often hypothesized that the precursor conversion results in a single unit of the final material; the *monomer* (M), see Equation 1.9. This intermediate crystallizes into nanocrystals (NCs) through a process of nucleation and growth. Multiple theories exist pertaining to both nucleation and growth.

$$\mathrm{P} \longrightarrow \mathrm{M} \longrightarrow \mathrm{NC} \tag{1.9}$$

Classical nucleation theory considers the monomer in thermodynamic equilibrium with the formed particles.[58] The activation energy for nucleation depends on the surface energy of the particles, the temperature, and the supersaturation ratio. Studying sulfur sols, Lamer hypothesized that monomers build up in solution, reaching a critical supersaturation, and at this point, particles homogeneously nucleate (infinitely fast).[59,60] This *burst nucleation* is mostly a hypothesis and was recently disproven in the case of Pd, InP, CdSe, and PbS(e) nanocrystals by Small Angle X-ray scattering (SAXS) and UV-Vis spectroscopy.[61–66] Instead, *continuous nucleation* was observed, evidenced by a continuous increase of the particle concentration during the reaction. Continuous nucleation is also the first step in the Finke-Watzky two-step model, although nucleation is considered an irreversible process in FW theory.[67] Interestingly, an order-disorder equilibrium (between an amorphous and crystalline state) was observed by *in situ* TEM during the nucleation of Au nanocrystals, indicating that crystallization is reversible (under those conditions).[68] There were more non-classical nucleation pathways proposed. For example, the surfactant-free aqueous synthesis of calcium phosphate and magnetite involves amorphous pre-nucleation clusters.[69,70] In the surfactant-assisted synthesis of Ni nanocrystals, liquid cell TEM revealed again an amorphous phase.[71] Furthermore, magic-sized clusters with a well-defined structure have been identified in the synthesis of InP nanocrystals as intermediate species between precursors and nanocrystals.[72] Finally, the conversion of iron oleate in iron oxide nanocrystals happens without nucleation. Iron oleate is an iron oxo cluster with three iron atoms connected by a μ_3-oxygen atom.[73] Esterification of the oleate leads to the continuous growth of the precursor into iron oxide nanocrystals, without a separate nucleation step.

Growth models can be constructed from thermodynamic principles where monomers are incorporated into nanocrystals *via* either diffusion-limited growth or reaction-limited growth.[74] While the former is size-focusing (narrowing the size distribution during growth), it appears insufficient to reconcile the monodisperse end product with continuous nucleation. A stronger focusing mechanism

is found by assuming an intrinsic size-dependent growth rate, where small particles grow faster than large particles.[61,62,75] Next, ripening is a growth mechanism where some particles dissolve to provide the necessary monomers for the growth of other particles. Some thermodynamic models consider the final nanocrystal size as an equilibrium product, the size of which is determined by the amount and type of surfactant.[76] In the case of MnO and CdSe nanocrystals, the number of particles decreased over the course of the reaction while the size distribution narrowed (self-focusing).[77,78] Finally, oriented attachment and coalescence are two growth mechanisms that do not involve growth by monomer.[33,79] For example, oriented attachment was observed for ZnO and TiO_2,[80–82] in the absence of ligands, or for ZnS in oleylamine, a weakly bound ligand.[83] Coalescence was shown for Ir and Pt nanocrystals, again with weakly binding ligands.[84,85] Especially in the case of Pt, a detailed TEM analysis showed an initial increase in the number of particles and a subsequent decrease, mostly caused by coalescence and to a minor extent by particle dissolution.[85] Some particles grew by monomer/precursor attachment and others by coalescence. While regular growth immediately formed single-crystalline particles, a polycrystalline particle was initially observed after coalescence. Structural rearrangement took about 16 seconds after coalescence to produce a single crystalline nanocrystal. Irrespective of the mechanism, the nanocrystals stop growing after reaching a certain size (*i.e.*, self-focusing).

Compared to the exhaustively studied semiconductor and metallic systems, little is known about the surfactant-assisted synthesis of group 4 metal oxides. Previous studies only focused on surfactant-free hydrothermal syntheses, where an amorphous material rapidly forms before crystallizing into highly aggregated particles.[86,87] Surfactant-assisted syntheses are generally hypothesized to control and slow down the precipitation rates.

1.4 Applications

1.4.1 ZrO_2 nanocrystals

ZrO_2 nanocrystals are great building blocks for material science. Shaw *et al.* used ZrO_2 nanocrystals to fabricate crack-free coatings.[54,88,89] After deposition, the organic ligands are removed by an oxygen plasma, and the particles simultaneously sinter together (providing mechanical strength to the coating). Note that the ligand's original mixture of TOPO, octylphosphinic acid and octylphosphonic acid anhydride, leads to residual phosphate in the final material. By ligand exchange with oleic acid prior to deposition, this could be minimized.[89] On the other hand, Talapin *et al.* obtained patterns

of ZrO_2 (and TiO_2 and HfO_2) by a method that was coined DOLFIN (Direct Optical Lithography of Functional Inorganic Nanomaterials).[90,91] The surface is first functionalized with photoactive ligands. Irradiation by UV light triggers the decomposition of the ligand, and as a result, the nanocrystals are no longer soluble. Patterns are obtained by a three-step process: layer deposition, illumination through a mask, and washing off unexposed nanocrystals. ZrO_2 nanocrystals are also used in nanocomposites. For example, composites of ZrO_2 NCs and epoxy polymer feature a high refractive index. Such nanocomposites are useful to encapsulate LEDs since the nanocomposite reduces the refractive index mismatch between the semiconductor LED material and air, thereby improving the light-extraction efficiency.[92] The high refractive index was further exploited in volume holography.[36] All-inorganic nanocomposites of ZrO_2 nanocrystals and $YBa_2Cu_3O_{7-\delta}$ superconductors have superior conductive properties over the pure superconductor.[46,93,94] $YBa_2Cu_3O_{7-\delta}$ is a type II superconductor and in high magnetic fields moving vortex currents destroy the superconducting state. The inclusion of nanocrystals pins the vortexes, enhancing the critical current at high magnetic fields. Finally, europium and terbium doped ZrO_2 NCs, stabilized by 2-aminoethyl phosphoric acid ligand, were developed for targeted bioimaging.[44] By coupling the amino group of the ligand with biotin *via* an amide bond, the nanocrystals obtained a high affinity for avidin. As a result, avidin could be detected *via* time-resolved Fluorescence Resonance Energy Transfer (FRET).

1.4.2 HfO_2 nanocrystals

HfO_2 NCs are being developed as components in next generation memory devices, based on memristors.[56,95] While memristors are traditionally fabricated with thin films of pure oxides, also assemblies of ligand capped nanocrystals can be switched from a high to a low resistance state. The voltage required to switch from one state to the other, depends on the ligand length and is minimized for shorter ligands.[95] Similar to bulk, ferroelectricity is also reported in HfO_2 nanorods.[20] HfO_2 nanocrystals are also among the few nanomaterials that made it to real clinical translation.[96] They are used in cancer treatment to locally enhance radiotherapy. The nanocrystals are directly injected into the tumor tissue and convert X-rays into reactive oxygen species that destroy the tumor.[97,98] The high X-ray absorption cross section of HfO_2 was also exploited in scintillators and medical imaging.[99,100] Nanocomposites of polymer, nanocrystals, and dyes were fabricated, where the HfO_2 absorbs the photons and transfers them to a cascade of dyes, which convert them to visible light. In medical CT (computed tomography), HfO_2 nanocrystals serve as contrast agents that absorb X-rays more efficiently than soft tissue.[100] HfO_2 NCs doped with lanthanides have also been explored as luminescent probes.[101]

However, europium doped HfO_2 NCs, that were capped with 2-[2-(2-methoxyethoxy)ethoxy]acetic acid, are not very stable in water and buffer solutions, causing aggregation during the staining of cells. Finally, HfO_2 nanocrystals have been used as catalysts for (*trans*)esterification reactions.[102] The fatty acid substrate was also used as a ligand, thereby eliminating the competition of ligands (necessary for colloidal stability) and substrates for the active surface sites.

1.5 Hard X-ray based characterization for nanocrystals

X-ray based techniques such as scattering, absorption spectroscopy, computed tomography, photoelectron spectroscopy, microscopy, and fluorescence spectroscopy are important methods for material characterization. Depending on the energy of the photons used they are categorized as soft or hard X-ray techniques. Hard X-ray techniques refer to methods that utilize photon energies greater than 5-10 keV. The selection of appropriate techniques depends on the material's response and the information required. X-ray scattering is one of the most popular methods for structural and compositional analysis of materials. X-rays are electromagnetic waves that cause elastic scattering when they interact with an atom, generating secondary spherical waves by scattering electrons. An ordered arrangement of the scatterers (electrons) results in a regular array of spherical waves that add or cancel by constructive or destructive interference, respectively. Accordingly, the resulting diffraction pattern can be used to illuminate the structural details of the material. In this section, we will concentrate on two distinct types of X-ray scattering methods, namely total scattering and small-angle scattering.

1.5.1 X-ray total scattering and pair distribution function analysis

X-ray powder diffraction is a very practical and powerful method for structural characterization of crystalline materials. However, one of the major drawbacks of this technique is that it can only be applied when some order of atomic arrangement (crystallinity) is present in the material. This limits the characterization of amorphous or disordered materials. At the nanoscale, analysis is difficult due to the small crystallite size, even when atomic order is present in the material. As the crystallite size decreases, the full width at half maxima (FWHM) of the Bragg peak increases, leading to a broadening of the diffraction peak as described by the Scherrer equation.

$$\tau = \frac{K\lambda}{\beta cos\theta} \tag{1.10}$$

(τ = mean size of crystalline domains, K = shape factor, λ = wavelength, β = line broadening at FWHM, θ = Bragg angle)

The broadening hides important structural features and limits the amount of information that can be extracted from the diffraction pattern. The above-mentioned challenge is referred to as the "nanostructure problem: the need to determine the atomic arrangement in nanostructured materials".[103] Total scattering methods have been introduced as a solution. When X-rays are scattered from atoms in a material, two types of elastic scattering can occur: Bragg scattering and diffuse scattering. Bragg scattering arises from the ordered arrangement of atoms in the material, resulting in sharp diffraction peaks in the scattering pattern. In contrast, diffuse scattering arises from the disorder in the atomic arrangement, resulting in a diffuse scattering pattern. The diffraction pattern that results from Bragg scattering is intense and relatively easy to analyze. However, the diffraction pattern resulting from diffuse scattering is less intense and is below the Bragg peaks, making analysis complicated.[104] In conventional powder diffraction methods, diffuse scattering is completely avoided in the analysis so that only limited information about the disorder can be extracted. If we consider both Bragg and diffuse scattering data for analysis (total scattering method), we can exceed the limits of structural analysis and obtain more comprehensive information about the atomic arrangement in the material.[104,105]

The experiment

X-ray diffraction experiments are based on either reflection (Bragg-Brentano geometry) or transmission (Debye-Scherrer geometry). Reflection geometry is the most common geometry with a moving sample stage, detector, or both, and is used in most laboratory instruments. Intensity is recorded as a function of 2θ, where 2θ is the scattering angle. On the other hand, transmission geometry uses a large 2D area detector, which is common in setups that use high-energy photon sources like synchrotrons. The resulting 2D diffraction pattern is then converted to a 2θ versus intensity plot through azimuthal integration. Alternatively, the intensity can be expressed as a function of the scattering vector (Q). Since the intensity as a function of Q is wavelength independent, it is useful for comparing data obtained from different X-ray sources.

$$Q = \frac{4\pi\, sin\theta}{\lambda} \quad (\lambda = wavelength) \tag{1.11}$$

For a standard X-ray diffraction measurement, the maximum value of Q (Qmax) is about 5 $Å^{-1}$. In total scattering measurements, a high Qmax value is important for obtaining a high Q resolution, which in turn improves the discrimination between peaks and allows for more accurate structural analysis. Conversely, a low Qmax can result in a broadening of peaks and limited information retrieval. According to the equation 1.11, there are two ways to increase Qmax. The first approach is to use high-energy X-rays, which correspond to shorter wavelengths. It is recommended to use X-rays with a wavelength of around 0.1 Å. The second approach is to maximize the scattering angle 2θ by placing the sample close to the detector. Placing the detector too close may increase the number of data points beyond the detector's resolution. Therefore, it is essential to optimize the distance between the sample and detector while considering the required Qmax and data quality.

Data reduction and analysis

The X-ray diffractogram (intensity data) is typically normalized and corrected to obtain the structure function, which is then Fourier transformed into the real space pair distribution function.[104, 106, 107] The data reduction procedure for obtaining the PDF involves several steps, as shown in Fig. 1.6. PDF is represented by G(r) and is a measure of the probability of finding atoms separated by distance r. The position of the peaks in G(r) represents the distance between the atoms. The intensity of the peak depends on the number of pairs present and the scattering power of the atom (atomic form factor). For example, hafnium scatters much more strongly than oxygen. A comparison of I(Q), G(r) of bulk Ni and 4 nm ZrO_2 is shown in Fig. 1.7.

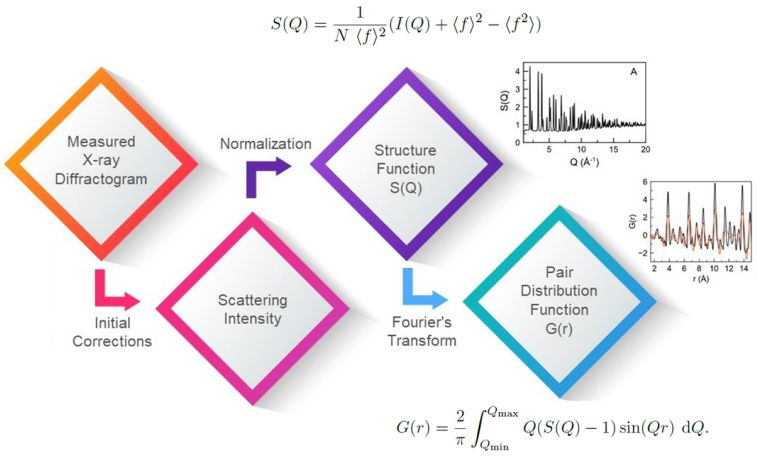

Fig. 1.6 | **Data reduction.** Reduction of measured X-ray diffractogram to pair distribution function.

Due to the long-range ordering and large crystallite size, sharp peaks are present in the I(Q) of bulk nickel. In contrast, the peaks are broad in ZrO_2 nanocrystals. In G(r), the pairs of atoms corresponding to the peaks are shown. In ZrO_2, two types of atoms are present, so three types of atom pairs are expected (Zr-Zr, Zr-O, and O-O). Since Zr is the largest atom among them, the pairs involving Zr atoms will be more intense. From Fig. 1.7b, it can be seen that Zr-Zr interactions are more intense than Zr-O. Due to the relatively low intensity, the O-O interactions are indistinguishable from the noise. This also means that the interactions corresponding to the organic ligands on the surface of the nanocrystal are not visible. In the case of Ni, there is only one type of atom, so all interactions correspond to Ni-Ni pairs. The difference in the intensity of the different Ni-Ni peaks corresponds to the number of pairs.

For polyatomic systems, the analysis is limited by the differences in the atomic form factor of the individual atoms. If the system consists of very strongly and very weakly scattering elements, the interaction of the latter will be suppressed by the former. Despite the weaker scattering from lighter atoms such as carbon or hydrogen compared to heavier atoms, it is still measurable and can provide useful information about the atomic arrangement in a sample. As a result, PDF analysis has been successfully used to study a broad range of materials including organic molecules.[108] Another advantage of PDF analysis is the ability to study local structure.[109] At times, the local atomic arrangement of a material may differ from its average or global structure. This can be challenging to detect using other analytical techniques, especially at the nanoscale. These differences may be due to defects and disorders. However, the study of defects is important as they can confer unique properties to materials, making them more interesting than defect-free materials. In some cases, defects may be intentionally incorporated to achieve desired properties. Thus the local structure analysis can provide fundamental insights into structure-function correlation studies and support the development of advanced materials with novel applications.

PDF analysis is not restricted to the characterization of the final product or pure material. It can also be used to monitor reactions *in situ* and study atomic-level changes during formation, enabling the investigation of nucleation and growth mechanisms.[110,111]

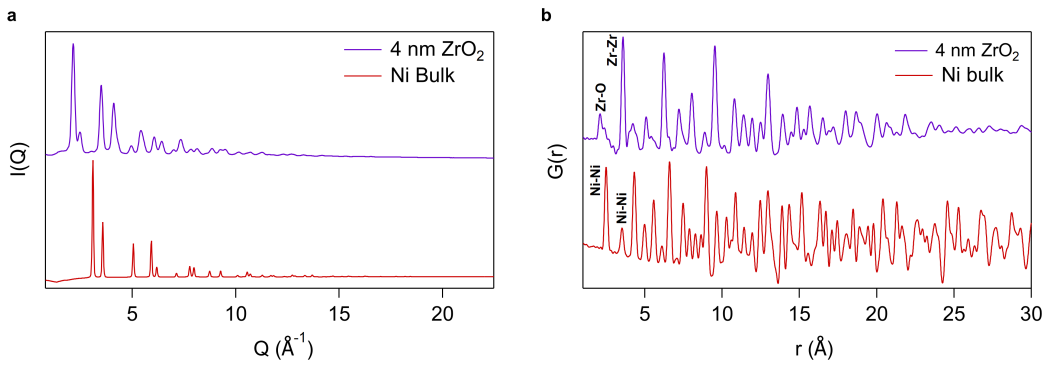

Fig. 1.7 | **Comparison of PDFs.** I(Q) and G(r) for **a** bulk Ni and **b** 4 nm ZrO_2 nanocrystals. The intensity is normalized for better visualization.

Fitting the experimental data

The obtained experimental PDF (G(r)) can be further validated by fitting it with a theoretical model. There are several tools available for modeling, which can be broadly divided into small-box models and large-box models. Small-box or attenuated-crystal modeling uses a small structural model that can represent the entire system. The model is then extended by constraining the structural features to fit the experimentally obtained information. One example of this is fitting the experimental PDF of a nanocrystal using a crystallographic information file (CIF). If a previously reported CIF is available, this method is very straightforward. PDFgui and diffpy-CMI (Complex modeling infrastructure) are the popular platforms for small-box modeling.[112,113] RMCProfile is one of the platforms for large-box modeling, where an atomic structure is derived directly from the experimental data.[114] The atomic arrangements are modified until they best match the properties in the experimental data.

1.5.2 X-ray small angle scattering analysis

Small-angle X-ray scattering (SAXS) is another scattering technique widely used by materials scientists. According to Bragg's law, larger structural features can be obtained at small scattering angles. SAXS experiments provide information on features ranging from 1 - 100 nm. Ultra-small angle X-ray scattering (USAXS) can be used to study even larger distances. However, since features are studied at the nanoscale, this technique cannot provide information on the atomic structure. Nevertheless, important information on size, size distribution, shape, surface area to volume ratio, concentration, and more can be obtained. SAXS is particularly interesting because crystalline samples are not required, unlike other techniques that rely on atomic order. Therefore, SAXS can be applied to a wide range of materials.

The experimental setup is similar to total scattering. However, SAXS experiments are performed at a much smaller scattering angle, typically between 0.1° and 5°, by moving the detector far away from the sample. A 2D area detector is used to collect the elastic scattering signals. After necessary corrections, the obtained images are azimuthally integrated into a one-dimensional scattering curve (as a function of the scattering vector or scattering angle). The particle size and concentration were quantified by fitting the normalized scattering curves with a theoretical model. The theoretical scattering cross-section of the distribution of spheres of homogeneous electron density dispersed in a solvent is given by:

$$I = n(\Delta\rho)^2 \int_0^\infty V(R)^2 D(R) P(q,R) dR$$

where n is the particle concentration, $\Delta\rho$ is the difference in scattering length density between the particles and the solvent (the contrast), V(R) is the volume of a sphere of radius R, D(R) is the radius distribution, and P(q,R) is the form factor of a sphere.

In Fig. 1.8 the SAXS curve for 4 nm ZrO_2 nanocrystals dissolved in toluene and the corresponding fit with the theoretical scattering with a spherical distribution are shown. The fit is a perfect match and particle distribution follows the Schulz distribution. According to the fit, the diameter and polydispersity are 4 nm and 11% respectively. The obtained results are in agreement with TEM and PDF analysis.

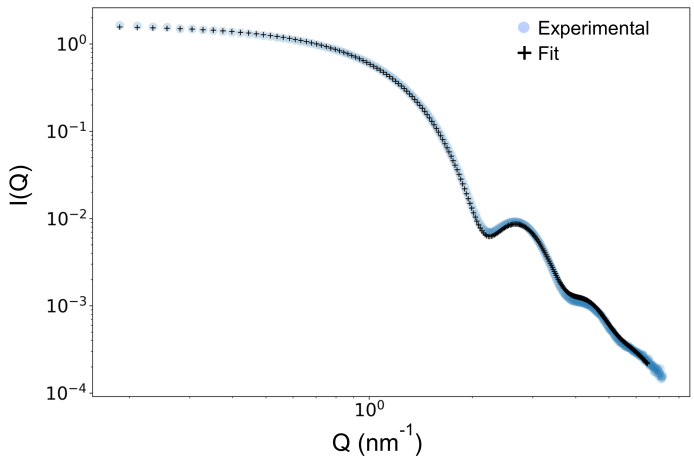

Fig. 1.8 | SAXS analysis for 4 nm ZrO_2 nanocrystals. SAXS curve and the corresponding fit with the theoretical scattering with a distribution of sphere sizes.

Numerous software platforms are available for SAXS analysis. Depending on the particle morphology and the specific research question, different software packages may be better suited for analyzing the data. Those interested in a more comprehensive discussion of SAXS software packages may find useful information on SAS Portal.[115]

In nanoparticle research, knowing the size, concentration, and polydispersity can provide valuable information about the nucleation and growth mechanism. The complementary nature of SAXS and PDF would be ideal for the investigation since the former accounts for all particles (crystalline and amorphous) and the crystalline fraction can be specifically filtered out using the PDF analysis.*

1.6 Problem statement

ZrO_2 nanocrystals possess intriguing material properties. Nevertheless, they drew less attention from the research community because of the absence of an optical signature, making the investigation difficult. These nanocrystals can be synthesized using either surfactant-free or surfactant-assisted synthetic procedures. Structural variations in cubic, tetragonal, or monoclinic nanocrystals can be achieved in benzyl alcohol synthesis by modifying the zirconium precursor. The underlying mechanism responsible for such variations is yet to be determined. On the other hand, in the TOPO synthesis, tetragonal nanocrystals with superior polydispersity and colloidal stability can be obtained. The size of the nanocrystals can be adjusted by changing the halide precursor. In contrast, for HfO_2, the reaction temperature needs to be slightly higher. The size and shape of the nanocrystals can be controlled by adjusting the temperature or precursor used in the synthesis, and the size can also be modulated by periodically injecting the precursor. Additionally, HfO_2 nanocrystals have unique properties that result from the defects in their crystal structure such as oxygen vacancies.

One can readily generate the nanocrystals by modifying the size, structure, shape, and properties of these nanocrystals, but the underlying chemistry is not well understood. Which is primarily due to the lack of detailed mechanistic studies. Understanding the mechanisms of synthesis can provide insight into the observed effects and can aid in the development of novel materials with potential applications. To advance the field of metal oxide nanocrystals, it is crucial to deepen our understanding of precursor chemistry, nucleation, and growth mechanisms. By investigating precursor chemistry, we can gain insights into the reactivity of different precursors and the role of surfactants in

*The SAXS technique is not my expertise and is performed by collaborators.

the synthesis. Nucleation and growth mechanisms can provide insights into size and shape tunability.

After a thorough understanding of the synthesis, a significant correlation between the structure, function, and synthesis of the material can be formulated. According to the materials science tetrahedron (depicted in Fig. 1.9), the synthesis, structure, properties, and performance of the material are interrelated.[116] Effective tuning of a material's properties and performance can be achieved by understanding the correlation. Since the size-dependent structural transformations are observed in ZrO_2 and HfO_2, structural modifications can be made using the gained insight. With the help of precise structural characterization techniques such as Pair Distribution Function analysis, it is possible to identify the details of structural changes and defects within the material. With sensitive structure-function correlations at the center of nanoscience, materials tailored for specific applications can be developed.

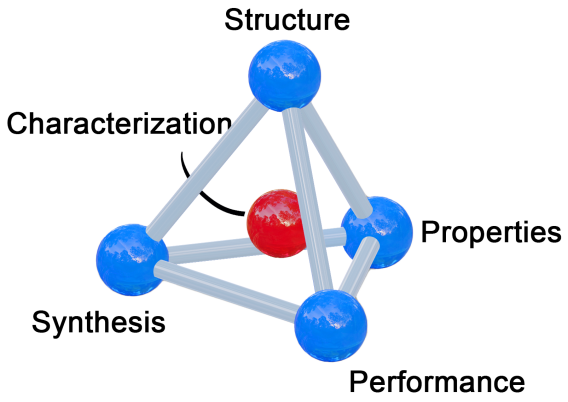

Fig. 1.9 | Material science tetrahedron. Tetrahedron shows the correlation between synthesis, structure, properties, and performance.

1.7 Outline

The research is divided into three key chapters, each focusing on an important aspect. In the first chapter, we explore the precursor chemistry involved in the surfactant-assisted non-aqueous synthesis of ZrO_2 nanocrystals using $ZrCl_4$ and zirconium isopropoxide isopropanol complex in TOPO. Investigation begins by studying the individual interactions of each precursor with TOPO. Subsequently, we examine the precursor mixtures under room temperature and actual reaction conditions. To unravel this part, we employ various techniques such as NMR analysis, PDF analysis, GC-FID, and quantum chemical calculations. In addition, we present a seeded growth approach to increase the size of the nanocrystals. In the next chapter, we dive into the nucleation and growth mechanism. Here, we

combine PDF and SAXS analysis to investigate the species formed during the reaction. We also discuss the strategies employed for achieving size tunability. This chapter provides a comprehensive understanding of the processes underlying the formation and growth of ZrO_2 nanocrystals. In the next chapter, we focus on identifying the local structural distortion in nanoscale ZrO_2 and its potential connection to the origin of ferroelectricity. We explore various possibilities for characterizing and understanding the ferroelectric behavior observed in the material. Finally, the thesis concludes by summarizing the findings and presenting future prospects for further exploration and advancement in this field.

Bibliography

[1] R. D. Shannon. Revised effective ionic radii and systematic studies of interatomic distances in halides and chalcogenides. *Acta Crystallographica*, 32(A31):751–767, 1976.

[2] J. Tang, J. Fabbri, R. D. Robinson, Y. Zhu, I. P. Herman, M. L. Steigerwald, and L. E. Brus. Solid-solution nanoparticles: Use of a nonhydrolytic sol-gel synthesis to prepare HfO_2 and $Hf_xZr_{1-x}O_2$ nanocrystals. *Chemistry of Materials*, 16(7):1336–1342, 2004.

[3] J. C. Slater. Atomic radii in crystals. *Chemical Physics*, 41(10):3199–3204, 1964.

[4] J. E. Huheey, E. A. Keiter, and R. L. Keiter. *Inorganic Chemistry : Principles of Structure and Reactivity*. HarperCollins, New York, 4^{th} edition, 1993.

[5] C. Tantardini and A. R. Oganov. Thermochemical electronegativities of the elements. *Nature Communications*, 12(1):2087, 2021.

[6] U. Diebold. The surface science of titanium dioxide. *Surface Science Reports*, 48(5):53–229, 2003.

[7] R. N. Patil and E. C. Subbarao. Axial thermal expansion of ZrO_2 and HfO_2 in the range room temperature to 1400 °C. *Journal of Applied Crystallography*, 2(6):281–288, Dec 1969.

[8] J. Robertson. High dielectric constant oxides. *The European Physical Journal Applied Physics*, 28(3):265–291, 2004.

[9] L. Kavan, M. Grätzel, S. E. Gilbert, C. Klemenz, and H. J. Scheel. Electrochemical and photoelectrochemical investigation of single-crystal anatase. *Journal of the American Chemical Society*,

118(28):6716–6723, 1996.

[10] S. H. Elder, F. J. DiSalvo, L. Topor, and A. Navrotsky. Thermodynamics of ternary nitride formation by ammonolysis: Application to lithium molybdenum nitride ($LiMo_2$), sodium tungsten nitride (Na_3WN_3), and sodium tungsten oxide nitride (Na_3WO_3N). *Chemistry of Materials*, 5(10):1545–1553, 1993.

[11] R. Marchand, L. Brohan, and Tournoux M. A new form of titanium dioxide and the potassium octatitanate $K_2Ti_8O_{17}$. *Materials Research Bulletin*, 15(15(8)):1129–1133, 1980.

[12] M. Latroche, L. Brohan, R. Marchand, and M. Tournoux. New hollandite oxides: TiO_2(H) and $K_{0.06}TiO_2$. *Journal of Solid State Chemistry*, 81(81(1)):78–82, 1989.

[13] J. Akimoto, Y. Gotoh, Y. Oosawa, N. Nonose, T. Kumagai, K. Aoki, and H. Takei. Topotactic oxidation of ramsdellite-type $Li_{0.5}TiO_2$, a new polymorph of titanium dioxide: TiO_2(R). *Journal of Solid State Chemistry*, 113(113(1)):27–36, 1994.

[14] P. Y. Simons and F. Dachille. The structure of II, a high-pressure phase of TiO_2. *Acta Crystallographica*, 23(23(2)):334–336, 1967.

[15] H. Sato, S. Endo, M. Sugiyama, T. Kikegawa, O. Shimomura, and K. Kusaba. Baddeleyite-type high-pressure phase of tio_2. *Science*, (251(4995)):786–788, 1991.

[16] N. A. Dubrovinskaia, L. S. Dubrovinsky, R. Ahuja, V. B. Prokopenko, V. Dmitriev, H. P. Weber, J. M. Osorio-Guillen, and B. Johansson. Experimental and theoretical identification of a new high-pressure TiO_2 polymorph. *Physical Review Letters*, (87):275501, 2001.

[17] M. Mattesini, J. S. de Almeida, L. Dubrovinsky, L. Dubrovinskaia, B. Johansson, and R. Ahuja. High-pressure and high-temperature synthesis of the cubic TiO_2 polymorph. *Physical Review B*, 70(70(21)):212101, 2004.

[18] L. S. Dubrovinsky, N. A. Dubrovinskaia, V. M. J. Swamy, N. M. Harrison, R. Ahuja, B. Holm, and B. Johansson. The hardest known oxide. *Nature*, (4(6)):1104–1116, 2001.

[19] M. N. Tsampas, F. M. Sapountzi, and P. Vernoux. Applications of yttria stabilized zirconia (YSZ) in catalysis. *Catalysis Science and Technology*, 5:4884–4900, 2015.

[20] S. W. Depner, N. D. Cultrara, K. E. Farley, Y. Qin, and S. Banerjee. Ferroelastic domain or-

ganization and precursor control of size in solution-grown hafnium dioxide nanorods. *ACS Nano*, 8(5):4678–4688, 2014.

[21] S. W. Depner, K. R. Kort, and S. Banerjee. Precursor control of crystal structure and stoichiometry in twin metal oxide nanocrystals. *CrystEngComm*, 11(5):841–846, 2009.

[22] J. Joo, T. Yu, Y. W. Kim, H. M. Park, F. Wu, J. Z. Zhang, and T. Hyeon. Multigram scale synthesis and characterization of monodisperse tetragonal zirconia nanocrystals. *Journal of the American Chemical Society*, 125(21):6553–6557, 2003.

[23] O. Jr. Hunter, R. W. Scheidecker, and S. Tojo. Characterization of metastable tetragonal hafnia. *Ceramics*, 5(4):137–142, 1 1979.

[24] S. V. Ushakov, A. Navrotsky, Y. Yang, S. Stemmer, K. Kukli, M. Ritala, M. A. Leskelä, P. Fejes, A. Demkov, and C. Wang. Crystallization in hafnia- and zirconia-based systems. *Physica Status Solidi B*, 241(10):2268–2278, 2004.

[25] W. Zhou, S. V. Ushakov, T. Wang, J. G. Ekerdt, A. A. Demkov, and A. Navrotsky. Hafnia: Energetics of thin films and nanoparticles. *Journal of Applied Physics*, 107(12):123514, 2010.

[26] G. R. Waetzig, S. W. Depner, H. Asayesh-Ardakani, N. D. Cultrara, R. Shahbazian-Yassar, and S. Banerjee. Stabilizing metastable tetragonal HfO_2 using a non-hydrolytic solution-phase route: Ligand exchange as a means of controlling particle size. *Chemical Science*, 7:4930–4939, 2016.

[27] X. Zhao and D. Vanderbilt. First-principles study of structural, vibrational, and lattice dielectric properties of hafnium oxide. *Physical Review B*, 65:233106, 2002.

[28] T. D. Huan, V. Sharma, G. A. Rossetti, and R. Ramprasad. Pathways towards ferroelectricity in hafnia. *Physical Review B*, 90:064111, 2014.

[29] X. Xu, F. Huang, Y. Qi, S. Singh, K. M. Rabe, D. Obeysekera, J. Yang, M. Chu, and S. Cheong. Kinetically stabilized ferroelectricity in bulk single-crystalline HfO_2:Y. *Nature Materials*, 2021.

[30] S. S. Cheema, D. Kwon, N. Shanker, R. dos Reis, S. Hsu, J. Xiao, H. Zhang, R. Wagner, A. Datar, M. R. McCarter, C. R. Serrao, A. K. Yadav, G. Karbasian, C. Hsu, A. J. Tan, L. Wang, V. Thakare, X. Zhang, A. Mehta, E. Karapetrova, R. V. Chopdekar, P. Shafer, E. Arenholz, C. Hu, R. Proksch, R. Ramesh, J. Ciston, and S. Salahuddin. Enhanced ferroelectricity in ultrathin films grown directly

on silicon. *Nature*, 580(7804):478–482, 2020.

[31] U. Schroeder, C. Richter, M. H. Park, T. Schenk, M. Pešić, M. Hoffmann, F. P. G. Fengler, D. Pohl, B. Rellinghaus, and C. Zhou. Lanthanum-doped hafnium oxide: A robust ferroelectric material. *Inorganic Chemistry*, 57(5):2752–2765, 2018.

[32] J. Müller, T. S. Böscke, U. Schröder, S. Mueller, D. Bräuhaus, U. Böttger, L. Frey, and T. Mikolajick. Ferroelectricity in simple binary ZrO_2 and HfO_2. *Nano Letters*, 12(8):4318–4323, 2012.

[33] M. Niederberger and H. Cölfen. Oriented attachment and mesocrystals: Non-classical crystallization mechanisms based on nanoparticle assembly. *Physical Chemistry Chemical Physics*, 8:3271–3287, 2006.

[34] R. Deshmukh and M. Niederberger. Mechanistic aspects in the formation, growth and surface functionalization of metal oxide nanoparticles in organic solvents. *Chemistry: A European Journal*, 23(36):8542–8570, 2017.

[35] M. Niederberger. Nonaqueous sol–gel routes to metal oxide nanoparticles. *Accounts of Chemical Research*, 40(9):793–800, 2007.

[36] G. Garnweitner, L. M. Goldenberg, O. V. Sakhno, M. Antonietti, M. Niederberger, and J. Stumpe. Large-scale synthesis of organophilic zirconia nanoparticles and their application in organic-inorganic nanocomposites for efficient volume holography. *Small*, 3(9):1626–1632, 2007.

[37] J. De Roo, F. Van den Broeck, K. De Keukeleere, J. C. Martins, I. Van Driessche, and Z. Hens. Unravelling the surface chemistry of metal oxide nanocrystals, the role of acids and bases. *Journal of the American Chemical Society*, 136(27):9650–9657, 2014.

[38] K. De Keukeleere, J. De Roo, P. Lommens, J. C. Martins, P. Van der Voort, and I. Van Driessche. Fast and tunable synthesis of ZrO_2 nanocrystals: Mechanistic insights into precursor dependence. *Inorganic Chemistry*, 54(7):3469–3476, 2015.

[39] S. X. Zhou, G. Garnweitner, M. Niederberger, and M. Antonietti. Dispersion behavior of zirconia nanocrystals and their surface functionalization with vinyl group-containing ligands. *Langmuir*, 23(18):9178–9187, 2007.

[40] C. Grote, T. A. Cheema, and G. Garnweitner. Comparative study of ligand binding during the

postsynthetic stabilization of metal oxide nanoparticles. *Langmuir*, 28(40):14395–14404, 2012.

[41] F. Rechberger, F. J. Heiligtag, M. J. Süess, and M. Niederberger. Assembly of $BaTiO_3$ nanocrystals into macroscopic aerogel monoliths with high surface area. *Angewandte Chemie International Edition*, 53(26):6823–6826, 2014.

[42] T. A. Cheema and G. Garnweitner. Phase-controlled synthesis of ZrO_2 nanoparticles for highly transparent dielectric thin films. *CrystEngComm*, 16(16):3366–3375, 2014.

[43] J. De Roo, N. Yazdani, E. Drijvers, A. Lauria, J. Maes, J. S. Owen, I. Van Driessche, M. Niederberger, V. Wood, J. C. Martins, I. Infante, and Z. Hens. Probing solvent–ligand interactions in colloidal nanocrystals by the NMR line broadening. *Chemistry of Materials*, 30(15):5485–5492, 2018.

[44] Y. Liu, S. Zhou, D. Tu, Z. Chen, M. Huang, H. Zhu, E. Ma, and X. Chen. Amine-functionalized lanthanide-doped zirconia nanoparticles: Optical spectroscopy, time-resolved fluorescence resonance energy transfer biodetection, and targeted imaging. *Journal of the American Chemical Society*, 134(36):15083–15090, 2012.

[45] C. Suchomski, D. J. Weber, P. Dolcet, A. Hofmann, P. Voepel, J. Yue, M. Einert, M. Möller, S. Werner, S. Gross, I. Djerdj, T. Brezesinski, and B. M. Smarsly. Sustainable and surfactant-free high-throughput synthesis of highly dispersible zirconia nanocrystals. *Journal of Materials Chemistry A*, 5(31):16296–16306, 2017.

[46] H. Rijckaert, J. De Roo, M. Van Zele, S. Banerjee, H. Huhtinen, P. Paturi, J. Bennewitz, S. J. L. Billinge, M. Bäcker, K. De Buysser, and I. Van Driessche. Pair distribution function analysis of ZrO_2 nanocrystals and insights in the formation of ZrO_2-$YBa_2Cu_3O_7$ nanocomposites. *Materials*, 11(7):1066, 2018.

[47] J. Gambe, F. Rémondière, J. Jouin, L. Portal, P. Thomas, and O. Masson. Detrimental effect and neutralization of in situ produced water on zirconia nanoparticles obtained by a nonaqueous sol–gel method. *Inorganic Chemistry*, 22:15175–15188, 2019.

[48] N. Pinna, G. Garnweitner, M. Antonietti, and M. Niederberger. Non-aqueous synthesis of high-purity metal oxide nanopowders using an ether elimination process. *Advanced Materials*, 16(23-24):2196–2200, 2004.

[49] P. Rauwel, A. Galeckas, and E. Rauwel. One step synthesis of pure cubic and monoclinic HfO_2 nanoparticles: Effects of temperature and ambient on the photoluminescent properties. *ECS Transactions*, 64(44):19–28, 2015.

[50] J. De Roo, K. De Keukeleere, J. Feys, P. Lommens, Z. Hens, and I. Van Driessche. Fast, microwave-assisted synthesis of monodisperse HfO_2 nanoparticles. *Journal of Nanoparticle Research*, 15(7):11, 2013.

[51] J. Buha, D. Arčon, M. Niederberger, and I. Djerdj. Solvothermal and surfactant-free synthesis of crystalline Nb_2O_5, Ta_2O_5, HfO_2, and Co-doped HfO_2 nanoparticles. *Physical Chemistry Chemical Physics*, 12(47):15537–15543, 2010.

[52] J. De Roo, K. De Keukeleere, Z. Hens, and I. Van Driessche. From ligands to binding motifs and beyond; the enhanced versatility of nanocrystal surfaces. *Dalton Transactions*, 45(34):13277–83, 2016.

[53] K. De Keukeleere, S. Coucke, E. De Canck, P. Van Der Voort, F. Delpech, Y. Coppel, Z. Hens, I. Van Driessche, J. S. Owen, and J. De Roo. Stabilization of colloidal Ti, Zr, and Hf oxide nanocrystals by protonated tri-n-octylphosphine oxide (TOPO) and its decomposition products. *Chemistry of Materials*, 29(23):10233–10242, 2017.

[54] S. Shaw, B. Yuan, X. Tian, K. J. Miller, B. M. Cote, J. L. Colaux, A. Migliori, M. G. Panthani, and L. Cademartiri. Building materials from colloidal nanocrystal arrays: Preventing crack formation during ligand removal by controlling structure and solvation. *Advanced Materials*, 28(40):8892–8899, 2016.

[55] E. Tirosh and G. Markovich. Control of defects and magnetic properties in colloidal HfO_2 nanorods. *Advanced Materials*, 19(18):2608–2612, 2007.

[56] J. De Roo, Z. Zhou, J. Wang, L. Deblock, A. J. Crosby, J. S. Owen, and S. S. Nonnenmann. Synthesis of phosphonic acid ligands for nanocrystal surface functionalization and solution processed memristors. *Chemistry of Materials*, 30(21):8034–8039, 2018.

[57] E. Dhaene, J. Billet, E. Bennett, I. Van Driessche, and J. De Roo. The trouble with ODE: Polymerization during nanocrystal synthesis. *Nano Letters*, 19(10):7411–7417, 2019.

[58] E. Matijevic. Preparation and properties of uniform size colloids. *Chemistry of Materials*, 5(4):412–

426, 1993.

[59] V. K. LaMer and R. H. Dinegar. Theory, production and mechanism of formation of monodispersed hydrosols. *Journal of the American Chemical Society*, 72(11):4847–4854, 1950.

[60] C. B. Whitehead, S. Özkar, and R. G. Finke. Lamer's 1950 model for particle formation of instantaneous nucleation and diffusion-controlled growth: A historical look at the model's origins, assumptions, equations, and underlying sulfur sol formation kinetics data. *Chemistry of Materials*, 31(18):7116–7132, 2019.

[61] S. Mozaffari, W. Li, C. Thompson, S. Ivanov, S. Seifert, B. Lee, L. Kovarik, and A. M. Karim. Colloidal nanoparticle size control: experimental and kinetic modeling investigation of the ligand–metal binding role in controlling the nucleation and growth kinetics. *Nanoscale*, 9(36):13772–13785, 2017.

[62] P. T. Prins, F. Montanarella, K. Dümbgen, Y. Justo, J. C. van der Bok, S. O. M. Hinterding, J. J. Geuchies, J. Maes, K. De Nolf, S. Deelen, H. Meijer, T. Zinn, A. V. Petukhov, F. T. Rabouw, C. De Mello Donega, D. Vanmaekelbergh, and Z. Hens. Extended nucleation and superfocusing in colloidal semiconductor nanocrystal synthesis. *Nano Letters*, 21(6):2487, 2021.

[63] B. M. McMurtry, K. Qian, J. K. Teglasi, A. K. Swarnakar, J. De Roo, and J. S. Owen. Continuous nucleation and size dependent growth kinetics of indium phosphide nanocrystals. *Chemistry of Materials*, 32(10):4358–4368, 2020.

[64] M. P. Campos, J. De Roo, M. W. Greenberg, B. M. McMurtry, M. P. Hendricks, E. Bennett, N. Saenz, M. Y. Sfeir, B. Abécassis, S. K. Ghose, and J. S. Owen. Growth kinetics determine the polydispersity and size of PbS and PbSe nanocrystals. *Chemical Science*, 13(16):4555–4565, 2022.

[65] B. Abécassis, M. W. Greenberg, V. Bal, B. M. McMurtry, M. P. Campos, L. Guillemeney, B. Mahler, S. Prevost, L. Sharpnack, M. P. Hendricks, D. DeRosha, E. Bennett, N. Saenz, B. Peters, and J. S. Owen. Persistent nucleation and size dependent attachment kinetics produce monodisperse PbS nanocrystals. *Chemical Science*, 13:4977–4983, 2022.

[66] B. Abécassis, C. Bouet, C. Garnero, D. Constantin, N. Lequeux, S. Ithurria, B. Dubertret, B. R. Pauw, and D. Pontoni. Real-time in situ probing of high-temperature quantum dots solution

synthesis. *Nano Letters*, 15(4):2620–2626, 2015.

[67] M. A. Watzky and R. G. Finke. Transition metal nanocluster formation kinetic and mechanistic studies. a new mechanism when hydrogen is the reductant: Slow, continuous nucleation and fast autocatalytic surface growth. *Journal of the American Chemical Society*, 119(43):10382–10400, 1997.

[68] S. Jeon, T. Heo, S. Hwang, J. Ciston, K. C. Bustillo, B. W. Reed, J. Ham, S. Kang, S. Kim, J. Lim, K. Lim, J. S. Kim, M. Kang, R. S. Bloom, S. Hong, K. Kim, A. Zettl, W. Y. Kim, P. Ercius, J. Park, and W. C. Lee. Reversible disorder-order transitions in atomic crystal nucleation. *Science*, 371(6528):498–503, 2021.

[69] W. J. E. M. Habraken, J. Tao, L. J. Brylka, H. Friedrich, L. Bertinetti, A. S. Schenk, A. Verch, V. Dmitrovic, P. H. H. Bomans, P. M. Frederik, J. Laven, P. van der Schoot, B. Aichmayer, G. de With, J. J. DeYoreo, and N. A. J. M. Sommerdijk. Ion-association complexes unite classical and non-classical theories for the biomimetic nucleation of calcium phosphate. *Nature Communications*, 4(1):1507, 2013.

[70] J. Baumgartner, A. Dey, P. H. H. Bomans, Cécile Le C., P. Fratzl, N. A. J. M. Sommerdijk, and D. Faivre. Nucleation and growth of magnetite from solution. *Nature Materials*, 12(4):310–314, 2013.

[71] J. Yang, J. Koo, S. Kim, S. Jeon, B. K. Choi, S. Kwon, J. Kim, B. H. Kim, W. C. Lee, W. B. Lee, H. Lee, T. Hyeon, P. Ercius, and J. Park. Amorphous-phase-mediated crystallization of ni nanocrystals revealed by high-resolution liquid-phase electron microscopy. *Journal of the American Chemical Society*, 141(2):763–768, 2019.

[72] C. Gary, Dylan, W. Terban, Maxwell, J. L. Billinge, Simon, and M. Cossairt, Brandi. Two-step nucleation and growth of InP quantum dots via magic-sized cluster intermediates. *Chemistry of Materials*, 27(4):1432–1441, 2015.

[73] H. Chang, B. H. Kim, H. Y. Jeong, J. H. Moon, M. Park, K. Shin, S. I. Chae, J. Lee, T. Kang, B. K. Choi, J. Yang, M. S. Bootharaju, H. Song, S. H. An, K. M. Park, J. Y. Oh, H. Lee, M. S. Kim, J. Park, and T. Hyeon. Molecular-level understanding of continuous growth from iron-oxo clusters to iron oxide nanoparticles. *Journal of the American Chemical Society*, 141(17):7037–7045, 2019.

[74] D. V. Talapin, A. L. Rogach, M. Haase, and H. Weller. Evolution of an ensemble of nanoparticles in a colloidal solution: theoretical study. *The Journal of Physical Chemistry B*, 105(49):12278–12285, 2001.

[75] D. R. Handwerk, P. D. Shipman, C. B. Whitehead, S. Özkar, and R. G. Finke. Particle size distributions via mechanism-enabled population balance modeling. *The Journal of Physical Chemistry C*, 124(8):4852–4880, 2020.

[76] D. V. Leff, P. C. Ohara, J. R. Heath, and W. M. Gelbart. Thermodynamic control of gold nanocrystal size: Experiment and theory. *The Journal of Physical Chemistry*, 99(18):7036–7041, 1995.

[77] Y. Chen, E. Johnson, and X. Peng. Formation of monodisperse and shape-controlled MnO nanocrystals in non-injection synthesis: Self-focusing via ripening. *Journal of the American Chemical Society*, 129(35):10937–10947, 2007.

[78] Y. A. Yang, H. Wu, K. R. Williams, and Y. C. Cao. Synthesis of CdSe and CdTe nanocrystals without precursor injection. *Angewandte Chemie International Edition*, 44(41):6712–6715, 2005.

[79] Y. Wang, Y. Zhang, F. Wang, D. E. Giblin, J. Hoy, H. W. Rohrs, R. A. Loomis, and W. E. Buhro. The magic-size nanocluster $(CdSe)_{34}$ as a low-temperature nucleant for cadmium selenide nanocrystals; room-temperature growth of crystalline quantum platelets. *Chemistry of Materials*, 26(7):2233–2243, 2014.

[80] C. Pacholski, A. Kornowski, and H. Weller. Self-assembly of ZnO: From nanodots to nanorods. *Angewandte Chemie International Edition*, 41(7):1188–1191, 2002.

[81] R. L. Penn and J. F. Banfield. Morphology development and crystal growth in nanocrystalline aggregates under hydrothermal conditions: insights from titania. *Geochimica et Cosmochimica Acta*, 63(10):1549–1557, 1999.

[82] R. L. Penn and J. F. Banfield. Imperfect oriented attachment: Dislocation generation in defect-free nanocrystals. *Science*, 281(5379):969–971, 1998.

[83] J. H. Yu, J. Joo, H. M. Park, S. Baik, Y. W. Kim, S. C. Kim, and T. Hyeon. Synthesis of quantum-sized cubic ZnS nanorods by the oriented attachment mechanism. *Journal of the American Chemical Society*, 127(15):5662–5670, 2005.

[84] E. E. Finney and R. G. Finke. The four-step, double-autocatalytic mechanism for transition-metal nanocluster nucleation, growth, and then agglomeration: Metal, ligand, concentration, temperature, and solvent dependency studies. *Chemistry of Materials*, 20(5):1956–1970, 2008.

[85] H. Zheng, R. K. Smith, Y. Jun, C. Kisielowski, U. Dahmen, and A. P. Alivisatos. Observation of single colloidal platinum nanocrystal growth trajectories. *Science*, 324(5932):1309–1312, 2009.

[86] A. Dippel, K. M. O. Jensen, C. Tyrsted, M. Bremholm, E. D. Bojesen, D. Saha, S. Birgisson, M. Christensen, S. J. L. Billinge, and B. B. Iversen. Towards atomistic understanding of polymorphism in the solvothermal synthesis of ZrO_2 nanoparticles. *Acta Crystallographica Section A*, 72(6):645–650, 2016.

[87] C. Tyrsted, N. Lock, K.M.Ø. Jensen, M. Christensen, E.D. Bøjesen, H. Emerich, G. Vaughan, S.J.L. Billinge, and B.B. Iversen. Evolution of atomic structure during nanoparticle formation. *IUCrJ*, page 165–171, 2014.

[88] S. Shaw, J. L. Colaux, J. L. Hay, F. C. Peiris, and L. Cademartiri. Building materials from colloidal nanocrystal arrays: Evolution of structure, composition, and mechanical properties upon the removal of ligands by O_2 plasma. *Advanced Materials*, 28(40):8900–8905, 2016.

[89] S. Shaw, T. F. Silva, J. M. Bobbitt, F. Naab, C. L. Rodrigues, B. Yuan, J. J. Chang, X. Tian, E. A. Smith, and L. Cademartiri. Building materials from colloidal nanocrystal assemblies: Molecular control of solid/solid interfaces in nanostructured tetragonal ZrO_2. *Chemistry of Materials*, 29(18):7888–7900, 2017.

[90] Y. Wang, I. Fedin, H. Zhang, and D. V. Talapin. Direct optical lithography of functional inorganic nanomaterials. *Science*, 357(6349):385–388, 2017.

[91] J. Pan, Z. Rong, Y. Wang, H. Cho, I. Coropceanu, H. Wu, and D. V. Talapin. Direct optical lithography of colloidal metal oxide nanomaterials for diffractive optical elements with 2π phase control. *Journal of the American Chemical Society*, 2021.

[92] P. Tao, Y. Li, R. W. Siegel, and L. S. Schadler. Transparent dispensible high-refractive index ZrO_2 / epoxy nanocomposites for LED encapsulation. *Journal of Applied Polymer Science*, 130(5):3785–3793, 2013.

[93] K. De Keukeleere, P. Cayado, A. Meledin, F. Vallès, J. De Roo, H. Rijckaert, G. Pollefeyt,

E. Bruneel, A. Palau, and M. Coll. Superconducting $YBa_2Cu_3O_{7-\delta}$ nanocomposites using preformed ZrO_2 nanocrystals: Growth mechanisms and vortex pinning properties. *Advanced Electronic Materials*, 2(10):1600161, 2016.

[94] H. Rijckaert, G. Pollefeyt, M. Sieger, J. Hanisch, J. Bennewitz, K. De Keukeleere, J. De Roo, R. Huhne, M. Backer, and P. and Paturi. Optimizing nanocomposites through nanocrystal surface chemistry: Superconducting $YBa_2Cu_3O_7$ thin films via low-fluorine metal organic deposition and preformed metal oxide nanocrystals. *Chemistry of Materials*, 29(14):6104–6113, 2017.

[95] J. Wang, S. Choudhary, J. De Roo, K. De Keukeleere, I. Van Driessche, A. J. Crosby, and S. S. Nonnenmann. How ligands affect resistive switching in solution-processed HfO_2 nanoparticle assemblies. *ACS Applied Materials and Interfaces*, 10(5):4824–4830, 2018.

[96] Y. Min, J. M. Caster, M. J. Eblan, and A. Z. Wang. Clinical translation of nanomedicine. *Chemical Reviews*, 115(19):11147–90, 2015.

[97] L. Maggiorella, G. Barouch, C. Devaux, A. Pottier, E. Deutsch, J. Bourhis, E. Borghi, and L. Levy. Nanoscale radiotherapy with hafnium oxide nanoparticles. *Future Oncology*, 8(9):1167–1181, 2012.

[98] J. Marill, N. Anesary, P. Zhang, S. Vivet, E. Borghi, L. Levy, and A. Pottier. Hafnium oxide nanoparticles: Toward an in vitro predictive biological effect? *Radiation Oncology*, 9(1):150, 2014.

[99] C. Liu, T. J. Hajagos, D. Kishpaugh, Y. Jin, W. Hu, Q. Chen, and Q. Pei. Facile single-precursor synthesis and surface modification of hafnium oxide nanoparticles for nanocomposite γ-ray scintillators. *Advanced Functional Materials*, 25(29):4607–4616, 2015.

[100] T. L. McGinnity, O. Dominguez, T. E. Curtis, P. D. Nallathamby, A. J. Hoffman, and R. K. Roeder. Hafnia (HfO_2) nanoparticles as an X-ray contrast agent and mid-infrared biosensor. *Nanoscale*, 8(28):13627–13637, 2016.

[101] I. Villa, C. Villa, A. Monguzzi, V. Babin, E. Tervoort, M. Nikl, M. Niederberger, Y. Torrente, A. Vedda, and A. Lauria. Demonstration of cellular imaging by using luminescent and anti-cytotoxic europium-doped hafnia nanocrystals. *Nanoscale*, 10(17):7933–7940, 2018.

[102] J. De Roo, I. Van Driessche, J. C. Martins, and Z. Hens. Colloidal metal oxide nanocrystal catalysis

by sustained chemically driven ligand displacement. *Nat. Materials*, 15(5):517–521, 2016.

[103] S. J. L. Billinge and L. Igor. The problem with determining atomic structure at the nanoscale. *Science*, 27(316(5824)):561–565, 2007.

[104] T. Egami and S. J. L. Billinge. Underneath the bragg peaks structural analysis of complex materials. *Materials Today*, 6, 2003.

[105] M. J. Cliffe, M. T. Dove, D. A. Drabold, and A. L. Goodwin. Structure determination of disordered materials from diffraction data. *Physical Review Letters*, 104(12):125501–125504, 2010.

[106] S. J. L. Billinge. The rise of the X-ray atomic pair distribution function method: a series of fortunate events. *Philosophical Transactions of the Royal Society A: Mathematical, Physical and Engineering Sciences*, 377(2147):20180413, 2019.

[107] X. Yang, P. Juhás, C. L. Farrow, and S. J. L. Billinge. xPDFsuite: an end-to-end software solution for high throughput pair distribution function transformation, visualization and analysis. *arXiv preprint arXiv:1402.3163*, 2014.

[108] M. W. Terban and S. J. L. Billinge. Structural analysis of molecular materials using the pair distribution function. *Chemical Reviews*, 122(1):1208–1272, 2022.

[109] S. J. L. Billinge, S. H. Skjaervoe, M. W. Terban, S. Tao, L. Yang, Y. Rakita, and B. A. Frandsen. Local structure determination using total scattering data. *Comprehensive Inorganic Chemistry III (Third Edition)*, pages 222–247, 2023.

[110] J. K. Mathiesen, J. Quinson, S. Blaseio, E. T. S. Kjær, A. Dworzak, S. R. Cooper, J. K. Pedersen, B. Wang, F. Bizzotto, J. Schröder, T. L. Kinnibrugh, S. B. Simonsen, K. L. Theil, J. J. K. Kirkensgaard, J. Rossmeisl, M. Oezaslan, M. Arenz, and K. M. Ø Jensen. Chemical insights into the formation of colloidal iridium nanoparticles from in situ X-ray total scattering: Influence of precursors and cations on the reaction pathway. *Journal of the American Chemical Society*, 145(3):1769–1782, 2023.

[111] S. L. Skjærvø, A. S. Anker, M. C. Wied, E. T. S. Kjær, M. Juelsholt, T. L. Christiansen, and K. M. Ø. Jensen. Atomic structural changes in the formation of transition metal tungstates: the role of polyoxometalate structures in material crystallization. *Chemical Science*, 2023.

[112] C. L. Farrow, P. Juhás, J. W. Liu, D. Bryndin, E. S. Božin, J. Bloch, Th Proffen, and S. J. L. Billinge. PDFfit2 and PDFgui: computer programs for studying nanostructure in crystals. *Journal of Physics: Condensed Matter*, 19(33):335219, 2007.

[113] P. Juhás, C. L. Farrow, X. Yang, K. R. Knox, and S. J. L. Billinge. Complex modeling: a strategy and software program for combining multiple information sources to solve ill posed structure and nanostructure inverse problems. *Acta Crystallographica*, 71:562–568, 2015.

[114] M. G. Tucker, D. A. Keen, M. T. Dove, A. L. Goodwin, and Q. Hui. Rmcprofile: reverse monte carlo for polycrystalline materials. *Journal of Physics: Condensed Matter*, 19(33), 2007.

[115] SAS portal, http://smallangle.org/.

[116] J. O. Cross, R. L. Opila, I. W. Boyd, and E. N. Kaufmann. Materials characterization and the evolution of materials. *MRS Bulletin*, 40(12):1019–1034, 2015.

"The will must be stronger than the skill"

- Muhammad Ali

Chapter 2

Precursor chemistry during the colloidal synthesis of ZrO_2 nanocrystals[†]

2.1 Introduction

Compared to TiO_2 and HfO_2, ZrO_2 nanocrystals produced in TOPO are the most monodisperse and feature the best colloidal stability. It is worth examining the proposed reaction scheme more closely (Fig. 2.1).[1] Slightly more $ZrCl_4$ (1.25 equivalents) was added to compensate for the isopropanol molecule coordinated to the zirconium isopropoxide precursor. Isopropyl chloride and propene were determined to be by-products *via* gas chromatography. Presumably, isopropyl chloride is formed in the same way as for TiO_2 (S_N1 nucleophilic substitution). The isopropyl chloride is believed to undergo dehydrohalogenation to propene. Note that it is also possible to replace $ZrCl_4$ with its tetrahydrofuran complex ($ZrCl_4$.2THF) to improve the solubility of the chloride.[2] Using $ZrCl_4$, the synthesis produces 4 nm nanocrystals while 3 nm nanocrystals are obtained with $ZrBr_4$. However, no further size tuning has been reported. This is a clear limitation of the current state-of-the-art, especially when compared to the exquisite size control exerted in the field of semiconductor quantum dots (e.g., PbS).[3] Finally, the yield of this reaction seems limited to about 50%.[2,4]

[†]This chapter is adapted from: Mechanistic insight into the precursor chemistry of ZrO_2 and HfO_2 Nanocrystals; towards Size-Tunable Syntheses. Rohan Pokratath, Dietger Van den Eynden, Susan Rudd Cooper, Jette Katja Mathiesen, Valérie Waser, Mike Devereux, Simon J. L. Billinge, Markus Meuwly, Kirsten M. Ø. Jensen, and Jonathan De Roo, JACS Au, 2, 4, 827-838, 2022, DOI: 10.1021/jacsau.1c00568.

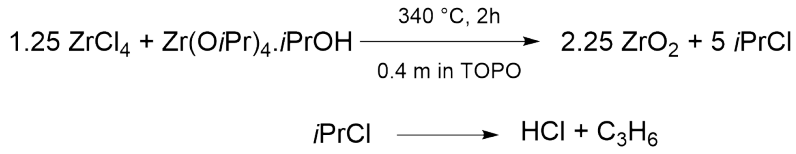

Fig. 2.1 | The proposed reaction scheme of ZrO_2 nanocrystal formation. The proposed reaction scheme of $ZrCl_4$ and zirconium isopropoxide isopropanol complex, reacting towards ZrO_2 nanocrystals, according to Joo *et al.*[1]

In this chapter, we aim at obtaining deeper insight into the precursor chemistry of these nanocrystal reactions, and we aim at introducing size tunability. We first analyze the speciation of the precursors using solution ^{1}H and ^{31}P NMR spectroscopy, supported by density functional theory (DFT) calculations to better understand their interaction with the coordinating solvent, TOPO. Second, by using control experiments and independent synthesis of the proposed species, we identify the actual reaction precursors; mixed chloroalkoxides. Furthermore, we reveal an alternative mechanism based on E1 elimination, which is happening in parallel to the earlier proposed S_N1 mechanism and we thus come to an overall, fully balanced reaction equation. We confirm the formation of $ZrCl_4$ as a by-product by NMR and X-ray total scattering studies. Finally, using our insight into the reaction mechanism, we then increase the yield of the reaction, while also providing a way to tune the final nanocrystal size.

2.2 Results and Discussion

2.2.1 Interaction of TOPO with zirconium chloride

We first investigate the speciation of the precursors and their interaction with the coordinating solvent; tri-*n*-octylphosphine oxide (TOPO). Starting from the soluble THF complex of $ZrCl_4$ in $CDCl_3$, we gradually add TOPO (as a 0.5 M solution in $CDCl_3$) and monitor the reaction by ^{1}H and ^{31}P NMR (Fig. 2.2). The resonances of THF bound to $ZrCl_4$ (a' and b') are shifted to higher ppm values compared to free THF (a and b), see Fig. 2.2b. Upon addition of TOPO, we observe a decrease in the a' and b' resonances, and resonance a shows up initially as a very broad resonance around 4 ppm and then sharpens and shifts to 3.74 ppm. We also clearly observe the growth of resonance 1' (2.11 ppm, TOPO bound to $ZrCl_4$) up to two equivalents of TOPO. It is only by the third TOPO equivalent, that resonance 1 of free TOPO is observed. These observations indicate that TOPO irreversibly displaces THF from the $ZrCl_4$ complex, in a Lewis base exchange reaction. The

stoichiometry is corroborated by the relative integrals of free THF and bound TOPO (Supplementary Fig. A.1). The ^{31}P NMR spectrum yields even more insight into the speciation (Fig. 2.2c). The resonance at 74.8 ppm is the main product after the addition of two equivalents TOPO and is assigned to the double TOPO adduct of $ZrCl_4$ (2), see Fig. 2.2c. This is verified by the direct synthesis of (2) from $ZrCl_4$ and 2 equivalents of TOPO (see Supplementary Fig. A.2). In C_6D_6, (2) appears at 73 ppm (Supplementary Fig. A.3). A Job plot of (2) also confirms the stoichiometry of two TOPO molecules per zirconium center (see Supplementary Fig. A.4).[5]

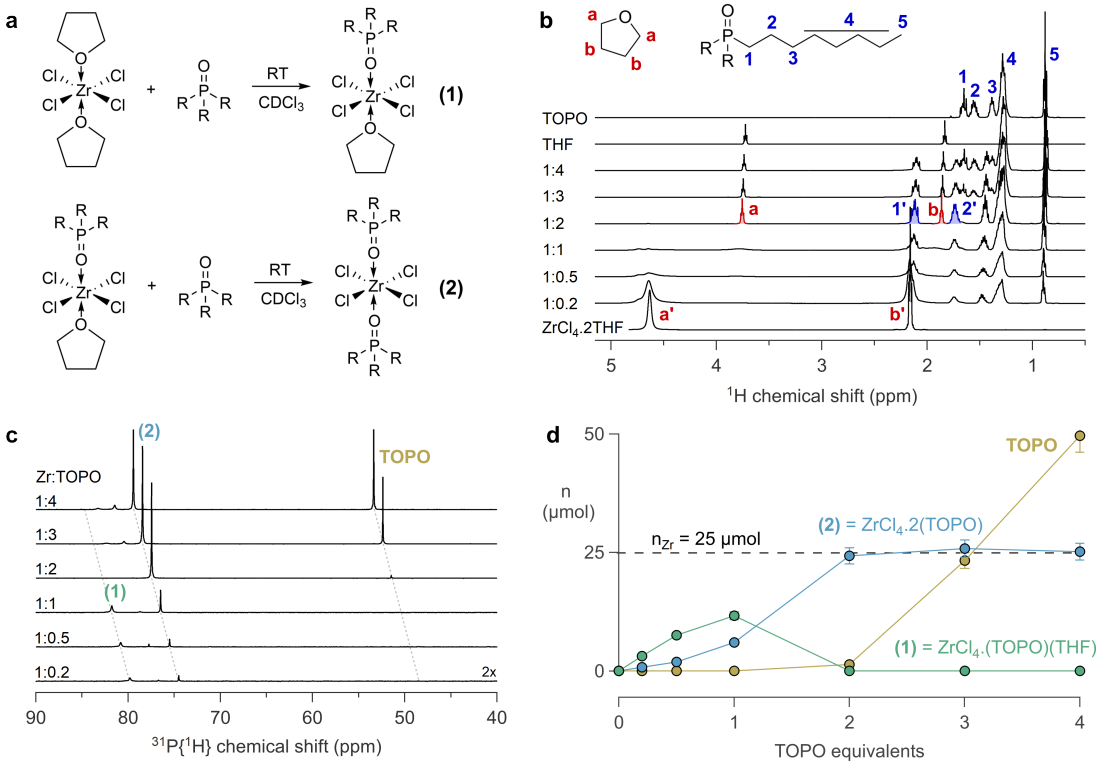

Fig. 2.2 | Interation of TOPO with $ZrCl_4$.2THF. a Scheme for the reaction of $ZrCl_4$.2THF with TOPO. **b** ^{1}H NMR of the titration of a solution of 0.05 M $ZrCl_4$.2THF in $CDCl_3$ with increasing equivalents of TOPO. The latter is added as a 0.5 M solution, gradually diluting the zirconium complex. **c** ^{31}P NMR of the same titration. The spectrum for 0.2 equivalents was amplified twofold to observe the resonances more clearly. The spectra have a relative x-offset of 1 ppm with respect to each other. **d** The different TOPO species over the course of the titration. The total amount of Zr in the sample was 25 μmol.

The resonance at 79.8 ppm is assigned to complex (1) based on its higher chemical shift (indicating a higher Lewis acidity of the metal center).[6–8] After adding the third TOPO equivalent, free TOPO is observed at 48 ppm in the ^{31}P NMR spectrum, consistent with our analysis of the ^{1}H NMR spectrum (Fig. 2.2b). Based on the integrals of the ^{31}P NMR spectrum, we calculate the amount of each species present during the titration (Fig. 2.2d). It is clear that (1) is a transient

species en route to (2). Note that (2) is formed together with (1), even at low equivalents, indicating that the second exchange is competitive with the first exchange. After two equivalents of TOPO added, all $ZrCl_4$ is coordinated with two TOPO ligands. Indeed, TOPO is a much stronger Lewis base than THF according to the $SbCl_5$ affinity scale (592 kJ/mol vs. 368.2 kJ/mol).[9] This further underscores our assignment of (1) since the weakly basic THF leaves the zirconium center in (1) more Lewis acidic, causing a higher ^{31}P NMR chemical shift.

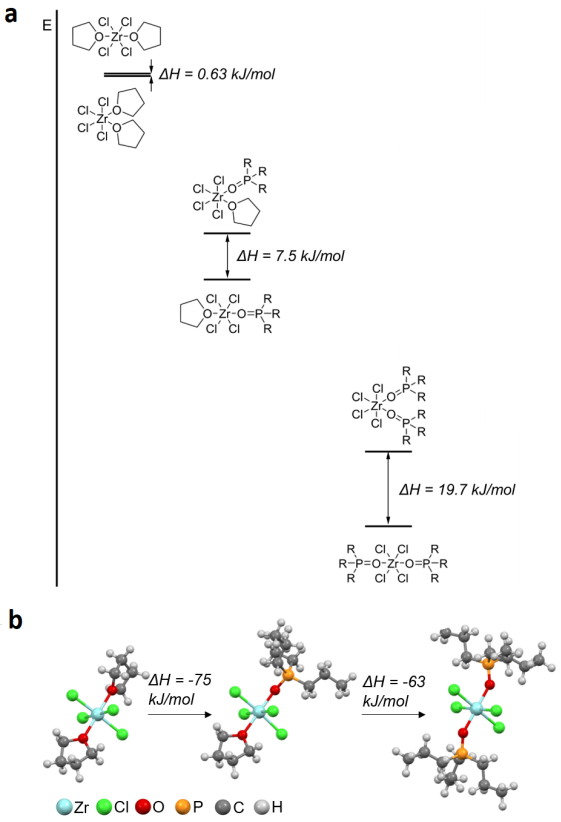

Fig. 2.3 | The exchange reaction between the $ZrCl_4$.2THF and tri-n-propylphosphine oxide ligands. a Scheme showing the exchange reaction between the $ZrCl_4$.2THF and tri-n-propylphosphine oxide ligands, comparing both *cis* and *trans* structures (R = propyl chain). **b** ΔH of the exchange reactions for the *trans* complexes and their corresponding optimized structures at the B3LYP/ aug-cc-pVDZ level of theory.

Having established the stoichiometry of the final complex (2), we turn to its geometry. Single crystal data shows that $ZrCl_4$.2THF has a *cis* geometry in the solid-state,[10] however, TOPO is more sterically demanding. Unfortunately, we were unsuccessful in crystallizing (2) or any of its shorter chain derivatives with, e.g., triethylphosphine oxide. We also deemed triphenylphosphine oxide not a representative substitute, given its larger Tolmann cone angle and lower basicity, compared to trialkylphosphines.[11] Therefore, using calculations at the density functional theory (B3LYP) level of

theory, the energy minimized structure for the $ZrCl_4$.2THF, $ZrCl_4$.(THF)(TPPO), and $ZrCl_4$.2TPPO complexes were determined with tri-n-propylphosphine oxide (TPPO) instead of TOPO as the ligand. Comparing the optimized structures of *cis* and *trans* $ZrCl_4$.2THF, we find only a negligible energy difference (0.6 kJ/mol), see Fig. 2.3. Since the *cis* isomer has a dipole moment, dipole-dipole interactions might explain the observation of the *cis* isomer in the solid state crystal structure.[10] Comparing the bond lengths in the latter (Zr-Cl: 2.39 Å and 2.42 Å; Zr-O: 2.23 Å and 2.24 Å) with the DFT optimized structure (Zr-Cl: 2.39 Å and 2.45 Å; Zr-O: 2.34 Å), we find good agreement thus providing confidence in the quantum chemical calculations. Upon substitution of THF for TPPO, we find that the energy difference between the isomers progressively increases (Fig. 2.3). The *trans* conformer is more stable by 7.5 kJ/mol and 20 kJ/mol for the single and double exchanges, respectively. Taking the *trans* complexes for each stoichiometry as the reference, we calculate the change in enthalpy (ΔH) for the exchange reactions. The first exchange accounts for -75 kJ/mol and the second is only slightly less exothermic (-63 kJ/mol) and thus competitive with the first exchange, which is consistent with our NMR experiments.

2.2.2 Interaction of TOPO with zirconium isopropoxide isopropanol complex

We find an interesting contrast by performing the same experiment with the zirconium isopropoxide isopropanol complex (Fig. 2.4). It was previously shown that this complex is a dimer, in the solid-state and in solution.[12] In the ^{1}H NMR spectrum of Zr(O*i*Pr)$_4$.*i*PrOH, we find resonance a' of isopropanol (CH) as a single broad peak at 4.4 ppm, while it should appear at 4.1 ppm for pure isopropanol (Fig. 2.4). This is consistent with the coordination of isopropoxide/isopropanol to Zr and indicates that all CH protons have a roughly similar chemical environment. We also observe a very broad resonance at 5.2 ppm which integrates to one, when the CH integral integrates to five (Supplementary Fig. A.5). We assign this resonance to the alcoholic proton (OH) of the coordinated isopropanol. The resonance is shifted considerably compared to free isopropanol in $CDCl_3$ (2.16 ppm).[13] Indeed, coordination of isopropanol with zirconium renders the alcohol proton more acidic.

Upon addition of 0.2 equivalents of TOPO relative to Zr, resonance a' splits in two (1:4 ratio). We assign the least intense resonance at 4.5 ppm to the bridging isopropoxide in the dimer. Upon the addition of more TOPO, the more intense resonance splits again in two. Resonance a at 4.1 ppm accounts for 20% of the total CH integral and is assigned to isopropanol. Isopropanol is in a fast exchange between a free and acoordinated state since resonance a sharpens up and shifts upon gradual TOPO addition. The resonance a' at 4.3 ppm is assigned to non-bridging isopropoxide. We observe

the bound TOPO resonance 1' at 1.96 ppm. This value is slightly lower than the 2.11 ppm found for TOPO bound to $ZrCl_4$ and is consistent with the lower expected Lewis acidity of $Zr(OiPr)_4$. In the ^{31}P NMR spectrum, we find a single species (3) at 63 ppm, apart from the resonance of free TOPO (Supplementary Fig. A.6a). We hypothesized three possible structures for (3), which differ in their TOPO-to-zirconium stoichiometry (Supplementary Fig. A.7). A Job plot of (3) is most consistent with a Zr:TOPO stoichiometry of 1:0.5 (Supplementary Fig. A.8), and we thus propose a dimer with a single TOPO ligand, see Fig. 2.4a. This species appears not to be thermodynamically favored and is in equilibrium with free TOPO. Even at only 0.2 TOPO equivalents, we observe free TOPO in both the ^{1}H and ^{31}P NMR spectrum. Integration of the ^{31}P NMR shows that only a small amount of (3) is formed (Supplementary Fig. A.6b). Even when TOPO is added in excess (4 eq), only 9 μmol of (3) is formed, while the total amount of Zr dimer is 12.5 μmol. This is a surprising result since isopropanol is even slightly less Lewis basic than THF (Supplementary Fig. A.9) and thus much weaker than TOPO. However, DFT calculations show that the exchange of isopropanol for TPPO is endothermic with the least positive ΔH for our hypothesized structure (3), see Supplementary Fig. A.10. It is thus clear that intramolecular hydrogen bonding stabilizes the $Zr(OiPr)_4.i$PrOH dimer.

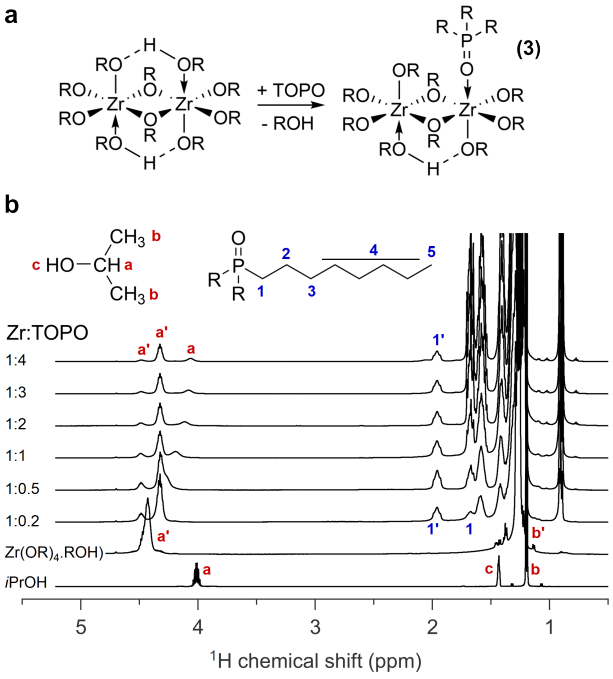

Fig. 2.4 | **Interaction of zirconium isopropoxide with TOPO. a** Scheme for the reaction of $Zr(OiPr)_4.i$PrOH with TOPO. **b** ^{1}H NMR of the titration of a solution of 0.05 M $Zr(OiPr)_4.i$PrOH in $CDCl_3$ with increasing equivalents of TOPO relative to Zr. TOPO is added as a 0.5 M solution, gradually diluting the zirconium complex. The total amount of Zr in the sample was 25 μmol.

2.2.3 Interaction of precursor mixtures with TOPO

In the literature, a 1.25:1 mixture of $ZrCl_4$ and $Zr(OiPr)_4.iPrOH$ is typically used to synthesize ZrO_2 nanocrystals.[1,2,14] This approach assumes that the extra 0.25 equivalents $ZrCl_4$ react with the coordinated isopropanol of $Zr(OiPr)_4.iPrOH$. Here we test the validity of that hypothesis. Mixing 1.25 eq of $ZrCl_4.2THF$ with 1 eq. of $Zr(OiPr)_4.iPrOH$ and titrating it with TOPO (Supplementary Fig. A.11), we observe unambiguously the resonance of free isopropanol at 4.1 ppm, indicating that the coordinated isopropanol does not react with the excess $ZrCl_4$. We rationalize this as follows. It is known that metathesis occurs by mixing metal complexes, randomly distributing the ligands over the available metal centers.[15,16] Therefore, we can write

$$1.25\ ZrCl_4 + Zr(OiPr)_4 \cdot iPrOH \longrightarrow 0.5\ ZrCl_3(OiPr) + 1.75\ ZrCl_2(OiPr)_2 + iPrOH \qquad (2.1)$$

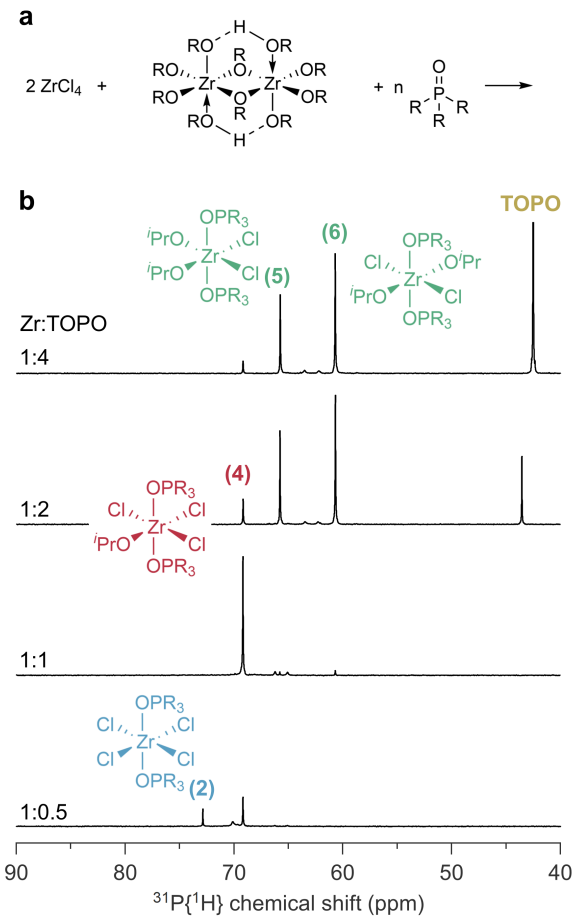

Fig. 2.5 | The titration of a 1 : 1 reaction mixture with TOPO. a Reaction scheme for the titration of a 1 : 1 mixture of $ZrCl_4$: $Zr(OiPr)_4.iPrOH$ with TOPO in C_6D_6 at room temperature. **b** The ^{31}P NMR spectra of the titration. The ratio of Zr to TOPO is indicated in the figure.

We also know that $ZrCl_4$ only reacts with a single equivalent of alcohol, even when the alcohol is in excess.[17] This means that $ZrCl_3(OR)$ is unreactive to alcohols. Therefore, the above $ZrCl_3(OiPr)$ and $ZrCl_2(OiPr)_2$ (produced from mixing the reagents) do not react further with isopropanol.

$$ZrCl_4 + \text{excess ROH} \longrightarrow ZrCl_3(OR) \cdot 2\,ROH + HCl \tag{2.2}$$

To gain further insight into the speciation, we turned to ^{31}P NMR. Unfortunately, the ^{31}P NMR spectrum of the precursor mixture in $CDCl_3$ is highly complex (Supplementary Fig. A.11), most likely due to the hydrogen bonding capabilities of $CDCl_3$. The spectrum in deuterated benzene is more convenient to analyze. Again, we observe the free isopropanol in the proton NMR spectrum, integrating for one while the isopropoxide resonance integrates for four (Supplementary Fig. A.12). Focusing below only on equimolar mixtures, we titrated the precursor mixture with TOPO. In the ^{31}P NMR spectrum (Fig. 2.5), we observe the previously identified (2) at 0.5 TOPO equivalents. At one equivalent TOPO, a single species (4) is observed at 69 ppm, which we identified as $ZrCl_3(OiPr).2TOPO$. This is corroborated by the direct synthesis of (4), either by reacting $ZrCl_4$ with dry isopropanol (Equation 2.2) or by reacting $Zr(OiPr)_4.iPrOH$ with acetyl chloride (Equation 2.3),[18] see Supplementary Fig. A.13a. The Job plot indicates again 2 TOPO ligands per zirconium center (Supplementary Fig. A.13b-c).

$$Zr(OiPr)_4 \cdot iPrOH + n\ AcCl \longrightarrow ZrCl_n(OiPr)_{(4-n)} + n\ AcOiPr + iPrOH \tag{2.3}$$

Upon addition of more TOPO, the resonance of (4) decreases again in intensity and new species (5) and (6) appear (at 65.7 and 60.7 ppm), which we assign as the two isomers of $ZrCl_2(OiPr)_2.2TOPO$ and which are the expected products of an equimolar mixture. The chemical identity of $ZrCl_2(OiPr)_2.2TOPO$ is again corroborated by the direct synthesis of $ZrCl_2(OiPr)_2.2TOPO$ *via* Equation 2.3 and the TOPO stoichiometry is confirmed by a Job plot (Supplementary Fig. A.14). The relative Lewis acidity of isomers (5) and (6) was estimated *via* DFT calculations. We calculated the enthalpy change upon removal of one TOPO molecule from the structure (i.e., dissociation of the Lewis acid-base adduct). The ΔH was more positive for the *cis* structure (5) than for the *trans* structure (6), thus suggesting that (5) is more Lewis acidic and has a higher ^{31}P chemical shift (Supplementary Fig. A.15). To further confirm the structural assignments of (5) and (6), ^{31}P chemical shifts for 6 compounds were determined from DFT calculations. The

chemical shifts for the validation compounds (1), (2), (4) and TOPO were correctly ranked and the difference between computed and observed chemical shifts was between -0.7 ppm and +1.4 ppm compared to the absolute chemical shifts ranging from 42.0 ppm to 79.8 ppm; see Supplementary Table A.3. Given that for compounds (5) and (6) the experimental difference is 4.9 ppm, the accuracy of the computations (2 ppm) is sufficient to assign their structures from computed ^{31}P shifts. Indeed, species (5) has a computed δ = 66.1 ppm whereas (6) is shifted down to δ = 62.9 ppm consistent with the experimentally determined shifts (66.4 and 61.5 respectively). Overall, the computed chemical shifts correlate linearly (R^2 = 0.996) with the experimental values (Supplementary Fig. A.16). Further validation can be gleaned from computed ^{1}H shifts at the same level of theory; see Supplementary Table A.4. Hence the computed chemical shifts for the DFT-optimized structures support our assignments in Fig. 2.5.

Finally, we mixed $ZrCl_4$ and $Zr(OiPr)_4.i$PrOH in the ratio 0.5:1, 1:1, 2:1, and 3:1 (with 2 TOPO equivalents), and observed the expected species in the ^{31}P NMR spectrum (Supplementary Fig. A.17):

$$0.5\ ZrCl_4 + Zr(OiPr)_4 \cdot iPrOH \longrightarrow 0.5\ ZrCl_2(OiPr)_2 + ZrCl(OiPr)_3 + iPrOH \tag{2.4}$$

$$ZrCl_4 + Zr(OiPr)_4 \cdot iPrOH \longrightarrow 2\ ZrCl_2(OiPr)_2 + iPrOH \tag{2.5}$$

$$2\ ZrCl_4 + Zr(OiPr)_4 \cdot iPrOH \longrightarrow 2\ ZrCl_3(OiPr) + ZrCl_2(OiPr)_2 + iPrOH \tag{2.6}$$

$$3\ ZrCl_4 + Zr(OiPr)_4 \cdot iPrOH \longrightarrow 4\ ZrCl_3(OiPr) + iPrOH \tag{2.7}$$

We also confirmed the ^{31}P NMR shift of $ZrCl(OiPr)_3$.2TOPO (7) as 58.7 ppm by synthesizing it according to Equation 2.3, Supplementary Fig. A.18. The Lewis acidity of the different zirconium species (2) - (7) decreases with every Cl to O*i*Pr substitution and this is evident by the progressive shift to lower ppm values and also by the presence of free TOPO in case of $ZrCl_2(OiPr)_2$.2TOPO and $ZrCl(OiPr)_3$.2TOPO. For the latter two, coordination of TOPO appears an equilibrium instead of a complete reaction.

From the titration in Fig. 2.5 and the Job plots in Supplementary Fig. A.13, A.14, and A.18, it appears that, at lower than two TOPO equivalents, more Lewis acidic species are formed than expected based on the composition of the mixture. We infer that TOPO, as a strong Lewis base, causes a ligand redistribution of the precursor mixture to maximize the strength of the formed

Lewis acid-base complexes. Taking for example $ZrCl_2(OiPr)_2$ with one equivalent of TOPO:

$$2\,ZrCl_2(OiPr)_2 + 2\,TOPO \longrightarrow ZrCl_3(OiPr)\cdot 2\,TOPO + ZrCl(OiPr)_3 \tag{2.8}$$

As such, TOPO is coordinated to the strongest Lewis acid, $ZrCl_3(OiPr)$, and only a single peak is observed in the ^{31}P NMR spectrum. Even though the species $ZrCl(OiPr)_3$ exists in solution, it is not detected by ^{31}P NMR since it is not coordinated by TOPO. To our knowledge, this is a unique and previously unreported ligand redistribution of metal complexes, induced by neutral Lewis base (L-type ligands). The only precedent for this reaction is a thermally induced ligand redistribution upon distillation of titanium chloroalkoxides.[18] Although this was called a disproportionation in 1952, the term seems currently reserved for redox reactions.

2.2.4 Evolution of species in a nanocrystal synthesis

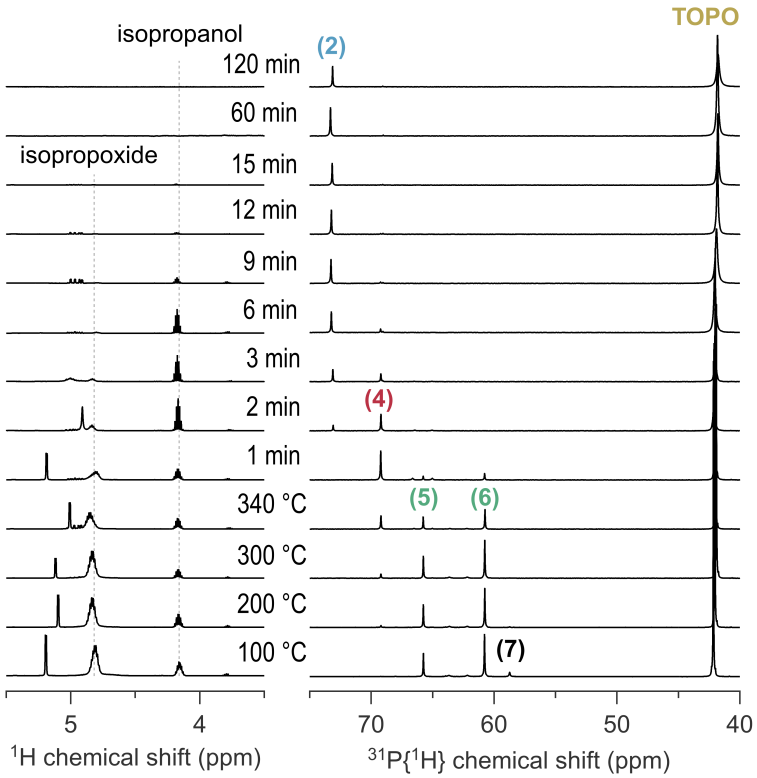

Fig. 2.6 | ^{1}H and ^{31}P NMR of the reaction aliquots. ^{1}H and ^{31}P NMR of the reaction mixture with 1 equivalent of $ZrCl_4$ in C_6D_6. Aliquots were taken at different temperatures during the ramp and at different times at the final reaction temperature of 340 °C.

Having determined the identity of all the species in ^{31}P NMR, we are now ready to investigate a real reaction (1 mmol $ZrCl_4$, 1 mmol $Zr(OiPr)_4.iPrOH$ and 13 mmol TOPO), see Fig. 2.6. The zirconium molality in the reaction is 0.4 mol/kg, corresponding to Zr:TOPO = 1:6.5. We take aliquots from the reaction mixture and measure them in ^{1}H and ^{31}P NMR (Fig. 2.6). At 100 °C, we find mostly species (5) and (6) in the ^{31}P NMR spectrum, showing that the actual reagent in this reaction is $ZrCl_2(OiPr)_2$. Upon heating to 340 °C, the isopropoxide resonance (^{1}H NMR spectrum) decreases in intensity and concomitantly, (5) and (6) decrease in concentration and $ZrCl_3(OiPr)$ (4) is formed. The precursor decomposition proceeds rapidly at 340 °C evidenced by the decay of the isopropoxide signal within 10 min. After 1 min at 340 °C, (4) is the dominant species, which then also decays within 10 min (showing thus a good correlation between the ^{1}H and ^{31}P NMR data). We clearly observe $ZrCl_4$.2TOPO (2) as a by-product of the reaction. Also, signals of free isopropanol remain present in the ^{1}H NMR spectrum up to 15 min despite its low boiling point. Isopropanol co-exists with (2), thus showing little reactivity towards $ZrCl_4$.2TOPO. This observation stands in contrast to the reactivity of isopropanol with uncoordinated $ZrCl_4$ (see Equation 2.2). The presence of (2) at the end of the reaction explains why the reaction does not reach 100% yield. After isolation of the final nanocrystals and subtraction of the organic mass (determined from TGA), we reproducibly find a yield of about 60% in ZrO_2. This value agrees perfectly with our estimation of the yield from integrating the ^{31}P NMR spectrum at the end of the reaction (Supplementary Fig. A.19). The reaction mixture with $ZrCl_4$.2THF shows qualitatively very similar trends (Supplementary Fig. A.20), but isopropanol and THF linger in the reaction mixture to the end (2 hours).

We further validate the results with X-ray total scattering and Pair Distribution Function analysis. Fig. 2.7a shows the PDF of the reaction mixture at different temperatures (100 °C, 200 °C, 300 °C, 340 °C) and after 90 minutes at 340 °C. The measurements were carried out ex-situ on corresponding reaction aliquots. We assign the three main peaks in the reaction mixture to Zr-O (2.0 Å), Zr-Cl (2.5 Å), and Zr-P (3.5 Å) which are in good agreement with the respective distances in the DFT optimized structures of (5) and (6): Zr-O (2.0 Å for OiPr and 2.2 Å for TPPO), Zr-Cl (2.5 Å for *cis* and 2.6 Å for *trans*), and Zr-P (3.5 Å). The absence of a Zr-Zr distance at 3.6 Å in the PDF data acquired below 340 °C indicates that the precursors are indeed monomers, coordinated by TOPO. A different PDF is observed after 90 min at 340 °C, where the contribution of crystalline ZrO_2 is prominent. The appearance of an intense Zr-Zr distance at 3.6 Å and the longer-range interactions above 5 Å indicate the formation of ZrO_2 nanocrystals. A single phase refinement of the data using the tetragonal (P_{42}/nmc) ZrO_2 crystal structure results in a moderately good fit (Rw =

0.26), see Supplementary Fig. A.21. While this crystal model describes the long-range interactions quite well, there is a considerable misfit below 5 Å. It is also clear from Fig. 2.7a that there are still Zr-Cl distances in the sample, which are not accounted for by the model. Therefore, we performed a dual phase refinement of tetragonal ZrO_2 and the $ZrCl_4$ complex (2), see Fig. 2.7b. For the complex, we used the $ZrCl_4$.2TPPO structure optimized by DFT with distances: Zr-O (2.1 Å), Zr-Cl (2.5 Å), and Zr-P (3.5 Å). The atomic positions were fixed during the PDF refinement and only the scale factor and the atomic displacement parameters are refined (Supplementary Table A.5). An excellent fit is obtained ($Rw = 0.12$), showing that the DFT structure is consistent with the PDF data and underscoring the results from NMR. The formation of $ZrCl_4$ as a reaction by-product is thus firmly established.

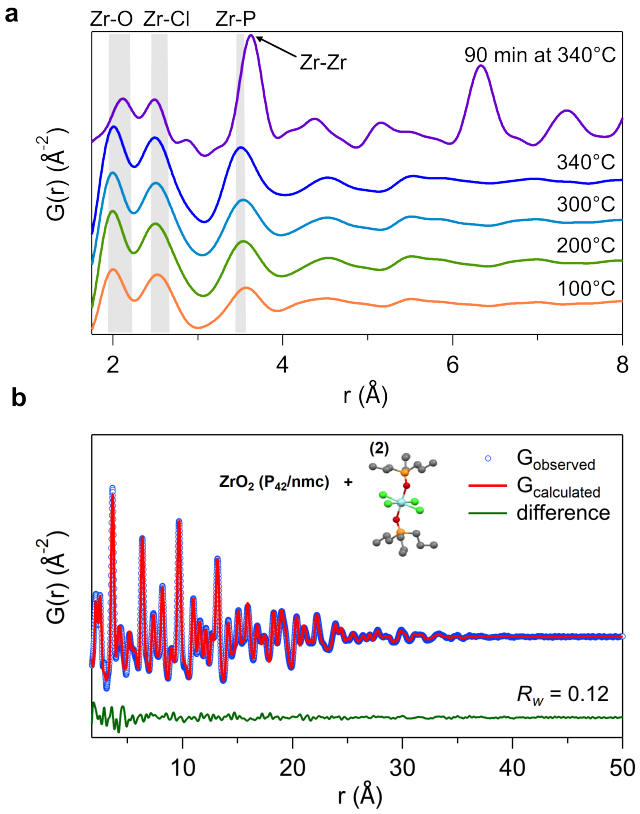

Fig. 2.7 | **X-ray PDFs analysis of the reaction aliquots. a** X-ray PDFs (acquired at 80 °C to melt TOPO) of reaction mixtures heated to different temperatures as indicated. The range of distances as determined from the DFT optimized structures of (5) and (6) are indicated by the grey zones. **b** PDF refinement for the reaction product at 340 °C after 90 min, using a dual-phase model with the tetragonal ZrO_2 ($P4_2/nmc$) and the DFT optimized $ZrCl_4$.2TEPO complex (2). The refined values are shown in Supplementary Table A.5.

2.2.5 Quantification of reagent disappearance and co-products

Based on the ^{1}H NMR spectra of Fig. 2.6 and using the methyl resonance of TOPO as the internal standard, we quantified the disappearance of isopropoxide. The same quantification was done using the ^{31}P NMR spectra, taking all species (4) - (7) together and taking into account the amount of isopropoxide in every species. For both quantifications, we assumed that the total amount of TOPO remains constant during the reaction, which is a fair assumption since only a very minor fraction decomposes.[2] Furthermore, we quantified the amount of free isopropanol in the mixture, see Fig. 2.8a. Regarding the reaction co-products, we have already identified $ZrCl_4$, but also isopropyl chloride and propene are expected based on Fig. 2.1. In earlier studies, isopropyl chloride and propene have been qualitatively detected.[1] Here, we use gas chromatography with flame ionization detection (GC-FID) to compare the relative concentration of gaseous by-products in the reaction headspace at different stages of the reaction, see Fig. 2.8b.

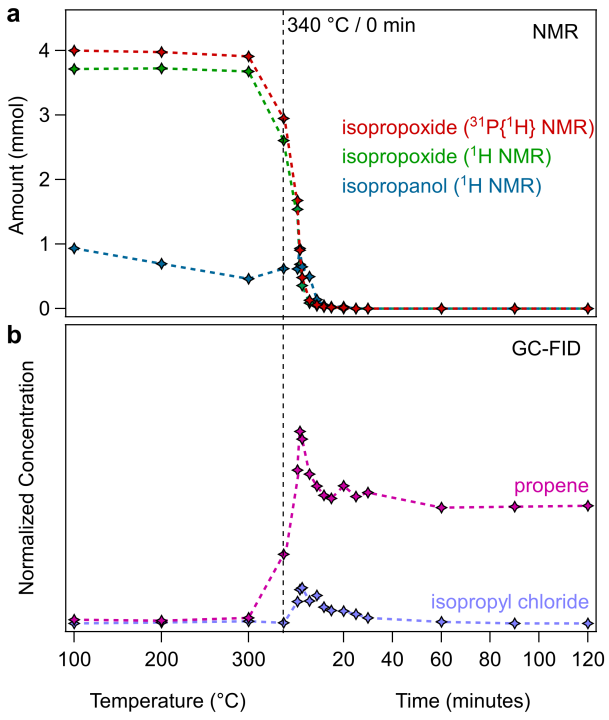

Fig. 2.8 | Quantification of reagent disappearance and co-product formation using NMR and GC-FID. a Concentration of various intermediates at different times at the final reaction temperature of 340 °C for a 1:1 mixture of $ZrCl_4$: $Zr(OiPr)_4$.*i*PrOH. The concentration of different species is calculated corresponding to the integrals of TOPO bound to the Zr-centers in ^{31}P NMR. **b** Normalized, relative concentration of propene and isopropyl chloride in the reaction headspace at different temperature/time points.

From Fig. 2.8, we learn that the isopropoxide starts decomposing between 300 °C and 340 °C. Interestingly, this coincides with an increase in detected isopropanol, while it was decreasing (evaporating) during the heat-up. This observation suggests that isopropanol is being released during the reaction and is thus also a co-product. Concomitant with the isopropoxide disappearance, we detect propene at 340 °C, the concentration of which reaches a maximum at 5 min at 340 °C. Isopropyl chloride is also detected but in lower concentrations. It was earlier proposed that isopropyl chloride is the actual reaction product and subsequently decomposes into HCl and propene. However, we find that propene appears before isopropyl chloride. Control experiments indicate that isopropyl chloride is indeed converted into propene, but the rate of this transformation is moderate and does not support an instantaneous conversion of isopropyl chloride (Supplementary Fig. A.22). For this reason, we infer that propene is also the direct reaction product of the decomposition of isopropoxide. Note that pure zirconium isopropoxide also thermally decomposes around 340 °C, yielding propene and isopropanol as co-products, thus further strengthening our hypothesis.[19]

2.2.6 The overall reaction mechanism

From the above data, we conclude that the reaction mechanism is not only based on S_N1 nucleophilic substitution (producing isopropyl chloride) but also on the E1 elimination mechanism. We propose a simplified pathway in Fig. 2.9, that agrees with all our observations. First, one isopropyl group in $ZrCl_2(OiPr)_2$ leaves as a cation and further eliminates a proton, forming both propene and a Zr-OH moiety. Second, the zirconium complex undergoes ligand redistribution, forming both $ZrCl_4$ and $Zr(OH)_2(OiPr)_2$. Third, the latter condenses into ZrO_2, eliminating two isopropanol molecules. Of course, reality will be more complex. The ligand redistribution and condensation steps most likely happen simultaneously. In addition, other condensation steps can be conceived, with the elimination of HCl or water. However, both these elimination products can react with the isopropoxide groups, releasing isopropanol and the overall sum of the reactions will be the same as the one presented in Fig. 2.9. Note, we do not propose that the ZrO_2 unit is formed as the monomer in this reaction. The current reaction scheme is highlighting the formation of organic by-products and remains agnostic as to the precise crystallization mechanism of ZrO_2. For example, the transient formation of HCl could be important to introduce the necessary reversibility in bond making and breaking that is required for crystallization. The merit of Fig. 2.9 lies in providing a fully balanced chemical equation for the reaction. From this chemical equation, it is self-evident that the reaction is limited to a 50% yield. The fact that the experimentally observed yield is 60% and that isopropyl chloride is also detected as

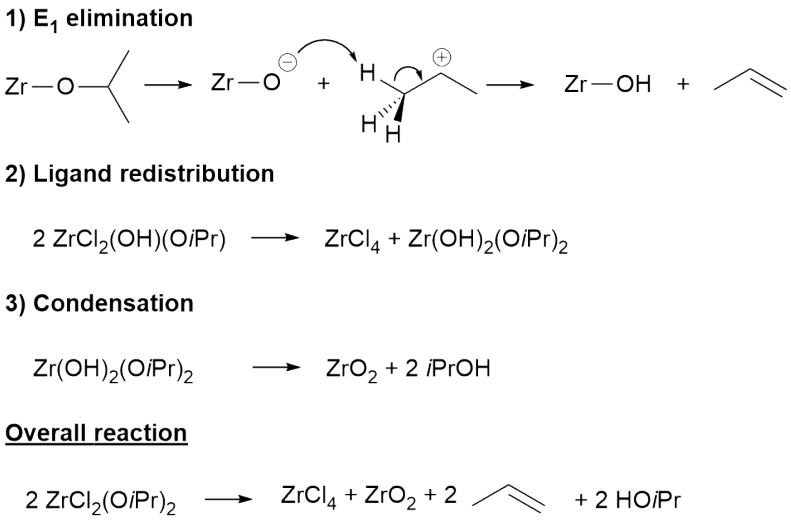

Fig. 2.9 | Our alternative pathway for the formation of ZrO_2 nanocrystals is based on E1 elimination, ligand redistribution, and condensation reactions.

a co-product, means that both the E1 elimination and the S_N1 mechanism are active simultaneously. Indeed, for the S_N1 mechanism, one can expect a theoretical yield of 100%:

$$ZrCl_2(OiPr)_2 \longrightarrow ZrO_2 + 2\ i\text{PrCl} \tag{2.9}$$

Given that 40% of zirconium is retrieved as $ZrCl_4$ at the end of the reaction, we estimate the relative contribution of the E1 and S_N1 mechanism as 80/20.

2.2.7 Size control and yield optimization

With the reaction mechanism at hand, we can introduce control over the nanocrystal size, while at the same time improving the chemical yield. We repeatedly injected $Zr(OiPr)_4.i$PrOH in the reaction flask, hypothesizing that it would undergo ligand redistribution with the $ZrCl_4$ by-product and form the active precursor once again (Fig. 2.10a). ^{1}H and ^{31}P NMR measurements of aliquots taken before and after each injection, confirm that $ZrCl_4$ is converted to the mixed chloroalkoxide species upon injection of $Zr(OiPr)_4.i$PrOH (Supplementary Fig. A.23). Each time, less $ZrCl_4$ is regenerated before the next injection. By TEM analysis we observe that the ZrO_2 nanocrystals grow from their usual 4.1 ± 0.4 nm (diameter) to 4.7 ± 0.5 nm after the first injection. By repeating the injection of extra $Zr(OiPr)_4.i$PrOH precursor, we can further increase the nanocrystal size up to 5.1 ± 0.5 nm and 5.4 ± 0.4 nm after the second and third injection respectively. The size dispersion of the main distribution decreases from 9.7% to 7.4% throughout this seeded growth process. However, some

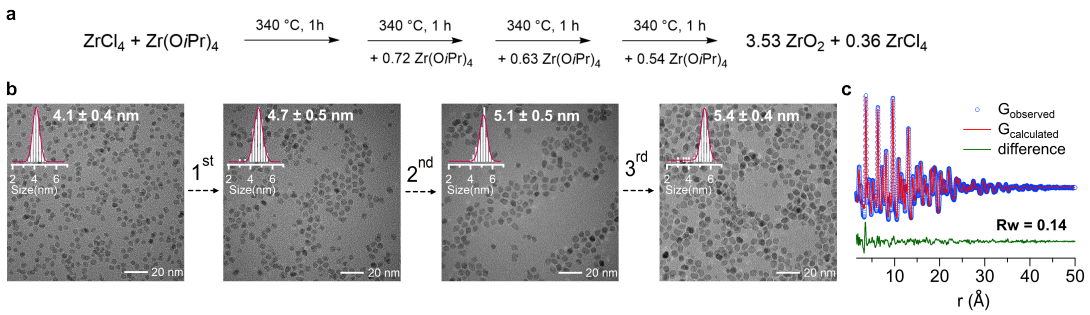

Fig. 2.10 | Size tuning by repeated injection of zirconium isopropoxide isopropanol complex. a Scheme showing the $Zr(OiPr)_4.iPrOH$ injection strategy to increase particle size and yield. **b** TEM and histogram of particles before and after each injection. The average size is indicated. **c** PDF fit for the purified product after three injections with the tetragonal ZrO_2 ($P4_2/nmc$) model. The refined crystallite diameter is 5.33 nm. The other refined values are shown in Supplementary Table A.6. The PDF fit for purified particles before the injection is shown in Supplementary Fig. A.25.

smaller particles (d = 3 - 4 nm) were also observed with TEM, suggesting independent nucleation of new particles and thus not a pure growth process. This is confirmed by considering the yield of the reaction. The overall yield after three injections is determined (by thermogravimetric analysis, Supplementary Fig. A.24) to be 79%, compared to 60% for a regular synthesis. Based on the experimental yield and in the absence of nucleation, one would have expected the particles to have grown to 5.8 nm, instead of the observed 5.4 nm. Therefore, we conclude that nucleation and growth take place simultaneously. There is a difference between the experimental yield and the yield based on the reaction scheme in Fig. 2.10a (91%), which could be due to loss of smaller particles during purification, unreacted monomer at the end of the reaction, or a slight error on the final $ZrCl_4$ amount. Finally, the crystalline phase and size of the final product were verified by X-ray PDF (Fig. 2.10c). The refinement using the tetragonal ZrO_2 structure yields a crystallite size of 5.33 nm, which is very close to the size obtained from TEM, and thus confirms the monocrystalline nature (and epitaxial growth) of the nanocrystals.

2.2.8 The generality of the mechanism

To generalize our findings to other metal oxide nanocrystal systems, HfO_2 and TiO_2 nanocrystals are synthesized in TOPO. Slightly different reaction temperatures are used for HfO_2 (360 °C) and TiO_2 (300 °C) depending on the reports in the literature.[20,21] For HfO_2, the ^{31}P NMR spectra of the reaction aliquots (Supplementary Fig. A.26) confirm the formation of similar active precursors ($HfCl_2(OiPr)_2$) and the co-product $HfCl_4.2TOPO$. The ^{31}P NMR shift of $HfCl_4.2TOPO$ is independently verified by a control experiment (Supplementary Fig. A.27). Furthermore, upon repeated

injection of additional Hf(O*i*Pr)$_4$.*i*PrOH, the nanorods grow in length from 14.7 nm to 24.9 nm (Supplementary Fig. A.28). The overall yield of the synthesis increases from 30% to 63% (see TGA analysis in Supplementary Fig. A.28). For TiO_2, we found neither conclusive evidence for the mixed chloroalkoxide species, nor for a $TiCl_4$ by-product (Supplementary Fig. A.29). We conclude that the formation of HfO_2 follows the same synthetic pathway as for ZrO_2 while the case of TiO_2 requires further research. The differences between TiO_2 on the one hand and ZrO_2 and HfO_2 on the other hand, are most likely responsible for the difficulties in preparing solid solutions of TiO_2 with ZrO_2 or HfO_2.[22] Finally, $ZrBr_4$ is also often used as precursor instead of $ZrCl_4$ and the resulting nanocrystals are smaller (d = 3 nm)[1] It is tempting to assume the reaction follows a similar reaction mechanism as described above. While we also find ligand redistribution effects for a 50/50 mixture of $ZrBr_4$ and Zr(*i*OPr)$_4$.*i*PrOH (with a varying amount of TOPO added), the situation looks more complex and identifying the exact species requires further research (Supplementary Fig. A.30).

2.3 Summary

We elucidated the precursor chemistry in the synthesis of ZrO_2 and HfO_2 nanocrystals from metal chloride and metal isopropoxide in TOPO. We showed how TOPO coordinates to the different precursors and that the mixed chloroalkoxide is the actual precursor in the reaction. Interestingly, we found a ligand redistribution reaction that is controlled by the amount of added neutral Lewis base (L-type). By supplying a sub-stoichiometric amount of Lewis base, the system redistributes the (X-type) ligands to create more Lewis acidic species and thus maximizes the strength of the Lewis acid-base adduct. We also monitored how the reaction mixture decomposes at 340 °C and established the formation of $ZrCl_4$ and isopropanol as by-products. The combination of NMR spectroscopy, DFT calculations at the B3LYP/aug-cc-pVDZ level of theory, and X-ray PDF analysis provided a comprehensive and consistent structural and molecularly refined characterization of precursors and intermediates/by-products. We further quantified the other gaseous by-products by quantitative GC and found that propene is the dominant by-product, with also isopropyl chloride being detected. These results lead us to hypothesize an alternative precursor decomposition mechanism which is based on E1 elimination of propene, ligand redistribution to form MCl_4 and $M(OH)_2(OiPr)_2$, and finally condensation to MO_2 with the formation of isopropanol. Based on the yield we estimate the ratio of the S_N1 and E1 mechanism to be 20 to 80 for ZrO_2. Finally, we used the MCl_4 by-product as an opportunity to control the nanocrystal size. Using a seeded growth approach, we periodically injected metal isopropoxide. The latter forms again the active precursor after reaction with MCl_4, and the nanocrystals grow fur-

ther. We thus introduced a valid pathway to gain control over nanocrystal size, which is particularly challenging for group 4 and 5 metal oxides. In addition, the fundamental insights obtained above will enable the formation of even more complex oxide nanocrystals, which will serve as valuable building blocks in material science.

2.4 Methods

Materials

$ZrCl_4$ (99.9%), $HfCl_4$ (99.9%) and $Ti(OiPr)_4$ (98%) were purchased from Strem Chemicals. $TiCl_4$ (99.9%) was bought from ACROS Organics. $Zr(OiPr)_4.i$PrOH (99.9%), $Hf(OiPr)_4.i$PrOH (99.9%), toluene (99.5%) and, acetone (99.8%) were purchased from Sigma Aldrich and used without further purification. $CDCl_3$ (99.8 atom%) was purchased from Cambridge Isotope laboratories and Benzene-D6 (99.5 atom%) from Apollo scientific, 10/100 mL of activated 4 Å molecular sieves were added and left to stand for 3 days in the glovebox to remove residual water. 3 mm high-throughput NMR tubes (0.58 mm wall thickness) were purchased from Sigma Aldrich. Tri-*n*-octylphosphine oxide (99%) was bought from Strem chemicals and recrystallized according to Owen *et al.*[23] $ZrCl_4$.2THF was synthesized according to Manzer *et al.*[24] General instrumentation. Nuclear Magnetic Resonance (NMR) measurements were recorded at 298 K on Bruker UltraShield 500 spectrometer operating at a frequency of 500.13 MHz. ^{31}P spectra were acquired using inverse gated decoupling, a delay time of 1 second and 64 scans. The ^{31}P spectra were processed with a line broadening of 5 Hz. Spectra acquired with a delay of 5 seconds gave identical relative integrations. Transmission electron microscopy (TEM) images (of a drop-cast suspension on a Holey Carbon Film – Cu grid) were taken on FEI Talos F200C TEM with 200 kV FEG optics.

Nanocrystal synthesis

ZrO_2 nanocrystals are synthesized according to a previously published procedure that involves mixing the reagents at room temperature and heating the mixture up to 340 °C.[2] Typical amounts were: 10 g recrystallized TOPO, $Zr(OiPr)_4.i$PrOH (0.775 g, 2 mmol), and $ZrCl_4$.2THF (0.754 g, 2 mmol). A synthetic variation uses $ZrCl_4$ (0.466 g, 2 mmol) instead of $ZrCl_4$.2THF. For enhancing the reaction yield, $Zr(OiPr)_4.i$PrOH was dissolved in TOPO (6.5 mmol TOPO / 1 mmol Zr), heated to 100 °C and rapidly injected into the reaction mixture at 340 °C. The temperature of the mixture decreases to 320 °C upon injection but rapidly recovers to 340 °C. TiO_2 and HfO_2 nanocrystals were synthesized

using a similar heat-up method with an equimolar mixture of metal chloride and metal isopropoxide but slightly different reaction temperatures were used for HfO_2 (360 °C) and TiO_2 (300 °C). Nanocrystal purification is performed using acetone and toluene as non-solvent and solvent, respectively, in the quantities like previously described.[2] To determine the yield, the dried particles are weighed and their organic fraction is determined by TGA.

Synchrotron X-ray total scattering experiments

Samples were prepared by the temporal sampling of reaction aliquot into 3 mm NMR tubes and sealed under argon atmosphere. We also used 2 mm glass capillaries from Hilgenberg for sampling, but they were prone to breaking and the data quality was worse. Data from the samples were measured at beamline P21.1 at DESY in Hamburg, Germany, and beamline ID15 at ESRF in Grenoble, France. At ESRF, X-ray total scattering data were collected at 80 °C (using a nitrogen cryo stream), in rapid acquisition mode, using a 2D Pilatus CdTe 2M detector (172 × 172 μm pixel size) with a sample-to-detector distance of 264 mm. The incident wavelength of the X-rays was λ = 0.1441 Å (66.05 keV). Calibration of the experimental setup was performed using a silicon standard sample. At DESY, X-ray total scattering data were collected at 80 °C in a home-built aluminium heating block in rapid acquisition mode, using a 2D Varex 4343RF amorphous silicon detector (2880 × 2880 pixels and 150 × 150 μm pixel size) with a sample-to-detector distance of 800 mm. During the measurement, the sample stage was placed in a Helium filled chamber to avoid air scattering. The incident wavelength of the X-rays was λ = 0.1220 Å (101.62 keV). Calibration of setup was performed using a Ni standard.

Analysis of synchrotron X-ray total scattering data

Raw 2D data were corrected for geometrical effects and polarization, then azimuthally integrated to produce 1D scattering intensities versus the magnitude of the momentum transfer Q (where Q = 4π sinθ / λ for elastic scattering) using pyFAI and xpdtools.[25,26] The program xPDFsuite with PDFgetX3 was used to perform the background subtraction, further corrections, and normalization to obtain the reduced total scattering structure function F(Q), and Fourier transformation to obtain the pair distribution function, G(r).[27,28] For data reduction, the following parameters were used after proper background subtraction: Qmin = 0.8 Å^{-1}, Qmax = 16 Å^{-1}, Rpoly = 0.9 Å. Modeling was carried out using Diffpy-CMI.[29]

Lab source X-ray total scattering experiments

Experiments were conducted using a Malvern Panalytical Empyrean Nano Edition lab source PDF diffractometer with Ag-Kα (0.56 Å and 22.1 keV) source. Purified samples were prepared in a 0.2 mm glass capillary. Data collection was carried out with 1D focusing X-ray mirror/slit system and a Galipix3D hybrid pixel detector attached to an 85 mm radius reduction interface using Data collector software. Data reduction was carried out in Highscore Plus with Qmin = 0.4 $Å^{-1}$, Qmax = 20 $Å^{-1}$.[30] Modeling and fitting was carried out using Diffpy-CMI.[29]

GC-FID

Samples (50 µL) of the gas phase were taken from the reaction flask with a gastight syringe and injected into headspace crimp vials (10 mL) filled with nitrogen. The samples were further diluted by transferring 200 µL into a second headspace crimp vial (10 mL). They were analyzed on a gas chromatograph (SRI 8610C, SRI instruments) equipped with a Haysep D column (3 m 2 mm ID Mesh 80/100) and an FID detector. As a carrier gas N_2 was used with a flow rate of 1 mL/min. The samples (1 mL) were injected with an autosampler (HT2000H, HTA instruments). The separation of the products was achieved with a temperate gradient starting from 70 °C (held for 2 min) and then heating to 270 °C at a rate of 10 °C/min. As a reference isopropyl chloride (99%, Sigma Aldrich) and propene (Pangas) was used.

Quantum chemical calculations

All calculations were performed with the B3LYP functional together with the aug-cc-pVDZ basis set for C, H, O, Cl, and P atoms using Gaussian09.[31–34] The aug-cc-pVDZ pseudopotential and associated basis set of Peterson *et al.* was taken from the Basis Set Exchange and applied to the Zr atoms.[35,36] To validate the calculations at the B3LYP/aug-cc-pVDZ level of theory which yielded ΔH = –20.7 kJ/mol for the exchange reaction of a single THF molecule in $ZrCl_4$.2THF for triethylphosphine oxide (only *cis* isomers considered), the enthalpies were recomputed at the M06/aug-cc-pVDZ and MP2/aug-cc-pVDZ levels of theory for which ΔH = –16.1 kJ/mol and ΔH = –20.4 kJ/mol were obtained, respectively. Thus, the formation energies are all within 4 kJ/mol (∼1 kcal/mol) which is the "chemical accuracy" expected from such calculations. As the species under investigation are already computationally demanding as per their size, calculations with several explicit solvent molecules in their optimized structures are too time consuming. Alternatively, using implicit solvent models as a substitute was deemed not sufficiently accurate given that some of the

energy differences encountered are small. Therefore, only calculations in the gas phase were carried out. To calculate the ^{1}H and ^{31}P NMR chemical shifts from the optimized structures, we followed the protocol of Willoughby *et al.*[37] The scaling factor for the ^{1}H NMR chemical shifts at our level of theory was reported by Pierens.[38]

Thermogravimetric analysis

Experiments were performed on a TGA5500 (TA instruments). Sample was heated to 800 °C at a rate of 5 °C/min. After maintaining the temperature for 15 min, the sample was cooled down to room temperature.

Contributions

Quantum chemical calculations were performed by Mr. Dietger Van den Eynden and GC-FID experiments were performed by Ms. Valérie Waser. Dr. Susan Rudd Cooper and Dr. Jette Katja Mathiesen helped with the PDF analysis.

Bibliography

[1] J. Joo, T. Yu, Y. W. Kim, H. M. Park, F. Wu, J. Z. Zhang, and T. Hyeon. Multigram scale synthesis and characterization of monodisperse tetragonal zirconia nanocrystals. *Journal of the American Chemical Society*, 125(21):6553–6557, 2003.

[2] K. De Keukeleere, S. Coucke, E. De Canck, P. Van Der Voort, F. Delpech, Y. Coppel, Z. Hens, I. Van Driessche, J. S. Owen, and J. De Roo. Stabilization of colloidal Ti, Zr, and Hf oxide nanocrystals by protonated tri-n-octylphosphine oxide (TOPO) and its decomposition products. *Chemistry of Materials*, 29(23):10233–10242, 2017.

[3] M. P. Hendricks, M. P. Campos, G. T. Cleveland, I. Jen-La Plante, and J. S. Owen. A tunable library of substituted thiourea precursors to metal sulfide nanocrystals. *Science*, 348:1226–1230, 2015.

[4] S. Shaw, B. Yuan, X. Tian, K. J. Miller, B. M. Cote, J. L. Colaux, A. Migliori, M. G. Panthani, and L. Cademartiri. Building materials from colloidal nanocrystal arrays: Preventing crack formation

during ligand removal by controlling structure and solvation. *Advanced Materials*, 28(40):8892–8899, 2016.

[5] V. M. S. Gil and N. C. Oliveira. On the use of the method of continuous variations. *Journal of Chemical Education*, 67:473, 1990.

[6] A. Zheng, S.-J. Huang, S.-B. Liu, and F. Deng. Acid properties of solid acid catalysts characterized by solid-state ^{31}P NMR of adsorbed phosphorous probe molecules. *Physical Chemistry Chemical Physics*, 13:14889–14901, 2011.

[7] Q. Zhao, W.-H. Chen, S.-J. Huang, Y.-C. Wu, H.-K. Lee, and S.-B. Liu. Discernment and quantification of internal and external acid sites on zeolites. *The Journal of Physical Chemistry B*, 106:4462–4469, 2002.

[8] W. H. Chen, H. H. Ko, A. Sakthivel, S. J. Huang, S. H. Liu, and A. Y. Lo. A solid-state NMR, FT-IR and TPD study on acid properties of sulfated and metal-promoted zirconia: Influence of promoter and sulfation treatment. *Catalysis Today*, 116:111–120, 2006.

[9] C. Laurence and J.-F. Gal. Lewis basicity and affinity scales. *Wiley*, 2009.

[10] M. Eberle and C. Röhr. Tetrachlorobis(tetrahydrofuran-O)zirconium(IV). *Acta Crystallographica Section C*, 52:566–568, 1996.

[11] N. C. Anderson, P. E. Chen, A. K. Buckley, J. De Roo, and J. S. Owen. Stereoelectronic effects on the binding of neutral lewis bases to CdSe nanocrystals. *Journal of the American Chemical Society*, 140(23):7199–7205, 2018.

[12] D. C. Bradley, R. C. M., J. D. Swanwick, and W. Wardlaw. Structural chemistry of the alkoxides. Part IV. Normal alkoxides of silicon, titanium, and zirconium. *Journal of Chemical Society*, pages 2025–2030, 1953.

[13] G. R. Fulmer, A. J. M. Miller, N. H. Sherden, H. E. Gottlieb, A. Nudelman, B. M. Stoltz, J. E. Bercaw, and K. I. Goldberg. NMR chemical shifts of trace impurities: Common laboratory solvents, organics, and gases in deuterated solvents relevant to the organometallic chemist. *Organometallics*, 29, 2010.

[14] S. Shaw, J. L. Colaux, J. L. Hay, F. C. Peiris, and L. Cademartiri. Building materials from col-

loidal nanocrystal arrays: Evolution of structure, composition, and mechanical properties upon the removal of ligands by O_2 plasma. *Advanced Materials*, 28(40):8900–8905, 2016.

[15] C. Suchomski, D. J. Weber, P. Dolcet, A. Hofmann, P. Voepel, J. Yue, M. Einert, M. Möller, S. Werner, S. Gross, I. Djerdj, T. Brezesinski, and B. M. Smarsly. Sustainable and surfactant-free high-throughput synthesis of highly dispersible zirconia nanocrystals. *Journal of Materials Chemistry A*, 5(31):16296–16306, 2017.

[16] H. Weingarten and J. R. Van Wazer. Exchange of parts between molecules at equilibrium. VI. scrambling on titanium of the alkoxyl, dimethylamino, and halogen substituents. *Journal of the American Chemical Society*, 87(4):724–730, 1965.

[17] R. C. Mehrotra. Synthesis and properties of alkoxy and acyloxysilanes. *Pure Applied Chemistry*, 13(1-2):111–132, 1966.

[18] D. C. Bradley, D. C. Hancock, and W. Wardlaw. 524. titanium chloride alkoxides. *Journal of Chemical Society*, pages 2773–2778, 1952.

[19] D. C. Bradley, R. C. Mehrotra, I. P. Rothwell, and A. Singh. *Alkoxo and Aryloxo Derivatives of Metals*. 2001.

[20] T. J. Trentler, T. E. Denler, J. F. Bertone, A. Agrawal, and V. L. Colvin. Synthesis of TiO_2 nanocrystals by nonhydrolytic solution-based reactions. *Journal of the American Chemical Society*, 121(7):1613–1614, 1999.

[21] E. Tirosh and G. Markovich. Control of defects and magnetic properties in colloidal HfO_2 nanorods. *Advanced Materials*, 19(18):2608–2612, 2007.

[22] J. Tang, J. Fabbri, R. D. Robinson, Y. Zhu, I. P. Herman, M. L. Steigerwald, and L. E. Brus. Solid-solution nanoparticles: Use of a nonhydrolytic sol-gel synthesis to prepare HfO_2 and $Hf_xZr_{1-x}O_2$ nanocrystals. *Chemistry of Materials*, 16(7):1336–1342, 2004.

[23] J. S. Owen, J. Park, P. E. Trudeau, and A. P. Alivisatos. Reaction chemistry and ligand exchange at cadmium-selenide nanocrystal surfaces. *Journal of the American Chemical Society*, 130(37):12279–12280, 2008.

[24] L. E. Manzer, Joe Deaton, Paul Sharp, and R. R. Schrock. *31. Tetrahydrofuran Complexes of*

Selected Early Transition Metals, pages 135–140. John Wiley 'I&' Sons, Inc., 2007.

[25] Giannis Ashiotis, Aurore Deschildre, Zubair Nawaz, Jonathan P. Wright, Dimitrios Karkoulis, Frédéric Emmanuel Picca, and Jérôme Kieffer. The fast azimuthal integration python library:pyFAI. *Journal of Applied Crystallography*, 48(2):510–519, 2015.

[26] C. J. Wright and X. D. Zhou. Computer-assisted area detector masking. *Journal of Synchrotron Radiation*, 24(2):506–508, 2017.

[27] P. Juhás, T. Davis, C. L. Farrow, and S. J. L. Billinge. PDFgetX3: a rapid and highly automatable program for processing powder diffraction data into total scattering pair distribution functions. *Journal of Applied Crystallography*, 46:560–566, 2013.

[28] X. Yang, P. Juhás, C. L. Farrow, and S. J. L. Billinge. xPDFsuite: an end-to-end software solution for high throughput pair distribution function transformation, visualization and analysis. *arXiv preprint arXiv:1402.3163*, 2014.

[29] P. Juhás, C. L. Farrow, X. Yang, K. R. Knox, and S. J. L. Billinge. Complex modeling: a strategy and software program for combining multiple information sources to solve ill posed structure and nanostructure inverse problems. *Acta Crystallographica*, 71:562–568, 2015.

[30] T. Degen, M. Sadki, E. Bron, U. König, and G Nénert. The highscore suite. *Powder Diffraction*, 29:S13–S18, 2014.

[31] M. J. Frisch, G. W. Trucks, H. B. Schlegel, G. E. Scuseria, M. A. Robb, J. R. Cheeseman, G. Scalmani, V. Barone, B. Mennucci, G. A. Petersson, H. Nakatsuji, M. Caricato, X. Li, H. P. Hratchian, A. F. Izmaylov, J. Bloino, G. Zheng, J. L. Sonnenberg, M. Hada, M. Ehara, K. Toyota, R. Fukuda, J. Hasegawa, M. Ishida, T. Nakajima, Y. Honda, O. Kitao, H. Nakai, T. Vreven, J. A. Montgomery, Jr., J. E. Peralta, F. Ogliaro, M. Bearpark, J. J. Heyd, E. Brothers, K. N. Kudin, V. N. Staroverov, R. Kobayashi, J. Normand, K. Raghavachari, A. Rendell, J. C. Burant, S. S. Iyengar, J. Tomasi, M. Cossi, N. Rega, J. M. Millam, M. Klene, J. E. Knox, J. B. Cross, V. Bakken, C. Adamo, J. Jaramillo, R. Gomperts, R. E. Stratmann, O. Yazyev, A. J. Austin, R. Cammi, C. Pomelli, J. W. Ochterski, R. L. Martin, K. Morokuma, V. G. Zakrzewski, G. A. Voth, P. Salvador, J. J. Dannenberg, S. Dapprich, A. D. Daniels, Ö. Farkas, J. B. Foresman, J. V. Ortiz, J. Cioslowski, and D. J. Fox. Gaussian 09, Revision B. 01. Gaussian, Inc., Wallingford. 2009.

[32] R. A. Kendall, T. H. Dunning, and R. J. Harrison. Electron affinities of the first-row atoms revisited. Systematic basis sets and wave functions. *The Journal of Chemical Physics*, 96(9):6796–6806, 1992.

[33] A. D. Becke. Density-functional exchange-energy approximation with correct asymptotic behavior. *Physical Review A*, 38(6):3098–3100, 1988.

[34] C. Lee, W. Yang, and R. G. Parr. Development of the Colle-Salvetti correlation-energy formula into a functional of the electron density. *Physical Review B*, 37(2):785–789, 1988.

[35] K. A. Peterson, D. Figgen, M. Dolg, and H. Stoll. Energy-consistent relativistic pseudopotentials and correlation consistent basis sets for the 4d elements Y–Pd. *The Journal of Chemical Physics*, 126(12):124101, 2007.

[36] B. P. Pritchard, D. Altarawy, B. Didier, T. D. Gibson, and T. L. Windus. New basis set exchange: An open, up-to-date resource for the molecular sciences community. *Journal of Chemical Information and Modeling*, 59(11):4814–4820, 2019.

[37] P. H. Willoughby, M. J. Jansma, and T. R. Hoye. A guide to small-molecule structure assignment through computation of (^{1}H and ^{13}C) NMR chemical shifts. *Nature Protocols*, 9(9):643–660, 2014.

[38] G. K. Pierens. ^{1}H and ^{13}C NMR scaling factors for the calculation of chemical shifts in commonly used solvents using density functional theory. *Journal of Computational Chemistry*, 35(18):1388–1394, 2014.

"You'll never find rainbows if you're looking down"

- Charlie Chaplin

Chapter 3

Insight into the nucleation and growth mechanism†

3.1 Introduction

In the previous chapter we conclude that a mixed chloroalkoxide precursor species is formed, which undergoes (predominantly) E1 elimination to zirconium hydroxide and propene, see Fig. 2.9.[1] After ligand redistribution and condensation, $ZrCl_4$, zirconium oxide, and isopropanol are formed as products. The $ZrCl_4$ co-product is retrieved as a complex of TOPO,[1] and also the nanocrystals are covered with TOPO and some of its decomposition products.[2] There is no information about their nucleation and growth mechanism. Understanding these processes might help to further control the nanocrystal size, introduce dopants and access the core-shell structures of group 4 oxides. Since also TiO_2 and HfO_2 nanocrystals can be synthesized by similar routes, the ZrO_2 model system is relevant for the entire group 4. Within this context of group 4 oxides, a Lewis structure of a MO_2 "monomer" is hard to conceive. A slightly more realistic monomer could be, e.g., $Zr(OH)_4$, but group 4 metal hydroxide species are highly reactive and usually already condense before the tetrahydroxide species can be fully formed.

In this chapter, we investigate the crystallization mechanism of ZrO_2 nanocrystals in TOPO, synthesized from zirconium halide (chloride or bromide) and zirconium isopropoxide. We combine X-

†This chapter is adapted from: An Amorphous Phase Precedes Crystallization: Unraveling the Colloidal Synthesis of Zirconium Oxide Nanocrystals. Rohan Pokratath, Laurent Lermusiaux, Stefano Checchia, Jikson Pulparayil Mathew, Susan Rudd Cooper, Jette Katja Mathiesen, Guillaume Landaburu, Soham Banerjee, Songsheng Tao, Nico Reichholf, Simon J. L. Billinge, Benjamin Abecassis, Kirsten M. O. Jensen, and Jonathan De Roo*, ACS Nano, 17, 9, 8796-8806, 2023, DOI: 10.1021/acsnano.3c02149.

ray pair distribution function analysis, small angle X-ray scattering, nuclear magnetic resonance, and transmission electron microscopy to investigate their nucleation and growth. In order to assign the crystallization mechanism to one of the earlier prposed mechanisms, we determined the temporal evolution of the number of particles, the particle size and the yield. We find that after an initial fast increase in the number of particles, the particle number drops again with a concomitant reduction of the size dispersion. While the first particles are amorphous, the final particles are monocrystalline.

3.2 Results and Discussion

We synthesize ZrO_2 nanocrystals at 340 °C, from a 1:1 molar mixture of $Zr(OiPr)_4 \cdot iPrOH$ and either $ZrCl_4$ or $ZrBr_4$. The synthesis is performed in pure tri-octylphosphine oxide (TOPO), which acts as both ligand and solvent. Details of the precursor chemistry are shown in Fig. 2.9.

3.2.1 Small angle X-ray scattering analysis

Given the success of small angle X-ray scattering (SAXS) in delivering insights into nucleation and growth mechanisms,[3–6] we also take it here as a starting point in our investigation. We performed *ex situ* SAXS measurements on aliquots, taken from the reaction mixture at 300 °C, 320 °C, and 340 °C during the heating ramp, and at different time intervals at 340 °C. The samples were measured in a flow-through setup to obtain signals in absolute intensity (Fig. 3.1a-b), and to estimate the particle concentration and size (see Methods section and Supplementary information for details).[7] Qualitatively, the evolution of the scattering curves suggests the formation of spherical particles for both reactions (with either $ZrCl_4$ or $ZrBr_4$). With increasing reaction time, the signal increasingly resembles the form factor of a sphere; with a plateau at intermediate q and an abrupt decrease followed by oscillations for q larger than 2 nm^{-1}. Both the increasing intensity of the plateau and the shift of the position of the abrupt decrease towards smaller q, indicate particles growing in size. The increasing amplitude of the oscillations suggests that the polydispersity decreases with time.

The particle size and concentration were quantified by fitting the normalized scattering curves. At lower q, we observe an increase in the intensity (Fig. 3.1a-b), which probably results from a partial aggregation of the particles. This would require introducing a structure factor in the fit. To minimize this effect and to consider a model of independent scatterers, our experimental data is fitted in the q region larger than 0.5 nm^{-1}. The SAXS patterns contain contributions from precursors and

ZrO_2 particles in solution:

$$I \approx I_{particles} + I_{precursors}$$

To approximate the signal of the precursors, we use the experimental SAXS signal of the $ZrCl_4$ reaction mixture, aliquoted at 300 °C. At this temperature, precursor conversion has not yet started.[1] Therefore, our fitting function becomes the sum of the scattering cross section of a distribution of polydisperse spheres and the experimental precursor signal, multiplied by a fitting parameter (F) set between 0 and 1:

$$I_{fit} = I^{theor}_{spheres} + F \times I^{exp}_{precursors}$$

This approach leads to very good fits for all the SAXS patterns (Fig. 3.1c-d), allowing us to derive the particle radius, polydispersity, and concentration during the synthesis, for both systems (Fig. 3.1e-g).

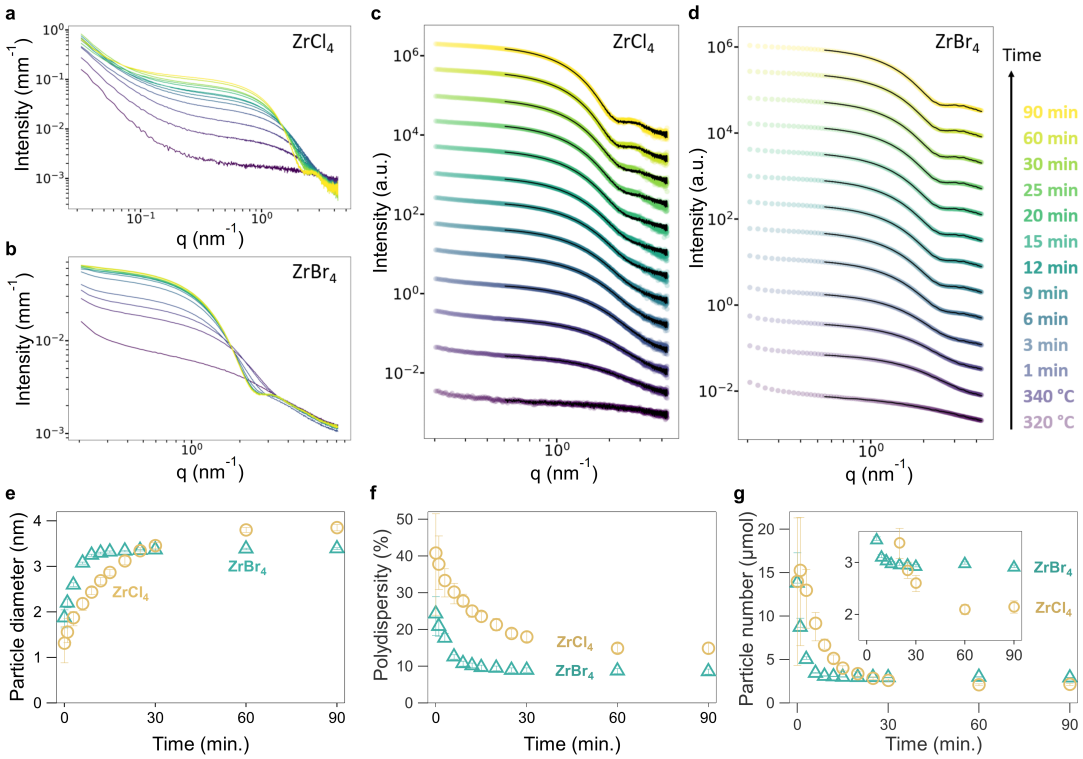

Fig. 3.1 | **SAXS analysis on reaction aliquots.** Normalized SAXS pattern **a-b** and corresponding fits **c-d** for reaction mixtures with either $ZrCl_4$ or $ZrBr_4$ as halide source. The different patterns are shifted with respect to one another for better visualization. Time evolution at 340 °C for the **e** particle diameter, **f** polydispersity, and **g** particle concentration obtained after fitting the experimental data.

For both reactions (with either $ZrCl_4$ or $ZrBr_4$ as halide source), there are a lot of particles present in the solution once the reaction temperature reaches 340 °C. We observe particle growth

(increase in diameter) with a simultaneous reduction in the polydispersity (Fig. 3.1e-f). The higher polydispersity in the first 10 min is also responsible for the higher error in the diameter value. The final particle size obtained in the $ZrCl_4$ reaction (3.9 nm) is higher than for the $ZrBr_4$ reaction (3.4 nm), consistent with previous reports.[8] The particles in the chloride reaction mixture keep growing for 90 min, while the growth of the bromide particles stops after about 15 min. Interestingly, the particle number decreases over the course of the reaction. These results stand in stark contrast to many other surfactant-assisted nanocrystal syntheses, which featured a continuous increase of the particle concentration (continuous nucleation).[3–5,9,10] Our data thus rather suggests a coalescence or ripening mechanism.[11–13] A lot of particles nucleate at the start and grow at the expense of other particles. When comparing the two halide sources, the particles from the bromide reaction grow faster, have a lower dispersity, are smaller in size and their final concentration is higher. For the same material yield, one can have either a few, large particles or many, small particles. The particle concentration at the end of the bromide reaction is indeed about 50% higher than in the chloride reaction (Fig. 3.1g), consistent with their diameter difference.

3.2.2 X-ray pair distribution function analysis

X-ray total scattering and pair distribution function analysis are great tools for understanding the chemistry of nucleation.[14] At room temperature, the PDF of the chloride reaction mixture features three inter-atomic distances; Zr-O (2.0 Å), Zr-Cl (2.5 Å) and Zr-P (3.5 Å), as expected for the $ZrCl_2(O\mathit{i}Pr)_2 \cdot 2\,TOPO$ precursor species. These atom pairs can still be recognized in the PDF of the first aliquot taken at 340 °C, see Fig. 3.2a (0 min). We observe similar atomic pair distances for the reaction mixture with $ZrBr_4$, where the Zr-Br distance is observed at 2.7 Å (Fig. 3.2b).

Within minutes after reaching 340 °C, ZrO_2 crystals start to form and grow in size, indicated by the appearance of correlations at higher distances (Fig. 3.2a-b). The Zr-Cl and Zr-Br distances contract slightly but remain present until the end of the reaction and are assigned to the TOPO complexes of $ZrCl_4$ and $ZrBr_4$. For the chloride reaction, this complex is $ZrCl_4 \cdot 2\,TOPO$. For the bromide reaction, the exact nature of the complex is unclear since the complexation between $ZrBr_4$ and TOPO is not fully understood (Supplementary Fig. B.3). Nevertheless, the ^{31}P NMR spectrum at the end of the reaction, is almost identical to the spectrum of $ZrBr_4$ and 8 TOPO equivalents. Therefore, we conclude that the metal halide is formed as the by-product, in both cases. We infer that the reaction with $ZrBr_4$ likely follows a similar precursor conversion mechanism as the reaction with $ZrCl_4$ (Fig. 2.9). Previously, we have shown that the PDF of the last aliquot (end of reaction)

can be well described by a two-phase model, featuring (i) tetragonal ($P4_2/nmc$) ZrO_2 and (ii) the $ZrCl_4 \cdot 2\,TOPO$ complex.[1] This approach does not work as well for the bromide case, since we do not have an accurate structure for the TOPO complex of $ZrBr_4$. The two-phase modeling strategy also appears challenging for the early aliquots in the chloride reaction. The contribution of the crystal phase is low and the molecular zirconium precursors species are not yet fully converted to the $ZrCl_4 \cdot 2\,TOPO$ by-product.

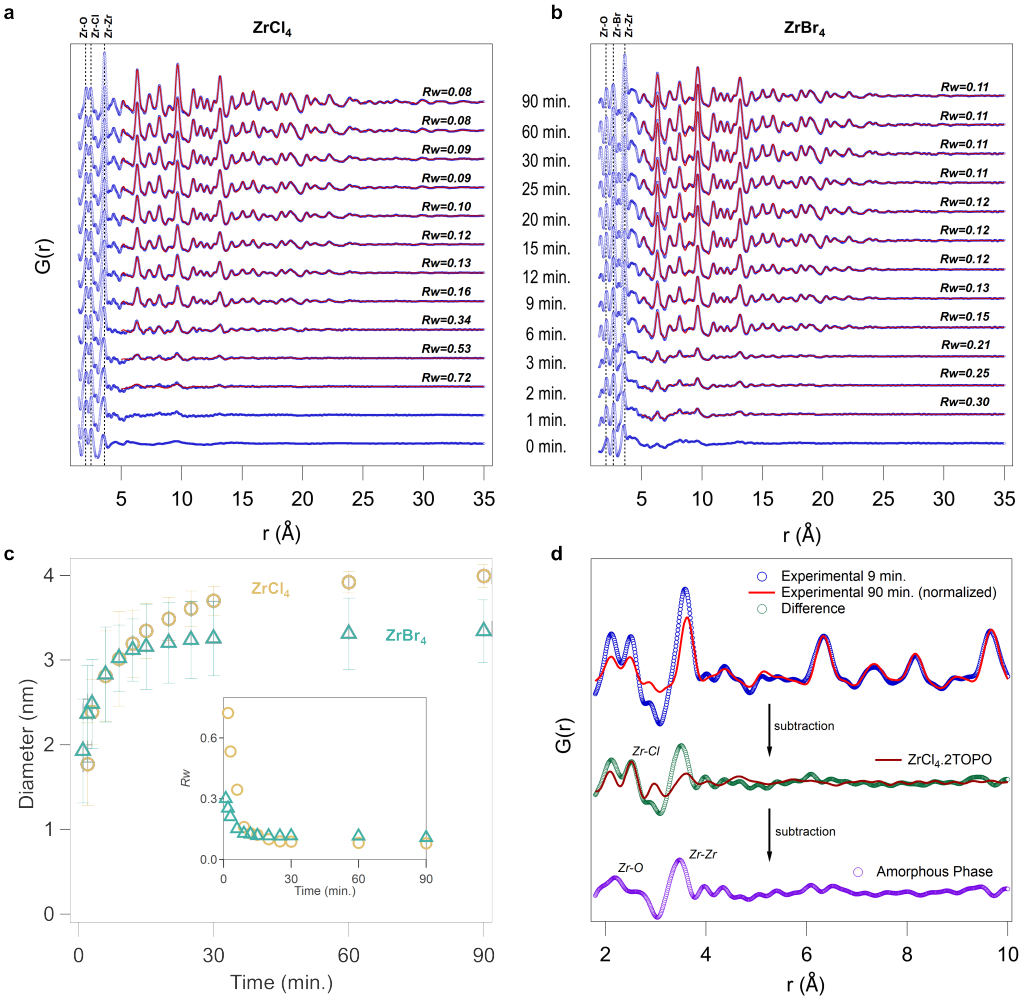

Fig. 3.2 | **Ex situ PDF analysis on reaction aliquots.** The experimental (blue circles) and calculated (red line) PDF for the reaction aliquots with either **a** $ZrCl_4$ or **b** $ZrBr_4$ as halide source. The goodness of fit is indicated by *Rw*. The reaction temperature of 340 °C is reached at t = 0 min. **c** The refined nanocrystal size by PDF and corresponding *Rw* values (inset) of the reaction aliquots. The data points that could not be refined are represented by a diameter of 0 nm. The refined parameters are shown in Supplementary Table B.1-B.2. **d** Extraction of PDF pattern of the amorphous intermediate phase for the 9 min. aliquot ($ZrCl_4$ reaction). The blue circles represent the measured PDF of the aliquot, and the red line corresponds to the normalized PDF of the reaction crude product (90 min. aliquot). After subtraction of the two, the data in the green circles is obtained. The experimental PDF of the $ZrCl_4 \cdot 2\,TOPO$ by-product (brown line) is scaled and subtracted from the green data, obtaining the PDF of the amorphous intermediate (violet circles).

To quantify the crystal size, we thus start the fit from 5 Å, cutting off the contributions from the molecular precursors and only focusing on the tetragonal ZrO_2 phase, see Fig. 3.2a-b. For the bromide case, we follow the same strategy but we add a decaying sinusoid to the model. The latter takes care of a periodic oscillation in the data. This effect may originate from the presence of organic ligands in the material.[15] Sinusoidal oscillations can also appear in differential PDF measurements due to solvent restructuring.[16] The refined particle size and goodness of fit (*Rw*) are shown in Fig. 3.2c. In the chloride reaction mixture, we could not obtain a decent refinement for the aliquots taken at 0 and 1 min (although one can argue that very weak signals are present after 1 min). Only after 2 min, we can refine a nanocrystal structure with a diameter of 1.8 nm. The crystal pattern is still fairly weak (due to a low concentration of crystals), which is reflected in the poor (high) *Rw* of the refinement. The particles grow over time to the expected crystal diameter of about 4 nm, and the *Rw* of the refinements decreases to 8%. The PDF of the bromide reaction mixture could not be refined at t = 0 min, even though some very weak signals are observed. After 1 min, we are able to refine the PDF reasonably well ($Rw = 0.3$) and the first observable nanocrystal is also 1.9 nm in diameter. The bromide reaction forms crystalline material faster than the chloride reaction, but the particles are growing only to about 3.3 nm in size. The bromide nanocrystals reach their final size after about 30 min, while the chloride particles keep growing for up to 90 min. This is even more obvious when the nanocrystal volume is plotted over time (Supplementary Fig. B.4). The obtained crystal size from PDF at various time points is in agreement with the size calculated from the TEM images of purified nanocrystals (Supplementary Fig. B.5), indicating that the particles are monocrystalline.

We also followed the reaction *in situ* in a 3 mm NMR tube heated by an aluminum metal block with heating cartridges (see experimental and Supplementary Fig. B.6). Similar trends are observed (see Supplementary Fig. B.7) but in general, the signal-to-noise ratio is much lower compared to the *ex situ* experiments. Most importantly, we conclude that no phase transformation took place in the crystals upon quenching the reaction aliquots to room temperature.

3.2.3 The emergence of an amorphous phase

Upon reaching 340 °C (t = 0 min), SAXS reveals the presence of nanoparticles, while PDF demonstrates the absence of nanocrystals (no long range correlations). Since SAXS detects any nanoparticle, crystalline or amorphous, we hypothesize that the first particles observed by SAXS are amorphous (*i.e.*, disordered). To investigate this hypothesis further, we turn now to the short-range PDF data (1.5 – 5 Å). This complex region contains contributions from precursors, by-products, crystalline (or-

dered) particles, and amorphous (disordered) particles. We first analyze the chloride reaction aliquot at t = 9 min (Fig. 3.2d). We know that after 9 min there is no precursor left and the only molecular zirconium species is the by-product; $ZrCl_4 \cdot 2\,TOPO$ (Supplementary Fig. B.8).[1] The absence of precursors simplifies the PDF analysis. To extract the contribution of the amorphous particles, we proceed as follows.

We scale the PDF of the final aliquot (90 min) to match the intensity of the peaks beyond 5 Å (Fig. 3.2d). As expected, a significant deviation is observed in the short r-range (1.5 - 5 Å). We then subtract the two PDFs and obtain the green data. This procedure removes the entire crystalline fraction and part of the $ZrCl_4 \cdot 2\,TOPO$ by-product. The latter is only partially removed due to the difference in the relative concentration of crystals and by-product at the two time points. Therefore, we scale the experimental PDF of $ZrCl_4 \cdot 2\,TOPO$ to the Zr-Cl peak in the green data and subsequently subtract it. We thus arrive at the residual PDF, free of crystals and by-product. Since also precursor is absent (evidenced by NMR), the residual PDF belongs to an amorphous intermediate. We exclude the possibility of a monomer due to the pronounced Zr-Zr distance in the PDF. No long-range order is present in the PDF of the amorphous phase. The amorphous PDF signal, together with the SAXS results firmly establish the existence of amorphous particles as reaction intermediates. By extending the analysis to other aliquots (Supplementary Fig. B.9), we verified that with time, the crystalline phase captures a higher proportion of the short-range structure, confirming that the amorphous phase is an intermediate that disappears over the course of the reaction.

To rule out the possibility of amorphization while sampling/cooling down, similar analyses were carried out on the *in situ* data set and similar results are obtained (Supplementary Fig. B.10).

3.2.4 The mass balance of the reaction

To gain further insight into the reaction mechanism and to connect the crystallization process to the precursor decomposition process, we sought to quantify all zirconium species in the reaction and have a closed mass balance. Subsequently, we aimed at determining the rate of each step. In the case of semiconductor nanocrystals, the precursor-to-monomer (P to M) conversion kinetics is assumed slower than the crystallization kinetics, see Equation 3.1.[17,18] A rate-limiting precursor conversion is a postulated prerequisite for controlling the size by the reaction rate.[19,20]

$$P \xrightarrow{slow} M \underset{}{\overset{fast}{\rightleftharpoons}} NC \tag{3.1}$$

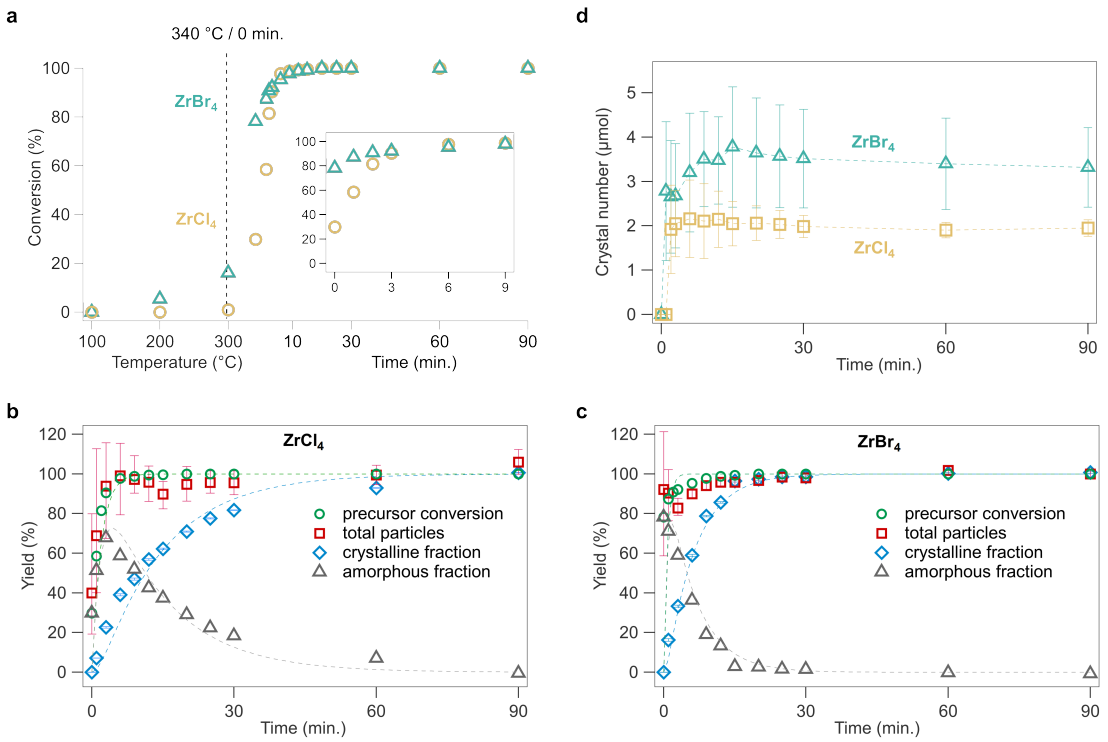

Fig. 3.3 | The precursor conversion, crystal number, and mass balance during the course of the reaction. a The disappearance of zirconium isopropoxide units determined with ^{1}H NMR. The inset aims at showing more detail for the first 9 min at 340 °C. The corresponding ^{1}H spectra are shown in Supplementary Fig. B.11-B.12. The yield of the reaction, from the perspective of precursor conversion, the total particles formed (from SAXS analysis), the crystalline fraction (from reciprocal total scattering analysis), and the amorphous fraction (total particles minus crystalline fraction) for reaction mixtures with either **b** $ZrCl_4$ or **c** $ZrBr_4$ as halide source. The dotted lines indicate the fit obtained using the simple two-step mechanism (3.2). **d** The number of nanocrystals as a function of time, calculated from the crystalline yield and the crystal size (PDF).

To quantify the precursor conversion in our system, we followed the disappearance of the isopropoxide resonance in ^{1}H NMR, see Fig. 3.3a (Corresponding ^{1}H spectra are shown in Supplementary Fig. B.11-B.12). We observe faster conversion with $ZrBr_4$, compared to $ZrCl_4$. Even during the heating phase to 340 °C, the bromide reaction mixture starts to convert at 200 °C, while the chloride reaction only starts converting between 300 and 340 °C. Consequently, at t = 0 min (at 340 °C), the bromide reaction progress is already about 80%. Interestingly, the bromide reaction slows down considerably by the end of the precursor conversion. For both precursors, full conversion is achieved after 9 min at 340 °C.

In Fig. 3.3b-c, we plot the yield of precursor conversion together with the yield of crystalline particles, amorphous particles and total particles (crystalline and amorphous). We calculated the total particle yield from the SAXS data using the particle size, the size distribution and the particle

concentration assuming the bulk density of ZrO_2. For the end of the reaction, we obtain a yield (n_{ZrO_2}/n_{Zr}) of 63% with $ZrCl_4$ and 58% with $ZrBr_4$, consistent with the obtained yield after isolation and purification (determined gravimetrically). We know that the zirconium halide by-product is responsible for the lower than 100% yield (based on metal). Therefore, the unbiased results from SAXS satisfy the mass balance of zirconium according to Fig. 2.9. To focus on the oxide formation, we re-scaled the yield from SAXS to 100% at the end of the reaction, which also corresponds to 100% precursor conversion. The rate of precursor conversion is equal to the rate of particle formation since the precursor conversion data and the total particle (SAXS) data coincide, within error. This means that, at any time, all the zirconium atoms are either in the form of precursor or part of a particle (amorphous or crystalline). We do not find evidence for another species such as molecular solute or a "monomer".

We calculated the yield of crystalline particles from the total scattering data, by integrating the area under a selected Bragg peak (Supplementary Fig. B.13) after background subtraction. Also here, we scale the yield to 100% at the end of the reaction. This assumes that no amorphous phase is present at the end of the reaction. It is a fair approximation given that the PDF of the last reaction aliquot could be accurately modeled by only the crystalline phase and the $ZrCl_4$ by-product.[1] We then calculate the amorphous fraction of particles by subtracting the crystalline fraction from the total particle yield. Given our conclusion that precursor conversion and total particle yield are identical, we used here the precursor conversion yield for the subtraction, since there is less scatter on this data. Finally, with crystal yield and nanocrystal size in hand, we could also calculate the concentration of nanocrystals over the course of the reaction (Fig. 3.3d).

Focusing first on the chloride reaction in Fig. 3.2c, one observes that the precursor conversion is complete at 9 min, but the crystalline yield is only about 50%. In addition, there is no evidence for a monomer. Hence this reaction is not well described by Equation (3.1). Instead, precursor conversion is clearly faster than crystallization. Since the species formed by precursor conversion (metal hydroxide) is highly reactive, this leads to a build-up of amorphous intermediate (I). The intermediate then slowly recrystallizes into nanocrystals, see Equation (3.2). Similar conclusions are reached for the bromide reaction although the crystallization rate appears faster, Fig. 3.3c.

$$\mathrm{P} \xrightarrow[k_1]{fast} \mathrm{I} \xrightarrow[k_2]{slow} \mathrm{NC} \tag{3.2}$$

To obtain more quantitative insight into the reaction kinetics, we modeled the time-dependent con-

centration of species. Starting from the simplest model containing two elementary steps (Mechanism (3.2)), we can reasonably well describe the kinetics of both the chloride and the bromide reaction. The resulting fit is plotted onto Fig. 3.3b-c as dotted lines (and also plotted in Supplementary Fig. B.14 and B.20). The rate constants are provided in Table 3.1. The bromide crystallization rate constant (k_2) is about double compared to the chloride crystallization rate constant. In both cases, the precursor conversion rate constant is about one order of magnitude higher than the crystallization rate constant.

Table 3.1 | Comparison of rate constants for various mechanisms. Comparison of reaction rate constants obtained after fitting various mechanisms for reaction mixtures with either **a** $ZrCl_4$ or **b** $ZrBr_4$ as halide source. The unit of rate constants are: s^{-1} - first order, $M^{-1}\ s^{-1}$ - second order.

Mechanism	Precursor	k_1	k_2	k_3
(3)	$ZrCl_4$	$8.8 \pm 0.2\ 10^{-3}$	$1.2 \pm 0.1\ 10^{-3}$	-
(3)	$ZrBr_4$	$2.3 \pm 0.1\ 10^{-2}$	$2.8 \pm 0.1\ 10^{-3}$	-
(4)	$ZrCl_4$	$8.8 \pm 0.2\ 10^{-3}$	4.7 ± 0.2	1.0 ± 0.3
(5)	$ZrBr_4$	123 ± 2	4.7 ± 0.4	17 ± 1

Focusing further on the chloride reaction, we tested multiple other mechanisms to explore the possibility of second order reactions, equilibria and auto-catalytic mechanisms (Supplementary Fig. B.15-B.19). Taking the precursor conversion as second order, we obtain a considerably worse fit (Supplementary Fig. B.15). This gives us further confidence in the E1 elimination mechanism since the latter should be first order. A mechanism that includes an equilibrium between precursors and intermediates does not fit significantly better than Mechanism (3.2) (Supplementary Fig. B.17). The back reaction ($I \longrightarrow P$) has an almost negligible rate constant. The fit improved when taking the crystallization step as second order (Supplementary Fig. B.16). Finally, the best agreement was obtained with Mechanism (3.3) (Supplementary Fig. B.19).

$$\begin{aligned} P &\xrightarrow{k_1} I \\ 2\,I &\xrightarrow{k_2} 2\,NC \\ I + NC &\xrightarrow{k_3} 2\,NC \end{aligned} \tag{3.3}$$

The precursor conversion is first order, the second step is second order (a coalescence nucleation mechanism) and the third step is autocatalytic growth by the addition of the amorphous species. The rate constants are reported in Table 3.1. Although Mechanism (3.3) has elements of the Finke-Watzky (FW) mechanism,[21] there are important differences. The FW mechanism features a slow nucleation step, directly from precursors that can be six orders of magnitude slower than the

autocatalytic growth. Here, we find that k_2 is five times higher than k_3, and particles nucleate from amorphous intermediates.

We also explored different mechanisms for the bromide reaction (Supplementary Fig. B.21-B.25). The precursor conversion reaction is not very well described by first order kinetics. The data is better described by a second order process (Supplementary Fig. B.21), or by an equilibrium between precursor and intermediate (Supplementary Fig. B.23). We cannot distinguish between the two scenarios based solely on the bromide data but the chloride data indicates that the back reaction is negligible. Taking thus the precursor conversion as second order, we considered the crystallization to be second order (Supplementary Fig. B.22) or autocatalytic (Supplementary Fig. B.24-B.25) and the best fit was found for Mechanism (3.4).

$$\begin{aligned} 2\,\mathrm{P} &\xrightarrow{k_1} 2\,\mathrm{I} \\ 2\,\mathrm{I} &\xrightarrow{k_2} 2\,\mathrm{NC} \\ \mathrm{I} + \mathrm{NC} &\xrightarrow{k_3} 2\,\mathrm{NC} \end{aligned} \tag{3.4}$$

Interestingly, k_2 is refined to the same value as for the chloride reaction but k_3 is much higher for the bromide reaction. This is an exciting result, indicating that the nucleation rate is similar in the bromide and chloride reactions, but that the growth rate is higher in the bromide reaction. Even though our simple model did not take into account differences in nanocrystal concentration, Fig. 3.3d, indicates only a 1.7-fold higher NC concentration in the bromide reaction, insufficient to explain the 17-fold rate enhancement. We infer that differences in surface adsorption of bromide and chloride play a role in the growth rate.

3.2.5 Nucleation and growth mechanism

The nucleation of nanocrystals is observed in Fig. 3.3d. After a sudden increase, the number of crystalline particles stays constant. There is more scatter on the crystal number in the bromide case, but the error on the size is larger due to the more complex PDF refinement (oscillations modeled by sinusoid). Therefore, we conclude that the number of particles in these reactions is set by a nucleation event, which happens soon after reaching 340 °C, with a rate faster than the time resolution of our data. The first observable crystal size by PDF was 1.8 nm. Before observing crystals, the joint SAXS and PDF analysis already detected large amounts of amorphous particles. This intermediate material is a logical consequence of the high reactivity of Zr-OH moieties, produced by precursor conversion.

The size of the amorphous particles was determined to be 1.5 - 2 nm. One could hypothesize that an amorphous particle crystallizes while maintaining its size since there is precedent for an order-disorder transition.[22] However, there is no reason for such a process to be limited to the start of the reaction. In addition, our kinetics modeling indicates a second order nucleation event. Such a second order reaction has a strong dependence on the concentration of the intermediate, which agrees with the absence of continuous nucleation.

Nanocrystal growth happens while the number of total particles decreases over the course of the reaction, see Fig. 3.1g. Amorphous particles are consumed by growth, which can happen by coalescence with a growing nanocrystal or by dissolution into smaller species that grow onto the nanocrystals. Distinguishing the two mechanisms is not straightforward with the data at hand. In the case of $ZrCl_4$, our kinetics modeling does suggest that a reversible equilibrium between intermediates and precursors is less likely than intermediates reacting with themselves or growing onto nanocrystals, thus rather supporting a coalescence mechanism, although we cannot exclude other reactive intermediates formed in low concentrations.

A schematic representation of the proposed mechanism is given in Fig. 3.4. After dissolution of the precursors, we obtain the mixed halide-alkoxide complexes, which decompose into amorphous particles and zirconium tetrahalide complexes. From the amorphous particles, crystals nucleate in a short nucleation event and the rest of the amorphous particles are consumed during crystal growth. We see no evidence for continuous nucleation nor ripening of the crystalline particles. Given that the number of nanocrystals does not change, the final nanocrystal size is set by the nucleation event, irrespective of the growth rate. A larger number of nanocrystals correlates with a smaller final size.

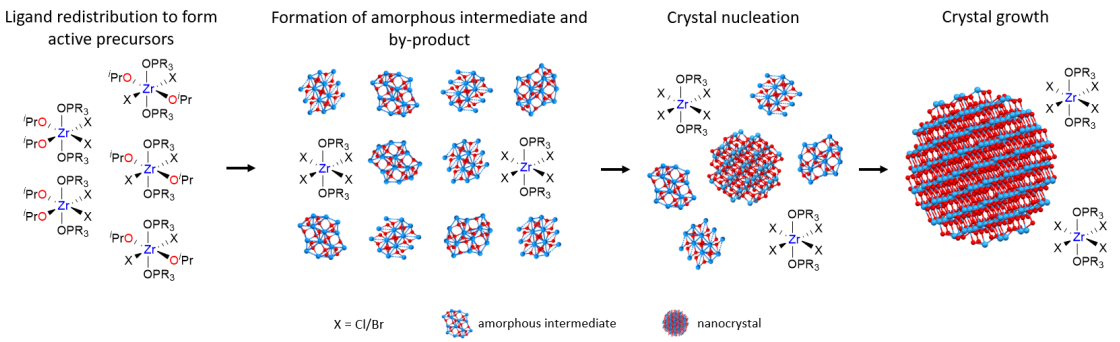

Fig. 3.4 | Schematic representation of the formation mechanism of ZrO_2 nanocrystals. Various steps during the nanocrystal formation from precursor conversion to crystal growth.

3.2.6 Tuning the size using mechanistic insight

According to our mechanism, the number of nanocrystals (thus the size at full yield) is determined by the nucleation event, and the nucleation reaction is second order in the amorphous intermediate. We thus hypothesize that we can control the nanocrystal number and size by controlling the concentration of amorphous particles at the nucleation event. Since all converted precursor turns into amorphous particles, our efforts were focused on controlling the precursor conversion by varying precursor structure. As shown in Supplementary Fig. B.26a, the precursor conversion rate increases in the series:

$$ZrCl_4 + Zr(O\mathit{i}Pr)_4 \cdot \mathit{i}PrOH \; < \; ZrBr_4 + Zr(O\mathit{i}Pr)_4 \cdot \mathit{i}PrOH \; < \; ZrCl_4 + Zr(O\mathit{t}Bu)_4$$

As expected, faster precursor decomposition correlates with a smaller final particle size (Supplementary Fig. B.26b-d). The approach was further validated by modifying the $ZrCl_4$: $Zr(O\mathit{i}Pr)_4 \cdot \mathit{i}PrOH$ reaction. The reaction mixture was held at 300 °C for two hours, reaching 91% precursor conversion. The solution was then quickly heated to 340 °C (Supplementary Fig. B.27). This method was designed to again increase the number of amorphous particles at nucleation (which we assume does not happen at 300 °C). Indeed, the reaction yielded smaller particles compared to the standard reaction (Supplementary Fig. B.27). Finally, mixing $ZrCl_4$ and $ZrBr_4$ delivers an intermediate size, see Fig. B.28.

3.3 Summary

In this work, we elucidated the nucleation and growth mechanism during the non-aqueous synthesis of ZrO_2 nanocrystals from zirconium halide (chloride and bromide) and zirconium isopropoxide in trioctylphosphine oxide. Upon decomposition of the active precursor, a lot of amorphous nanoparticles are formed, which are subsequently converted into nanocrystals. The presence of the amorphous intermediate was evidenced by a combined analysis of X-ray total scattering, small angle X-ray scattering, and NMR. We presented a closed mass balance and kinetic modeling. We determined that the precursor conversion rate is an order of magnitude higher than the crystallization rate. This rate imbalance is responsible for the rapid build-up of amorphous particles. Changing the halide precursor from chloride to bromide, we observed faster kinetics for both precursor conversion and crystallization, together with a smaller crystal size. We found that the nanocrystal size is generally controlled

by the concentration of amorphous particles at nucleation (second order) and we showed multiple strategies for size tuning. These comprehensive results present a leap forward in our understanding of group 4 metal oxide nanocrystals and are expected to enable higher synthetic control over nanocrystal architecture.

3.4 Methods

Materials

$ZrCl_4$ (99.9%), $ZrBr_4$ (99%) and $Zr(OtBu)_4$ (99.9%) were purchased from Strem Chemicals and $Zr(OiPr)_4 \cdot iPrOH$ (99.9%), toluene (99.5%), acetone (99.8%) from Sigma Aldrich and used without further purification. $CDCl_3$ (99.8 atom%) was purchased from Cambridge Isotope laboratories and Benzene-D6 (99.5 atom%) from Apollo scientific, 10/100 mL of activated 4 Å molecular sieves were added and left to stand for 3 days in the glovebox to remove residual water. 3 mm high-throughput NMR tubes (0.58 mm wall thickness) were purchased from Sigma Aldrich. Tri-*n*-octylphosphine oxide (99%) was bought from Strem chemicals and recrystallized according to Owen *et al.*[23]

Instrumentation

Transmission electron microscopy (TEM) imaging was done using a JEOL JEM2800 field emission gun microscope operated at 200 kV equipped with a TVIPS XF416ES TEM camera. Nuclear Magnetic Resonance (NMR) measurements were recorded on Bruker spectrometers operating at a ^1H frequency of 500.13 MHz. ^{31}P spectra were acquired using inverse gated decoupling. The ^{31}P spectra were processed with a line broadening of 5 Hz to reduce noise.

ZrO_2 synthesis

ZrO_2 nanocrystals are synthesized according to our previously published procedure,[2] which was slightly different from the original procedure of Joo *et al.*[8] Typical amounts were 7.5 g recrystallized TOPO, $Zr(OiPr)_4 \cdot iPrOH$ (0.387 g, 1.5 mmol), and $ZrCl_4$ (0.349 g, 1.5 mmol). Synthetic variations include (i) using $ZrBr_4$ (0.616 g, 1.5 mmol) instead of $ZrCl_4$ and (ii) using $Zr(OtBu)_4$ (0.575 g, 1.5 mmol) instead of $Zr(OiPr)_4 \cdot iPrOH$.

Ex situ X-ray total scattering experiments

Samples were prepared by the temporal sampling of reaction aliquot into 3 mm NMR tubes and sealed under Argon atmosphere. We also used 2 mm glass capillaries from Hilgenberg for sampling, but they were prone to breaking upon heating to 80 °C and in general, did not result in higher data quality. The samples were measured either using beamline P21.1 at DESY in Hamburg, Germany or using beamline ID15A at ESRF in Grenoble, France.[24] At ESRF, data were collected at 80 °C (using a nitrogen cryo stream), in rapid acquisition mode, using a 2D Pilatus CdTe 2M detector (1679 × 1475 pixels and 172 × 172 μm pixel size) with a sample-to-detector distance of 264 mm. The incident wavelength of the X-rays was $\lambda = 0.1441$ Å (66.05 keV). Calibration of the experimental setup was performed using a Silicon standard sample. At DESY, ex-situ X-ray scattering data were collected at 80 °C in a home-built aluminium heating block (see *in situ* experiments) in rapid acquisition mode, using a 2D Varex 4343RF amorphous silicon detector (2880 × 2880 pixels and 150 × 150 μm pixel size) with a sample to detector distance of 800 mm. During the measurement, the sample stage was placed in a Helium filled chamber to avoid air scattering. The incident wavelength of the X-rays was $\lambda = 0.1220$ Å (101.62 keV). Calibration of the experimental setup was performed using a Ni standard sample.

In situ X-ray total scattering experiments

Samples were prepared in a nitrogen-filled glovebox by mixing the precursors (see ZrO_2 synthesis) in molten tri-*n*-octylphosphine oxide. The mixture was then transferred to a 3 mm NMR tube and sealed. The samples were measured using beamline P21.1 at DESY in Hamburg, Germany. A home-built aluminum block with an NMR tube holder and cartridge heaters was used to establish the reaction environment. The temperature was first ramped to 340 °C followed by a plateau for 2 hours with Lakeshore 336 cryogenic temperature controller. The sample stage was placed in a helium-filled chamber to avoid air scattering. The data was continuously collected in rapid acquisition mode using a 2D Varex 4343RF amorphous silicon detector (2880 × 2880 pixels and 150 × 150 μm pixel size) with a sample-to-detector distance of 800 mm, with an exposure time of 2 seconds. The incident wavelength of the X-rays was $\lambda = 0.1220$ Å (101.62 keV). Calibration of the experimental setup was performed using a Ni standard sample.

Analysis of X-ray total scattering data

Raw 2D data were corrected for geometrical effects and polarization, then azimuthally integrated to produce 1D scattering intensities versus the magnitude of the momentum transfer Q (where Q = $4\pi \sin\theta/\lambda$ for elastic scattering) using the program Fit2D. The program xPDFsuite with PDFgetX3 was used to perform the background subtraction, further corrections, and normalization to obtain the reduced total scattering structure function F(Q), and Fourier transformation to obtain the pair distribution function, G(r).[25,26] The refinement for each data point was carried out using Diffpy-CMI with a dual-phase fit.[27]

Small angle X-ray scattering experiments

The SAXS experiments were performed on the SWING beamline at SOLEIL synchrotron (Saint Aubin, France). The sample to SAXS detector distances was 0.5 m (for the $ZrBr_4$ synthesis) and 3 m (for the $ZrCl_4$ synthesis). Aliquots collected at different stages of the reactions (during the heating ramp at 300 °C, 320 °C, 340 °C and after 1, 3, 6, 9, 12, 15, 20, 25, 30, 60, 90 and 120 min. at 340 °C). The samples were measured in a flow-through setup which enables the scattering patterns of the empty capillary, the solvent (toluene), and the solutions to be measured at exactly the same spot in the capillary. This allows the same background signals to be subtracted and to obtain the pattern on an absolute scale. Each sample was measured 10 times and the signals were then averaged. The 2D SAXS images were radially averaged using beamline-specific procedures. Then, the capillary signals were subtracted. The signal of the toluene solvent is used to obtain an absolute scale. From the isothermal compressibility of toluene, the intensity at high q is 0.0026 mm^{-1}. This was used to determine a multiplying factor that was applied to all the samples. The solvent signal was then subtracted to obtain all samples in absolute intensity (Fig. 3.1a-b). Details of the fitting are located in Supplementary information.

Contributions

SAXS measurements and analysis were performed by Dr. Laurent Lermusiaux, Dr. Benjamin, and Guillaume Landaburu. The mechanism fitting using COPASI was performed by Mr. Jikson Pulparayil Mathew. Dr. Stefano Checchia, Dr. Susan Rudd Cooper, and Dr. Jette Katja Mathiesen, and Dr. Soham Banerjee helped with the PDF analysis.

Bibliography

[1] R. Pokratath, D. Van den Eynden, S. R. Cooper, J. K. Mathiesen, V. Waser, M. Devereux, S. J. L. Billinge, M. Meuwly, K. M. Ø. Jensen, and J. De Roo. Mechanistic insight into the precursor chemistry of ZrO_2 and HfO_2 nanocrystals; towards size-tunable syntheses. *JACS Au*, 2(4):827–838, 2022.

[2] K. De Keukeleere, S. Coucke, E. De Canck, P. Van Der Voort, F. Delpech, Y. Coppel, Z. Hens, I. Van Driessche, J. S. Owen, and J. De Roo. Stabilization of colloidal Ti, Zr, and Hf oxide nanocrystals by protonated tri-n-octylphosphine oxide (TOPO) and its decomposition products. *Chemistry of Materials*, 29(23):10233–10242, 2017.

[3] S. Mozaffari, W. Li, C. Thompson, S. Ivanov, S. Seifert, B. Lee, L. Kovarik, and A. M. Karim. Colloidal nanoparticle size control: experimental and kinetic modeling investigation of the ligand–metal binding role in controlling the nucleation and growth kinetics. *Nanoscale*, 9(36):13772–13785, 2017.

[4] P. T. Prins, F. Montanarella, K. Dümbgen, Y. Justo, J. C. van der Bok, S. O. M. Hinterding, J. J. Geuchies, J. Maes, K. De Nolf, S. Deelen, H. Meijer, T. Zinn, A. V. Petukhov, F. T. Rabouw, C. De Mello Donega, D. Vanmaekelbergh, and Z. Hens. Extended nucleation and superfocusing in colloidal semiconductor nanocrystal synthesis. *Nano Letters*, 21(6):2487, 2021.

[5] B. Abécassis, M. W. Greenberg, V. Bal, B. M. McMurtry, M. P. Campos, L. Guillemeney, B. Mahler, S. Prevost, L. Sharpnack, M. P. Hendricks, D. DeRosha, E. Bennett, N. Saenz, B. Peters, and J. S. Owen. Persistent nucleation and size dependent attachment kinetics produce monodisperse PbS nanocrystals. *Chemical Science*, 13:4977–4983, 2022.

[6] B. Abécassis, C. Bouet, C. Garnero, D. Constantin, N. Lequeux, S. Ithurria, B. Dubertret, B. R. Pauw, and D. Pontoni. Real-time in situ probing of high-temperature quantum dots solution synthesis. *Nano Letters*, 15(4):2620–2626, 2015.

[7] J. Maes, N. Castro, K. De Nolf, W. Walravens, B. Abécassis, and Z. Hens. Size and concentration determination of colloidal nanocrystals by small-angle X-ray scattering. *Chemistry of Materials*, 30(12):3952–3962, 2018.

[8] J. Joo, T. Yu, Y. W. Kim, H. M. Park, F. Wu, J. Z. Zhang, and T. Hyeon. Multigram scale

synthesis and characterization of monodisperse tetragonal zirconia nanocrystals. *Journal of the American Chemical Society*, 125(21):6553–6557, 2003.

[9] B. M. McMurtry, K. Qian, J. K. Teglasi, A. K. Swarnakar, J. De Roo, and J. S. Owen. Continuous nucleation and size dependent growth kinetics of indium phosphide nanocrystals. *Chemistry of Materials*, 32(10):4358–4368, 2020.

[10] M. P. Campos, J. De Roo, M. W. Greenberg, B. M. McMurtry, M. P. Hendricks, E. Bennett, N. Saenz, M. Y. Sfeir, B. Abécassis, S. K. Ghose, and J. S. Owen. Growth kinetics determine the polydispersity and size of PbS and PbSe nanocrystals. *Chemical Science*, 13(16):4555–4565, 2022.

[11] H. Zheng, R. K. Smith, Y. Jun, C. Kisielowski, U. Dahmen, and A. P. Alivisatos. Observation of single colloidal platinum nanocrystal growth trajectories. *Science*, 324(5932):1309–1312, 2009.

[12] Y. Chen, E. Johnson, and X. Peng. Formation of monodisperse and shape-controlled MnO nanocrystals in non-injection synthesis: Self-focusing via ripening. *Journal of the American Chemical Society*, 129(35):10937–10947, 2007.

[13] Y. A. Yang, H. Wu, K. R. Williams, and Y. C. Cao. Synthesis of CdSe and CdTe nanocrystals without precursor injection. *Angewandte Chemie International Edition*, 44(41):6712–6715, 2005.

[14] E. D. Bojesen and B. B. Iversen. The chemistry of nucleation. *CrystEngComm*, 18(43):8332–8353, 2016.

[15] M. W. Terban and S. J. L. Billinge. Structural analysis of molecular materials using the pair distribution function. *Chemical Reviews*, 122(1):1208–1272, 2022.

[16] M. Zobel, R. B. Neder, and S. A. J. Kimber. Universal solvent restructuring induced by colloidal nanoparticles. *Science*, 347(6219):292–294, 2015.

[17] S. Abe, R. K. Capek, B. De Geyter, and Z. Hens. Tuning the postfocused size of colloidal nanocrystals by the reaction rate: from theory to application. *Acs Nano*, 6(1):42–53, 2012.

[18] M. P. Hendricks, M. P. Campos, G. T. Cleveland, I. Jen-La Plante, and J. S. Owen. A tunable library of substituted thiourea precursors to metal sulfide nanocrystals. *Science*, 348(6240):1226–1230, 2015.

[19] T. Sugimoto, F. Shiba, T. Sekiguchi, and H. Itoh. Spontaneous nucleation of monodisperse silver

halide particles from homogeneous gelatin solution I: silver chloride. *Colloids and Surfaces A: Physicochemical and Engineering Aspects*, 164(2):183–203, 2000.

[20] T. Sugimoto. Underlying mechanisms in size control of uniform nanoparticles. *Journal of Colloid Interface Science*, 309(1):106–118, 2007.

[21] M. A. Watzky and R. G. Finke. Transition metal nanocluster formation kinetic and mechanistic studies. a new mechanism when hydrogen is the reductant: Slow, continuous nucleation and fast autocatalytic surface growth. *Journal of the American Chemical Society*, 119(43):10382–10400, 1997.

[22] S. Jeon, T. Heo, S. Hwang, J. Ciston, K. C. Bustillo, B. W. Reed, J. Ham, S. Kang, S. Kim, J. Lim, K. Lim, J. S. Kim, M. Kang, R. S. Bloom, S. Hong, K. Kim, A. Zettl, W. Y. Kim, P. Ercius, J. Park, and W. C. Lee. Reversible disorder-order transitions in atomic crystal nucleation. *Science*, 371(6528):498–503, 2021.

[23] J. S. Owen, J. Park, P. E. Trudeau, and A. P. Alivisatos. Reaction chemistry and ligand exchange at cadmium-selenide nanocrystal surfaces. *Journal of the American Chemical Society*, 130(37):12279–12280, 2008.

[24] G. B. Vaughan, R. Baker, R. Barret, J. Bonnefoy, T. Buslaps, S. Checchia, D. Duran, F. Fihman, P. Got, and J. Kieffer. ID15A at the ESRF – a beamline for high speed operando X-ray diffraction, diffraction tomography and total scattering. *Journal of Synchrotron Radiation*, 27(2):515–528, 2020.

[25] X. Yang, P. Juhás, C. L. Farrow, and S. J. L. Billinge. xPDFsuite: an end-to-end software solution for high throughput pair distribution function transformation, visualization and analysis. *arXiv preprint arXiv:1402.3163*, 2014.

[26] P. Juhás, T. Davis, C. L. Farrow, and S. J. L. Billinge. PDFgetX3: a rapid and highly automatable program for processing powder diffraction data into total scattering pair distribution functions. *Journal of Applied Crystallography*, 46:560–566, 2013.

[27] P. Juhás, C. L. Farrow, X. Yang, K. R. Knox, and S. J. L. Billinge. Complex modeling: a strategy and software program for combining multiple information sources to solve ill posed structure and nanostructure inverse problems. *Acta Crystallographica*, 71:562–568, 2015.

"Insight must precede application"

- Max Planck

Chapter 4

Local structure distortion and the origin of local dipole in nanoscale ZrO_2[†]

4.1 Introduction

Materials that exhibit switchable polarization have garnered significant interest due to their potential applications in various fields such as energy storage, energy harvesting, infrared sensors, high permittivity capacitors, Ferroelectric Random Access Memory (FeRAM), Radio Frequency Identification (RFID), optoelectronic devices, and other related areas.[1–8] Switchable polarization refers to the ability of certain materials to exhibit a reversible change in the orientation of their electric dipole moment under the application of an external electric field (ferroelectricity), pressure (piezoelectric), or thermal variations (pyroelectric). All ferroelectric materials are pyroelectric and piezoelectric. Therefore ferroelectricity is a unique behavior, which allows the interchange between electrical, mechanical, and thermal energy. To evaluate ferroelectric properties, a P-E hysteresis loop is typically utilized, with P representing the induced polarization and E representing the applied electric field. As illustrated in Figure 4.1a, the P-E response for an ideal linear capacitor is a linear relationship, with the slope of the line representing the capacitance (C). Conversely, for a ferroelectric material, the P-E response differs slightly, as demonstrated in Figure 4.1b. In contrast to dielectric materials, ferroelectric materials maintain their polarization even after the applied electric field has been removed, which is known as remnant polarization (P_R). The polarization can be altered by applying an adequate opposing electric field, referred to as the electric coercivity (E_C). Additionally, the maximum achievable induced po-

[†]Parts of this chapter are adapted from a manuscript in preparation. Local Structure Distortion and the Origin of Local Dipole in Nanoscale Zirconia. Rohan Pokratath, Kumara Cordero-Edwards, Ajmal Roshan Unniram Parambil, Simon J. L. Billinge, Gustau Catalan, Jonathan De Roo*.

larization is known as saturation polarization (P_S). The selection of appropriate materials for various applications is determined by the values of P_R and E_C.

Standard ferroelectric materials, such as BTO ($BaTiO_3$), are not compatible with silicon process technologies, leading to a demand for alternative materials. Since 2011, hafnium oxide has been considered a potential replacement.[9]. The ferroelectric phase of HfO_2 can be stabilized through various methods, including doping, oxygen vacancies, stress/strain, quenching after crystallization, or modification of surface energy.[10] At the nanoscale, the surface energy of materials becomes increasingly significant as the surface area-to-volume ratio increases with decreasing particle size. As a result, structural changes are induced. While both ZrO_2 and HfO_2 exhibit size-induced structural changes, the ferroelectric properties have been reported only for HfO_2 and solid oxide solutions of ZrO_2 and HfO_2. In this chapter, we investigate the possibility of ferroelectricity in ZrO_2 nanocrystals.

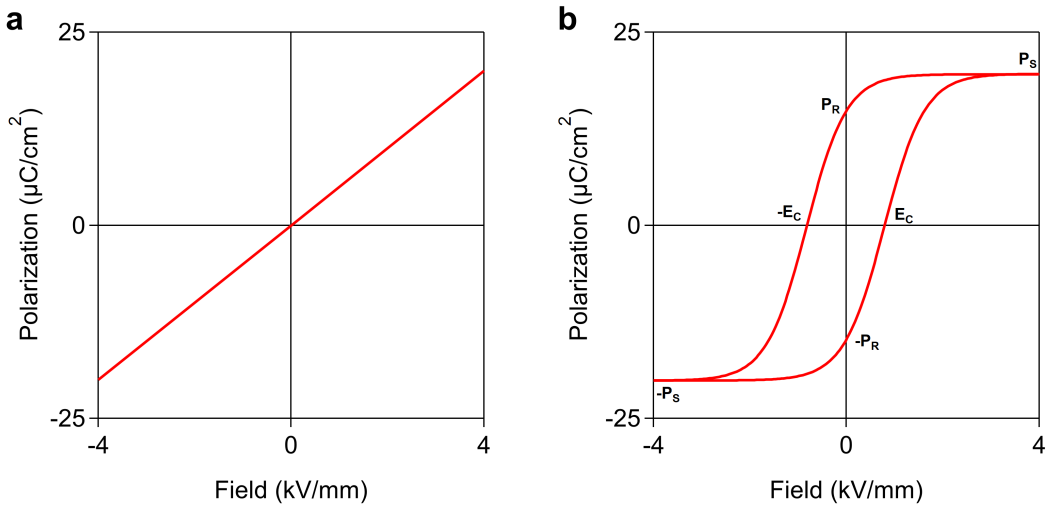

Fig. 4.1 | **Polarization - applied field response.** P-E hysteresis loop for **a** an ideal linear capacitor and **b** ferroelectric material.

4.2 Results and Discussion

4.2.1 Identifying the local distortion

X-ray total scattering with pair distribution function analysis is a well-known technique for the detailed structural analysis of nanostructured materials.[11] The analysis is particularly useful because it accounts for subtle local distortions in the material, allowing the identification of disorders. When 4 nm ZrO_2 nanocrystals were subjected to PDF analysis and modeled with a tetragonal ($P4_2/nmc$) phase, a

significant misfit was observed for the first Zr-Zr peak (3.59 Å). However, all other peaks showed agreement with the model (refer to Fig. 4.2a). Although the fit is quite good ($Rw = 0.11$), the mismatch observed for the first Zr-Zr peak (3.59 Å) could be attributed to minor variations in the local structure of the synthesized nanocrystals, as compared to the average structure. Conventional powder diffraction techniques are limited in detecting such differences due to peak broadening caused by the small crystallite size.[12] The inset in Fig. 4.2a illustrates the source of the mismatch, indicating that it originates from a small deviation in the placement of the model, while the intensity of the two peaks is similar. Dividing the fitting range into two parts, 1.5 - 5 Å (Fig. 4.2b) and 5 - 50 Å (Fig. 4.2c), surprisingly resulted in better individual fits. The refinements were made by fixing the actual crystallite size. The fit parameters obtained for the 1.5 - 50 Å and 5 - 50 Å ranges show similar values, while those for the 1.5 - 5 Å range are different (Supplementary Table C.1). An increase in the lattice parameter *a*, the isotropic thermal motion parameter (Uiso) of oxygen, and a decrease in the lattice parameter *b* are observed in the 1.5 - 5 Å range. The higher Uiso values for the fit range 1.5 - 50 Å indicate the presence of local disorder, suggesting that the local and average structures differ from each other.

In Fig. 4.2d, short-range X-ray PDF simulations are shown for various ZrO_2 phases, along with their deviation from the observed PDF of the synthesized ZrO_2 nanocrystals. In the cubic phase (Fm-3m) of ZrO_2, only one type of short Zr-Zr spacing is observed at 3.63 Å due to its high symmetry. On the other hand, in the tetragonal phase ($P4_2/nmc$), there are two types of pairs with equal contributions to the peak intensity, located at 3.59 Å and 3.62 Å. Although the peak positions are very close, a slightly broader peak is observed. Monoclinic ($P2_1/c$) is the most distorted structure among the different ZrO_2 phases, with even shorter Zr-Zr distances ranging from 3.3 to 4 Å. In this case, two broad peaks are observed. Several orthorhombic phases, such as $Pmn2_1$, $Pca2_1$, Pbca, and Pnma, have been reported with average Zr-Zr distances that fall between those of the monoclinic and tetragonal phases.[13] The Zr-Zr spacing observed in the experimental PDF does not match any known polymorphs and falls between the values for the tetragonal and monoclinic phases. The intensity of the second Zr-O peak (between 4 and 5 Å) is much lower in the experimental PDF than in the calculated tetragonal phase, and multiple peak contributions are observed in the first Zr-O interaction.

Further investigation is needed to confirm the local and average structure. By fitting the local range with various polymorphs, as shown in Supplementary Figure C.1 and Supplementary Table C.2, it was observed that the fits with $P4_2/nmc$ and $Pmn2_1$ were more suitable in terms of peak

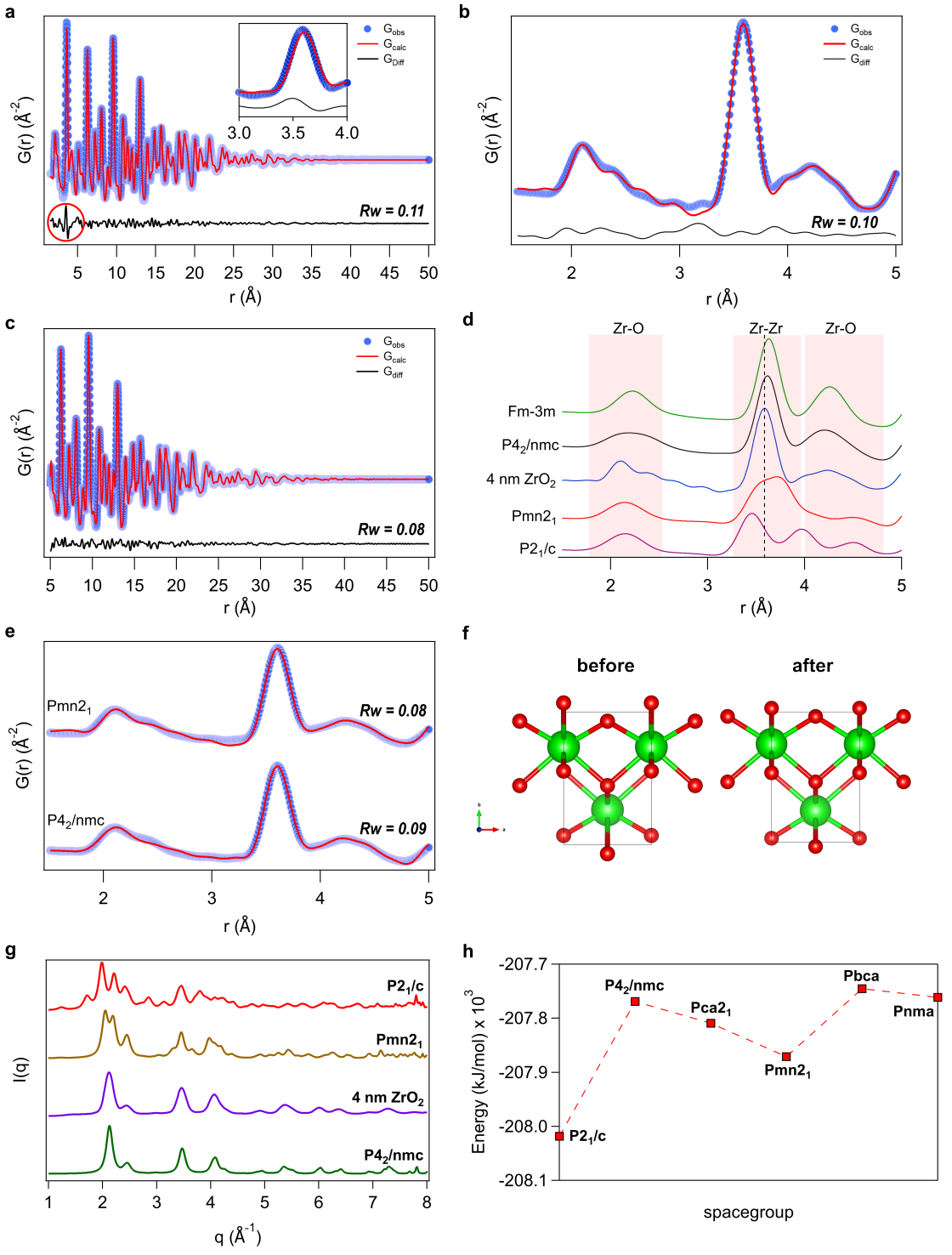

Fig. 4.2 | **Structural analysis of 4 nm ZrO_2 nanocrystal.** Experimental and calculated PDF for 4 nm ZrO_2 nanocrystals with tetragonal($P4_2/nmc$) model for the range **a** 1.5 - 50 Å, **b** 1.5 - 5 Å, and **c** 5 - 50 Å. **d** Comparison of simulated PDF for different ZrO_2 polymorphs with experimental data. The spacegroup of polymorphs used is indicated. **e** Short-range fit obtained for 4 nm ZrO_2 after relaxing the atomic positions of Zr by constraining the symmetry. **f** The unit cell of $Pmn2_1$ before and after optimizing the Zr atom position. **g** Comparison of XRD pattern of 4 nm ZrO_2 with simulated patterns of $P4_2/nmc$, $Pmn2_1$, and $P2_1/c$. The patterns are simulated with an FWHM value of 2 which is calculated for the crystallite size 4 nm for the peak at 2.1 Å^{-1}. **h** The energy of various polymorphs of ZrO_2 calculated using DFT calculations. The corresponding spacegroups are indicated.

positions and refined parameters. However, the Uiso value of oxygen was higher in the $P4_2/nmc$ model. This suggests that the distortions present in the structure were compensated by using a higher Uiso value, leading to a better-fit agreement. Notably, the Uiso values obtained for $Pmn2_1$ are relatively lower, and the fit can be substantially improved by allowing additional freedom to the positions of the Zr atoms given that the symmetry is confined (as shown in Figure 4.2e). The unit cell, before and after refinement of the Zr atom positions, is illustrated in Fig 4.2f, and the refined parameters are listed in Supplementary Table C.3. However, unlike $Pmn2_1$, no such improvement was observed in the case of $P4_2/nmc$. The findings suggest that the local structure can be described as a slightly distorted $Pmn2_1$ phase, which belongs to the non-centrosymmetric orthorhombic crystal system. For comparing the average structure, XRD patterns of $P2_1/c$, $P4_2/nmc$, and $Pmn2_1$ were simulated for the crystallite size 4 nm (Fig. 4.2g). A clear distinction is possible with the reflections of $P4_2/nmc$ phase matching better with the experimental results.

In bulk ZrO_2, monoclinic ($P2_1/c$) is the only stable polymorph at room temperature. However, below a certain crystallite size of 30 nm, the tetragonal ($P4_2/nmc$) phase can be stabilized due to the significant difference in surface free energy.[14] There have also been reports of 20 nm tetragonal crystals.[15] Several colloidal syntheses for monodisperse ZrO_2 have been reported, which are consistent with the predicted critical size for stabilizing the tetragonal phase below 30 nm.[16,17] However, no detailed structural analysis has been performed on these synthesized materials. As the crystal size decreases, the ratio of surface to bulk atoms increases, resulting in higher surface energy. To minimize this energy, the system undergoes a phase transformation. Garvie *et al.* found that the surface energy of the tetragonal structure is lower than that of the monoclinic structure, which leads to the transformation to the tetragonal phase when the crystallite size decreases below 30 nm.[14] According to DFT calculations, the monoclinic phase has the lowest energy, and $Pmn2_1$ is more stable than $P4_2/nmc$ (as shown in Fig. 4.2h). No available information regarding the surface free energy of $Pmn2_1$ is available in the literature.

4.2.2 Nanocrystal size effect

ZrO_2 nanocrystals of various sizes are prepared following our previously established size-tuning methods.[18,19] The standard $ZrCl_4$ and $Zr(O\mathit{i}Pr)_4 \cdot \mathit{i}PrOH$ synthesis is used to synthesize 4 nm nanocrystals. To synthesize smaller nanocrystals, either the reaction is stopped based on the temporal evolution of nanocrystal size discussed in the previous chapter or precursor combinations with $ZrBr_4$ or $Zr(O\mathit{t}Bu)_4$ are used. Larger ZrO_2 nanocrystals were produced by means of continuous injection of

either $Zr(OiPr)_4 \cdot iPrOH$ or $Zr(OtBu)_4$ into the reaction mixture. The XRD patterns of the resulting size series can be seen in Figure 4.3a, and they appear to be similar to the tetragonal phase ($P4_2/nmc$) of ZrO_2. Strong peak broadening is observed for the smaller nanocrystals where the (101) and (002) peaks are overlapping. As the nanocrystal size increases, the peaks become sharper, but no significant changes in the structural features were observed. A distinct difference is visible in the corresponding signals when transformed to PDF, as shown in Figure 4.3b. A shift can be observed for the first Zr-Zr peak, which is correlated with the changes in the crystallite size. As the size increases, the peak position increases and shifts towards the position in the pure tetragonal phase (3.61 Å). The shift is more noticeable for smaller nanocrystals. Additionally, it is worth noting that the second Zr-O peak (shaded region in Fig. 4.3b) for the 2.5 nm nanocrystal appears to have split into two parts, resembling the simulated pattern of the pure monoclinic phase ($P2_1/c$) shown in Fig. 4.2. However, it is important to note that no reflections of this polymorph were detected in the XRD pattern.

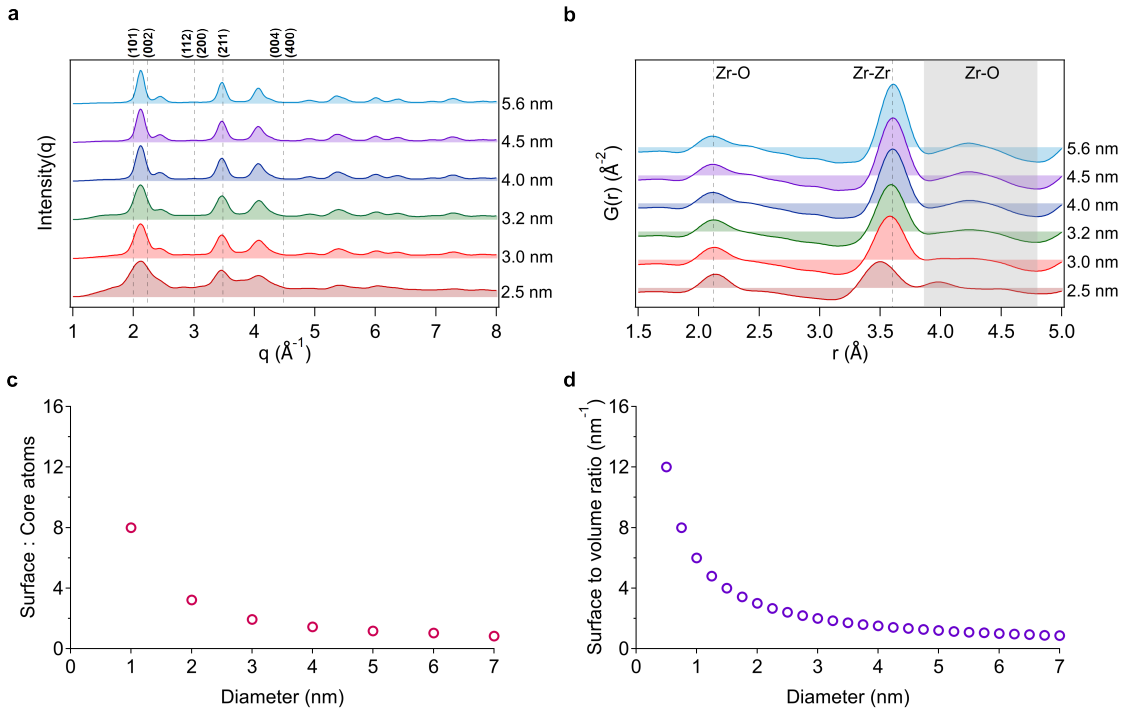

Fig. 4.3 | **Nanocrystal size effect.** The **a** XRD, **b** PDF, **c** surface to core atom ratio, and **d** surface to volume ratio for ZrO_2 nanocrystal size series. The intensity of XRD patterns has been normalized for better visualization. The size of the particles was determined from the corresponding PDF refinements and is shown in the figure. In the calculation of the surface atom ratio, a surface thickness of 0.4 nm was assumed, and only Zr atoms were considered for quantification.

To further investigate this phenomenon, we synthesized several tetragonal nanocrystals of different sizes and simulated their PDFs theoretically. This allowed us to compare the observed peak

shift or splitting with the simulated patterns (Supplementary Fig. C.2). The simulated PDFs showed no peak shift or splitting, supporting the results on local distortions. The only difference observed was in the intensity of the peak, which is attributed to the difference in the number of atom pairs.

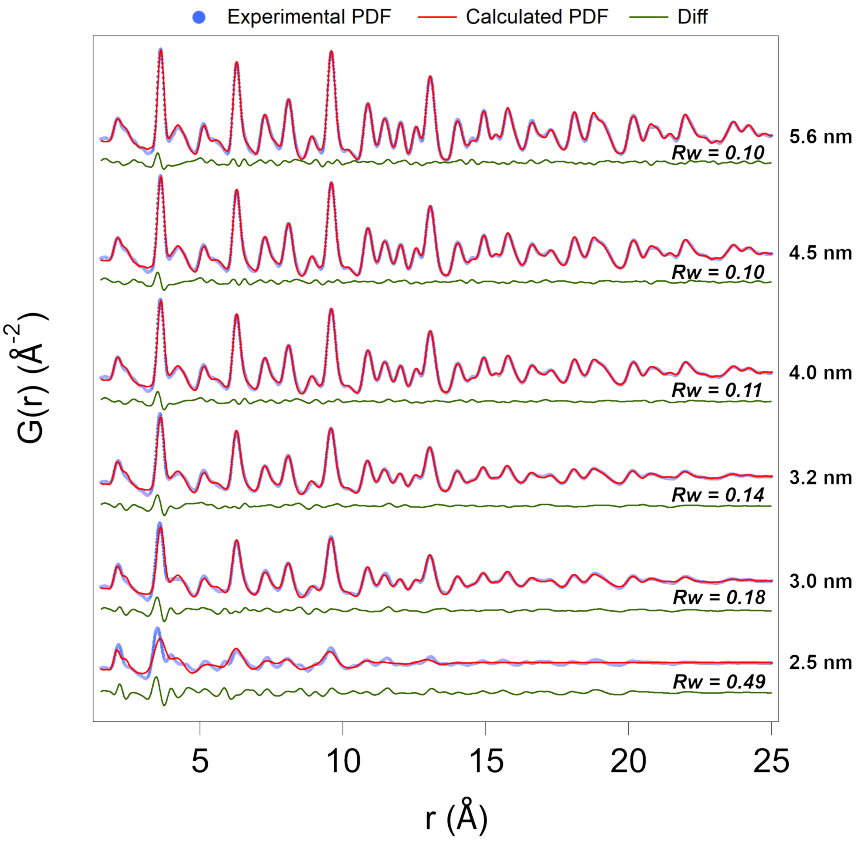

Fig. 4.4 | PDF fitting of ZrO_2 size series. Experimental and calculated PDFs for ZrO_2 nanocrystal size series fitted with $P4_2/nmc$. The refined particle size (psize) and *Rw* value (goodness of fit) are indicated.

Fitting the PDFs with the tetragonal phase ($P4_2/nmc$) results in a poor match (*Rw*) for smaller crystals, as shown in Figure 4.4. The *Rw* value decreases with an increase in crystal size up to 4 nm, after which the changes become minimal. As previously mentioned, when the size of the nanocrystals decreases, the proportion of surface atoms compared to those in the core increases. From Figure 4.3b-c, it can be seen that the ratio of surface to core atoms is approximately 1 when the diameter is 6 nm. As the diameter decreases below 6 nm, the surface atoms dominate over the core atoms. From 6 to 3 nm, the ratio of surface to core atoms increases gradually, and there is a dramatic change below 3 nm. The presence of broken bonds on the terminating surface atoms causes a difference in the bond distance between the surface atom and its nearest neighbor in the

core compared to the bulk. The PDFs shown in Fig. 4.3b suggest that the bond length between the Zr atom on the surface and its nearest neighbor may be shorter than average. This explains the high magnitude of peak shift and increased *Rw* value observed for very small particles (Fig. 4.4). However, it is not possible to perform absolute quantification of the surface contribution due to the contribution of local distortions to the peak shift.

4.2.3 Heat treatment and surface modification

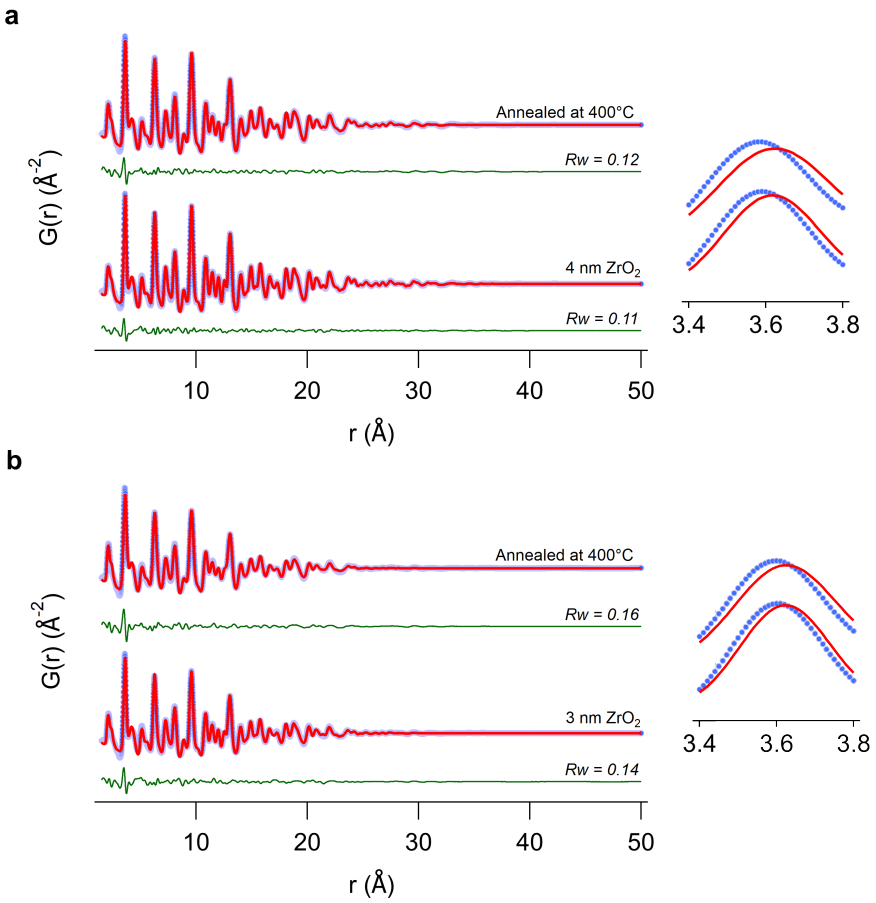

Fig. 4.5 | PDF analysis after heat treatment. The PDF of **a** 4 nm and **b** 3 nm nanocrystals after annealing at 400 °C for 1 hour in air. The misfit at the first Zr-Zr peak is magnified in order to improve visualization. The refined parameters can be found in Supplementary Table C.5,C.6.

Previously reported findings indicate that the synthesized ZrO_2 nanocrystals are capped with TOPO and its decomposition products.[20] To eliminate the effect of the ligands from the analysis, we modified the surface by treating it with dilute HCl. Once the ligands exchanged, the surface chemistry altered and the nanocrystals were no longer colloidally stable. We compared the PDF analysis of the surface-modified nanocrystals with the original ones, and no changes were detected in the peak position or

refined parameters (Supplementary Fig. C.3 and Supplementary Table C.4). Therefore confirms the absence of any significant effect of ligands on our hypothesis.

After annealing the nanocrystals at 400 °C for 1 hour (Fig. 4.5), we observed changes in the structure (Fig. 4.5). The misfit for the first Zr-Zr peak became severe, the crystallite size reduced by about 2 Å, and Uiso values of zirconium and oxygen atoms increased (Supplementary Table C.5,C.6). The higher Uiso values indicate more disorder. Based on the fact that there is only a slight reduction in crystallite size and the XRD patterns appear similar (as shown in Supplementary Fig. C.4), it can be inferred that the observed effect is confined to the surface. However, the specific changes that occurred at the surface are unclear. One possibility is that the presence of phosphorous atoms in the ligands led to the formation of phosphorous oxides at the surface. The increased surface defects can be another possibility. Surface structure needs more investigation and is a part of the ongoing research.

4.2.4 P-V hysteresis loop measurements

As the non-centrosymmetric orthorhombic phase, $Pmn2_1$, is ferroelectric, we conducted switching spectroscopy - piezoelectric force microscopy (SS-PFM) measurements on the ZrO_2 nanocrystals to investigate their properties. SS-PFM is a highly effective technique for accurately characterizing ferroelectric parameters such as Remnant polarization (P_R), Electric coercivity (E_C), and Saturation polarization (P_S).[21] We prepared ZrO_2 based thin films on a conducting electrode *via* spin coating (see methods), which were subsequently annealed at 400 °C to enhance the packing efficiency and minimize the ligand fraction. Supplementary Fig. C.5 displays the AFM (atomic force microscopy) images obtained prior to and following annealing. The spin-coat annealing cycle was repeated 2 times to improve the surface morphology. The thin films were examined to obtain a ferroelectric switching loop.

In SS-PFM, a conductive tip is used in the PFM setup to apply a DC (direct current) bias, in addition to the small AC voltage applied to probe the piezo-response. By ramping this bias, a local ferroelectric switching loop can be measured. The results obtained for the thin film with 4 nm and 3 nm nanocrystals are shown in Fig. 4.6. To avoid the electrostatic interactions between tip and material, the DC bias is not ramped continuously but step-wise and set back to zero volts after each step. There are two loops involved in the experiment. The first loop is where the voltage is turned on, which is called the on state (Supplementary Fig. C.6). In this state, there may be currents

flowing and electrostatic interactions occurring, which is normally disregarded. The second loop is where each point is measured at zero bias, which is called the off state. This measurement is taken just after the associated voltage was applied to the sample. The loops are then formed by tracing the PFM phase versus the applied DC bias. The PFM amplitude as a function of bias exhibits a characteristic "butterfly" shape, as shown in Fig. 4.6, where the amplitude remains almost constant in both stable states but experiences a sharp drop at the coercive voltage. This can be attributed to the fact that during the transition, the sample briefly passes through the paraelectric phase in a localized manner. Since the loop in the on state does not show the typical antiferroelectric loop, and the off state presents a ferroelectric hysteresis loop, the material exhibit ferroelectric properties.

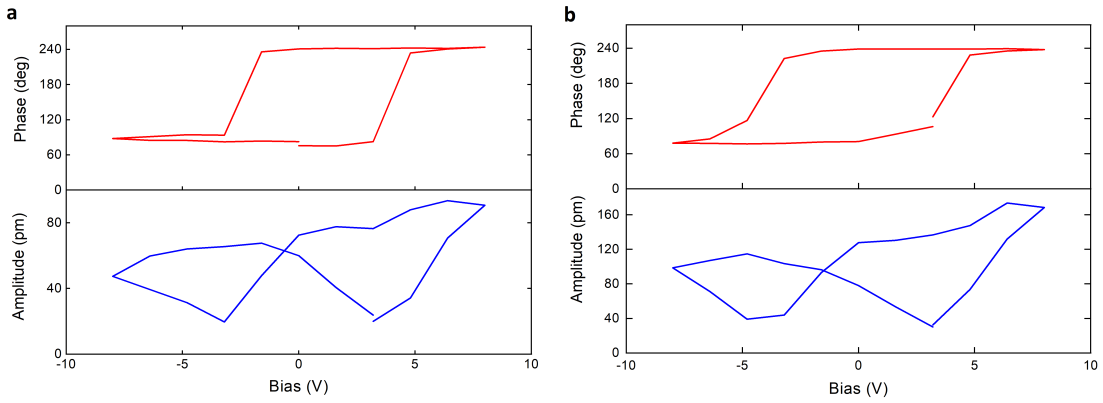

Fig. 4.6 | Hysteresis loop for ZrO_2 nanocrystal thin film. Off state hysteresis loop for **a** 4 nm and **b** 3 nm ZrO_2 nanocrystal thin films.

Further characterization is necessary in this regard. SS-PFM results need to be analyzed in detail. In addition, our attention is directed towards Sawyer-Tower circuit measurements and the development of ferroelectric pellets based on ZrO_2 nanocrystals, which is an ongoing component of the project.

4.3 Summary

A detailed study of the structure of ZrO_2 nanocrystals is conducted through X-ray PDF analysis. We observe a minor deviation in the first Zr-Zr peak, indicating a difference between the local structure of the material and its average structure. The local structure exhibits a slight distortion in $Pmn2_1$, whereas the average structure is $P4_2/nmc$. As $Pmn2_1$ is a non-centrosymmetric orthorhombic structure, the material could possess a local ferroelectric dipole. Additional investigation into the properties of the material was conducted using SS-PFM measurements. Although hysteresis loops were gener-

ated for the nanocrystal-based thin films, further characterization is necessary. Additional methods are chosen for further characterizing ferroelectricity. The identified components, as well as the newly acquired results, will be published in the near future.

4.4 Methods

Materials

$ZrCl_4$ (99.9%), $ZrBr_4$ (99%) and $Zr(OtBu)_4$ (99.9%) were purchased from Strem Chemicals and $Zr(OiPr)_4 \cdot iPrOH$ (99.9%), toluene (99.5%), acetone (99.8%) from Sigma Aldrich and used without further purification. Tri-*n*-octylphosphine oxide (99%) was bought from Strem chemicals and recrystallized according to Owen *et al.*[22]

Nanocrystal synthesis

ZrO_2 nanocrystals are synthesized according to our previously published procedure,[20] which was slightly different from the original procedure of Joo *et al.*[17] Typical amounts were 7.5 g recrystallized TOPO, $Zr(OiPr)_4 \cdot iPrOH$ (0.387 g, 1.5 mmol), and $ZrCl_4$ (0.349 g, 1.5 mmol). Synthetic variations include (i) using $ZrBr_4$ (0.616 g, 1.5 mmol) instead of $ZrCl_4$ and (ii) using $Zr(OtBu)_4$ (0.575 g, 1.5 mmol) instead of $Zr(OiPr)_4 \cdot iPrOH$.

Thin film preparation

Purified nanocrystals are dispersed in toluene at a concentration of 100 mg/mL. 50 μL of sample spin-coated on a 12.5 x 12.5 mm indium tin oxide (ITO) coated substrate at 1000 rpm for 30 seconds, followed by moving the substrate to a hot plate at 400 °C. After one hour, the substrate is taken out and allowed to cool to room temperature.

Synchrotron X-ray total scattering experiments

Samples were prepared in a 1 mm polyamide kapton tube and were measured at beamline 11-ID-BM at Advanced Photon Source, Argonne National Laboratory, USA. X-ray total scattering data were collected at room temperature in rapid acquisition mode, using a Perkin Elmer digital X-ray flat panel amorphous silicon detector (2048 × 2048 pixels and 200 × 200 μm pixel size) with a sample-to-detector distance of 180 mm (11-ID-BM). The incident wavelength of the X-rays was $\lambda = 0.2110$ Å (11-ID-BM). Calibration of the experimental setup was performed using a Ni standard.

Analysis of synchrotron X-ray total scattering data

Raw 2D data were corrected for geometrical effects and polarization, then azimuthally integrated to produce 1D scattering intensities versus the magnitude of the momentum transfer Q (where $Q = 4\pi sin\theta/\lambda$ for elastic scattering) using pyFAI and xpdtools.[23,24] The program xPDFsuite with PDFgetX3 was used to perform the background subtraction, further corrections, and normalization to obtain the reduced total scattering structure function F(Q), and Fourier transformation to obtain the pair distribution function, G(r).[25,26] For data reduction, the following parameters were used after proper background subtraction: Qmin = 0.8 $Å^{-1}$, Qmax = 22 $Å^{-1}$, Rpoly = 0.9 Å. Modeling and fitting were carried out using Diffpy-CMI.[27]

Quantum chemical calculations

Computational calculations were performed with the CP2K program package.[28] Cell parameters were optimized at the DFT level of theory with the hybrid Gaussian and plane waves (GPW) formalism and the Perdew-Burke-Ernzerhof (PBE) functionals.[29] Goedecker–Teter–Hutter (GTH) pseudopotentials[30] and the standard double-ζ MOLOPT basis sets (DZVP– MOLOPT–SR–GTH)[31] have been used for both zirconium and oxygen. The cutoff for the plane wave representation of electron density was set to 400 Ry, while the SCF convergence criterion was set to 1×10^{-6}. CP2K calculations were performed in vacuum without periodic boundary conditions using Wavelet Poisson solver.[32] A box of 17 × 17 × 17 Å was used to achieve a zero electronic density at the edge of the box.

SS-PFM measurements

SS-PFM was performed using the same setup as PFM as described by Jesse *et al.*.[21] A DC bias (VDC) is applied to the AFM tip in addition to the AC probing voltage (VAC), and the bottom electrode is grounded. The PFM phase and amplitude are then recorded while the DC bias is ramped stepwise, going back to zero bias after each step. This produces two measurements: one as a function of the bias applied at the time of the acquisition ('on'), and one as a function of the bias applied just before the acquisition ('off'). To avoid the effects of electrostatic interactions between tip and sample, only the results of the 'off' state are used. Amplitude and phase signals were recorded using an Asylum Research MFP-3D atomic force microscope (AFM) operating in dual resonance tracking (DART) mode, using Nanosensores PPP-EFM cantilevers with a resonance frequency of 75 kHz and a spring constant of 2.8 N/m.

Notes

The ferroelectric property measurement and analysis were performed by Dr. Rohini Kumara Cordero Eduards. The DFT calculations were performed by Mr. Ajmal Roshan Unniram Parambil.

Bibliography

[1] J. Okuno, T. Kunihiro, K. Konishi, H. Maemura, Y. Shuto, F. Sugaya, M. Materano, T. Ali, M. Lederer, K. Kuehnel, K. Seidel, U. Schroeder, T. Mikolajick, M. Tsukamoto, and T. Umebayashi. Demonstration of 1T1C FeRAM arrays for nonvolatile memory applications. pages 1–4, 2021.

[2] T. S. Boescke, J. Mueller, D. Braeuhaus, U. Schroeder, and U. Boettger. Ferroelectricity in hafnium oxide thin films. *Applied Physics Letters*, 99(10), 2011.

[3] M. H. Park, Y. H. Lee, T. Mikolajick, U. Schroeder, and C. S. Hwang. Review and perspective on ferroelectric HfO_2-based thin films for memory applications. *MRS Cummunications*, 8(3):795–808, 2018.

[4] H. S. Philip Wong and Sayeef Salahuddin. Memory leads the way to better computing. *Nature Nanotechnology*, 10(3):191–194, 2015.

[5] M. Gurfinkel, J.S. Suehle, J.B. Bernstein, and Yoram Shapira. Enhanced gate induced drain leakage current in HfO_2 mosfets due to remote interface trap-assisted tunneling. pages 1–4, 2006.

[6] S. Lemey, S. Agneessens, P. Van Torre, K. Baes, J. Vanfleteren, and H. Rogier. Wearable flexible lightweight modular RFID tag with integrated energy harvester. *IEEE Transactions on Microwave Theory and Techniques*, 64(7):2304–2314, 2016.

[7] X. Wei, N. Domingo, Y. Sun, N. Balke, R. E. Dunin-Borkowski, and J. Mayer. Progress on emerging ferroelectric materials for energy harvesting, storage and conversion. *Advanced Energy Materials*, 12(24):2201199, 2022.

[8] A. P. Sharma, M. K. Behera, D. K. Pradhan, S. K. Pradhan, C. E. Bonner, and M. Bahoura. Lead-free relaxor-ferroelectric thin films for energy harvesting from low-grade waste-heat. *Scientific Reports*, 11(1):111, 2021.

[9] T. S. Böscke, J. Müller, D. Bräuhaus, U. Schröder, and U. Böttger. Ferroelectricity in hafnium oxide thin films. *Applied Physics Letters*, 99(10):102903, 2011.

[10] T. Mikolajick and U. Schroeder. Ferroelectricity in bulk hafnia. *Nature Materials*, 20:718–719, 2021.

[11] S. J. L. Billinge and I. Levin. The problem with determining atomic structure at the nanoscale. *Science*, 316(5824):561–565, 2007.

[12] T. Egami and S. J. L. Billinge. Underneath the Bragg Peaks: Structural Analysis of Complex Materials. *Elsevier*, 16:2–481, 2012.

[13] T. D. Huan, V. Sharma, G. A. Rossetti, and R. Ramprasad. Pathways towards ferroelectricity in hafnia. *Physical Review B*, 90:064111, 2014.

[14] R. C. Garvie. Stabilization of the tetragonal structure in zirconia microcrystals. *The Journal of Physical Chemistry*, 82(2):218–224, 1978.

[15] R. D. Robinson, J. Tang, M. L. Steigerwald, L. E. Brus, and I. P. Herman. Raman scattering in $Hf_xZr_{1-x}O_2$ nanoparticles. *Physical Review B*, 71(11):218–224, 2005.

[16] S. W. Depner, K. R. Kort, and S. Banerjee. Precursor control of crystal structure and stoichiometry in twin metal oxide nanocrystals. *CrystEngComm*, 11(5):841–846, 2009.

[17] J. Joo, T. Yu, Y. W. Kim, H. M. Park, F. Wu, J. Z. Zhang, and T. Hyeon. Multigram scale synthesis and characterization of monodisperse tetragonal zirconia nanocrystals. *Journal of the American Chemical Society*, 125(21):6553–6557, 2003.

[18] R. Pokratath, D. Van den Eynden, S. R. Cooper, J. K. Mathiesen, V. Waser, M. Devereux, S. J. L. Billinge, M. Meuwly, K. M. Ø. Jensen, and J. De Roo. Mechanistic insight into the precursor chemistry of ZrO_2 and HfO_2 nanocrystals; towards size-tunable syntheses. *JACS Au*, 2(4):827–838, 2022.

[19] R. Pokratath, L. Lermusiaux, S. Checchia, J. P. Mathew, S. R. Cooper, J. K. Mathiesen, J Landaburu, S. Banerjee, S. Tao, N. Reichholf, S. J. L. Billinge, B. Abécassis, K. M. Ø. Jensen, , and J.* De Roo. An amorphous phase precedes crystallization: Unraveling the colloidal synthesis of zirconium oxide nanocrystals. *ACS Nano*, 17(9):8796–8806, 2023.

[20] K. De Keukeleere, S. Coucke, E. De Canck, P. Van Der Voort, F. Delpech, Y. Coppel, Z. Hens, I. Van Driessche, J. S. Owen, and J. De Roo. Stabilization of colloidal Ti, Zr, and Hf oxide nanocrystals by protonated tri-n-octylphosphine oxide (TOPO) and its decomposition products. *Chemistry of Materials*, 29(23):10233–10242, 2017.

[21] S. Jesse, A. P. Baddorf, and S. V. Kalinin. Switching spectroscopy piezoresponse force microscopy of ferroelectric materials. *Applied Physics Letters*, 88(6), 2006.

[22] J. S. Owen, J. Park, P. E. Trudeau, and A. P. Alivisatos. Reaction chemistry and ligand exchange at cadmium-selenide nanocrystal surfaces. *Journal of the American Chemical Society*, 130(37):12279–12280, 2008.

[23] Giannis Ashiotis, Aurore Deschildre, Zubair Nawaz, Jonathan P. Wright, Dimitrios Karkoulis, Frédéric Emmanuel Picca, and Jérôme Kieffer. The fast azimuthal integration python library:pyFAI. *Journal of Applied Crystallography*, 48(2):510–519, 2015.

[24] C. J. Wright and X. D. Zhou. Computer-assisted area detector masking. *Journal of Synchrotron Radiation*, 24(2):506–508, 2017.

[25] P. Juhás, T. Davis, C. L. Farrow, and S. J. L. Billinge. PDFgetX3: a rapid and highly automatable program for processing powder diffraction data into total scattering pair distribution functions. *Journal of Applied Crystallography*, 46:560–566, 2013.

[26] X. Yang, P. Juhás, C. L. Farrow, and S. J. L. Billinge. xPDFsuite: an end-to-end software solution for high throughput pair distribution function transformation, visualization and analysis. *arXiv preprint arXiv:1402.3163*, 2014.

[27] P. Juhás, C. L. Farrow, X. Yang, K. R. Knox, and S. J. L. Billinge. Complex modeling: a strategy and software program for combining multiple information sources to solve ill posed structure and nanostructure inverse problems. *Acta Crystallographica*, 71:562–568, 2015.

[28] T. D. Kühne, M. Iannuzzi, M. Del Ben, V. V. Rybkin, P. Seewald, F. Stein, T. Laino, R. Z. Khaliullin, O. Schütt, F. Schiffmann, D. Golze, J. Wilhelm, S. Chulkov, M. H. Bani-Hashemian, V. Weber, U. Borštnik, M. Taillefumier, A. S. Jakobovits, A. Lazzaro, H. Pabst, T. Müller, R. Schade, M. Guidon, S. Andermatt, N. Holmberg, G. K. Schenter, A. Hehn, A. Bussy, F. Belleflamme, G. Tabacchi, A. Glöß, M. Lass, I. Bethune, C. J. Mundy, C. Plessl, M. Watkins, J. VandeVondele,

M. Krack, and J. Hutter. CP2K: An electronic structure and molecular dynamics software package - Quickstep: Efficient and accurate electronic structure calculations. *The Journal of Chemical Physics*, 152(19), 2020.

[29] J. P. Perdew, K. Burke, and M. Ernzerhof. Generalized gradient approximation made simple. *Physical Review Letters*, 77:3865–3868, 1996.

[30] S. Goedecker, M. Teter, and J. Hutter. Separable dual-space gaussian pseudopotentials. *Physical Review B*, 54:1703–1710, 1996.

[31] J. VandeVondele and J. Hutter. Gaussian basis sets for accurate calculations on molecular systems in gas and condensed phases. *The Journal of Chemical Physics*, 127(11), 2007.

[32] L. Genovese, T. Deutsch, and S. Goedecker. Efficient and accurate three-dimensional Poisson solver for surface problems. *The Journal of Chemical Physics*, 127(5), 2007.

"In a gentle way, you can shake the world"

- Mahatma Gandhi

Chapter 5

Conclusion and future prospects

The investigation into the synthesis, structure, and properties of ZrO_2 nanocrystals has revealed a fascinating correlation between them. Manipulating one of these factors can lead to changes in the others, demonstrating the interdependence. For example, by controlling the synthesis of ZrO_2 nanocrystals, it is possible to adjust their size, which can then affect the crystalline phase. Understanding this relationship is crucial for developing novel complex group 4 metal oxide materials that have potential applications. This correlation underscores the significance of structure-function relationships in materials chemistry and opens up new avenues for research in this field.

To produce crystalline, monodisperse nanocrystals that are colloidally stable, we opted for surfactant-assisted non-aqueous synthesis. We selected this method because of its proven efficacy. The investigation begins by examining the precursor chemistry of metal chloride and metal isopropoxide in TOPO. Our study revealed how TOPO coordinates with the various precursors and established that the mixed chloroalkoxide serves as the actual precursor in the reaction. Our investigation also revealed a ligand redistribution reaction in the metal chloroalkoxide, which is influenced by the quantity of TOPO present. The extent of TOPO in the reaction mixture plays a crucial role in controlling the reaction, resulting in the formation of nanocrystals with varying properties. This finding highlights the significance of reaction conditions in controlling the final properties of the nanocrystals synthesized. To obtain a comprehensive and consistent structural and molecularly refined characterization of the precursors, intermediates, and by-products, we utilized a combination of NMR spectroscopy, quantum chemical calculations, and X-ray scattering analysis. We quantified other gaseous by-products through GC-FID and identified that propene was the dominant by-product along with isopropyl chloride. Based on these results, we hypothesized an alternative mechanism for precursor decomposition

involving E1 elimination of propene, ligand redistribution to form MCl_4 and $M(OH)_2(OiPr)_2$, and finally condensation to MO_2. These findings provide valuable insights into the reaction mechanism and can be used to optimize the synthesis process for ZrO_2 nanocrystals.[1]

In addition to the precursor decomposition mechanism, we also investigated the nucleation and growth mechanism of ZrO_2 nanocrystals. We observed that the active precursor's decomposition leads to the formation of many amorphous nanoparticles, which subsequently transform into nanocrystals. The formation of the amorphous intermediate was evidenced by a powerful combination of X-ray total scattering, small-angle X-ray scattering, and NMR spectroscopy. Through a closed mass balance and kinetic modeling, we found that the precursor conversion rate is much faster than the crystallization rate, resulting in the rapid build-up of amorphous particles. Furthermore, we discovered that by changing the halide precursor from chloride to bromide, we observed faster kinetics for both precursor conversion and crystallization, as well as smaller crystal sizes. We found that the nanocrystal size is generally controlled by the concentration of amorphous particles during nucleation (second order). Moreover, we demonstrated several strategies for size tuning, which is particularly challenging for group 4 and 5 metal oxides. Our findings provide crucial insights into the nucleation and growth process of ZrO_2 nanocrystals and pave the way for the development of novel size-tunable materials.[2]

To investigate the size-dependent structural changes of zirconia, we conducted a comprehensive structural analysis using X-ray total scattering techniques. We found that based on the slight mismatch of the first Zr-Zr peak in the pair distribution function, the local structure of the material is different from the average structure. We identified that local structure is slightly distorted in the $Pmn2_1$ and $P4_2/nmc$ on average. Notably, the $Pmn2_1$ structure is non-centrosymmetric and orthorhombic, suggesting the possibility of a local ferroelectric dipole in the material. This finding has significant implications for various engineering applications that rely on the ferroelectric properties of materials. Our study provides a deeper understanding of the structural properties of zirconia nanocrystals and highlights the importance of local structure analysis.

In a nutshell, the research provides insights into the structure and formation mechanism of ZrO_2 nanocrystals and highlights the crucial role of understanding the relationship between synthesis, structure, and function in material development.

5.1 Perspectives

I would like to begin this final section of my dissertation with a definition of Dr. Thomas Kuhn's paradigm shift theory, which has inspired me throughout my doctoral work. Science follows a pattern that remains essentially unchanged until the existing theories can no longer explain a phenomenon, resulting in a model crisis. Then the new models evolve that solve the crisis and lead to a paradigm shift. The whole process goes through different phases and finally ends up in a cycle that repeats itself forever. The important message is that everything we see is a perspective and not the truth.

In this dissertation, we have presented several models, including precursor surfactant interaction, precursor decomposition, local structure, nucleation, and growth. These models have been developed to better understand the system and provide a more accurate description of the observed phenomena. While it is important to recognize that all models are inherently imperfect. The research has identified several areas for future exploration. We have provided a comprehensive study of the precursor chemistry in the TOPO synthesis of ZrO_2 and generalized it to HfO_2. It is likely that the nucleation and growth mechanism of HfO_2 will follow a similar pattern. However, an important aspect that we have yet to investigate is the shape of the HfO_2 nanocrystals. Obtaining different shapes such as rods suggests that there might be some interesting underlying reasons. The shape of the HfO_2 nanocrystals may be related to the monoclinic phase that is obtained, which in turn could be linked to the difference in reactivity of the Zr and Hf. It would be highly intriguing to investigate this aspect and explore the potential of extending the size tunability to size-shape tunability.

The obtained results demonstrate that smaller nanocrystals with higher concentration can be obtained using the $ZrBr_4$ precursor compared to $ZrCl_4$. However, the underlying reason for this observation remains unclear and requires further research. One potential explanation is that the superior leaving ability of Br ion could accelerate the reaction, leading to the formation of more amorphous particles and thus more nanocrystals. Similar results can be achieved with $Zr(O\mathit{t}Bu)_4$, which also involves a better-leaving group. However, it should be noted that the interaction between TOPO and various zirconium halide precursors differs. While they exhibit similar behavior in the presence of a limited amount of TOPO (up to 2 eq.), the scenario is completely different in excess of TOPO. This hypothesis is based on titration with TOPO. In the literature, a number of $ZrBr_X$ complexes can be found, which could be a promising starting point. Further investigation of this behavior may offer a more comprehensive understanding of why smaller nanocrystals are produced

when using bromide precursors. This study could also be extended to other halide precursors to gain additional insights.

While the local structure analysis was a part of the dissertation from the beginning, the investigation into the origin of ferroelectric properties was an unexpected discovery. There were many challenges along the way, but I am pleased with how the project ultimately turned out. This ongoing project can be driven in multiple directions. One possibility is to develop nanocrystal-based thin films by optimizing the coating technique and enhancing the surface morphology. Additionally, the development of ZrO_2 nanocrystal-based ferroelectric pellets is also feasible. Further tests to enhance the properties through cation doping, size tuning, and heat treatment can also be conducted. With the increasing demand for energy storage and memory devices, materials with ferroelectric properties have become highly sought after. Although bulk ZrO_2 does not exhibit ferroelectric properties, the discovery of ferroelectric behavior in ZrO_2 nanoparticles is significant for the ferroelectric community.

The never-ending pursuit of comprehending the synthesis, structure, and function of ZrO_2 nanocrystals continues, and excited to discover new insights and breakthroughs.

Bibliography

[1] R. Pokratath, D. Van den Eynden, S. R. Cooper, J. K. Mathiesen, V. Waser, M. Devereux, S. J. L. Billinge, M. Meuwly, K. M. Ø. Jensen, and J. De Roo. Mechanistic insight into the precursor chemistry of ZrO_2 and HfO_2 nanocrystals; towards size-tunable syntheses. *JACS Au*, 2(4):827–838, 2022.

[2] R. Pokratath, L. Lermusiaux, S. Checchia, J. P. Mathew, S. R. Cooper, J. K. Mathiesen, J Landaburu, S. Banerjee, S. Tao, N. Reichholf, S. J. L. Billinge, B. Abécassis, K. M. Ø. Jensen, , and J.* De Roo. An amorphous phase precedes crystallization: Unraveling the colloidal synthesis of zirconium oxide nanocrystals. *ACS Nano*, 17(9):8796–8806, 2023.

Appendix A

Supplementary Information of Chapter 2

A.1 Supplementary Figures

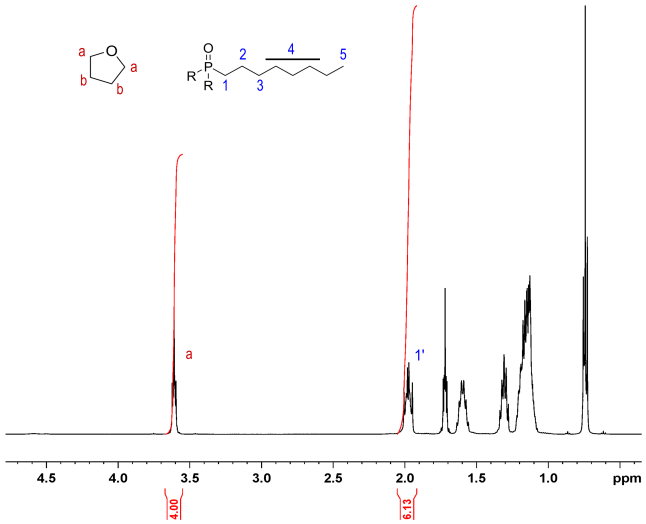

Fig. A.1 | ^{1}H NMR in $CDCl_3$ showing the ratio of integrals for free THF and coordinated TOPO obtained by mixing $ZrCl_4$.2THF with 2 equivalents of TOPO.

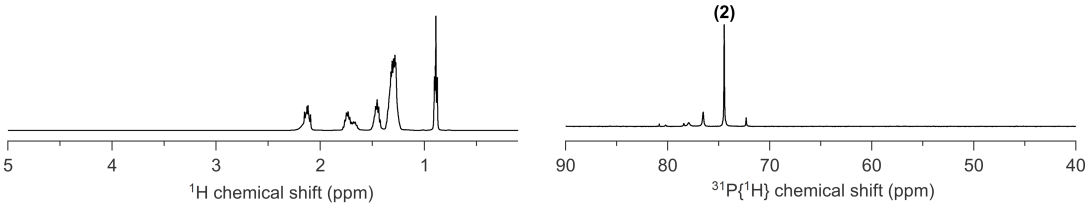

Fig. A.2 | ^{1}H NMR and ^{31}P NMR of $ZrCl_4$ dissolved in $CDCl_3$ with two equivalents of TOPO.

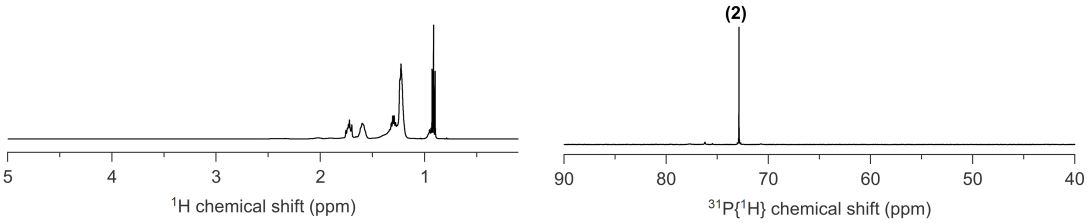

Fig. A.3 | ^{1}H NMR and ^{31}P NMR of $ZrCl_4$ dissolved in C_6D_6 with two equivalents of TOPO.

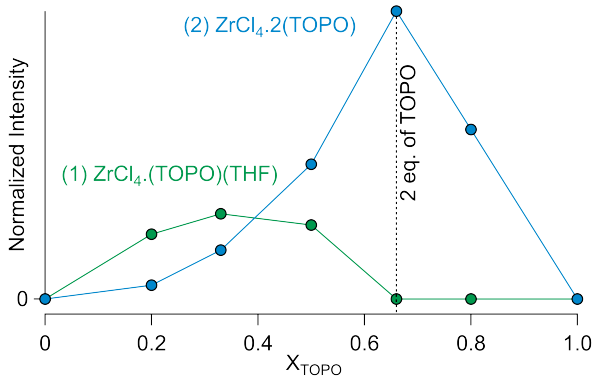

Fig. A.4 | Job plot analysis for the binding event between $ZrCl_4$.2THF and TOPO. The total amount of species mixed for each data point is 0.15 mmol. The asymmetry arises because of the intermediate (1) at low TOPO mole fraction.

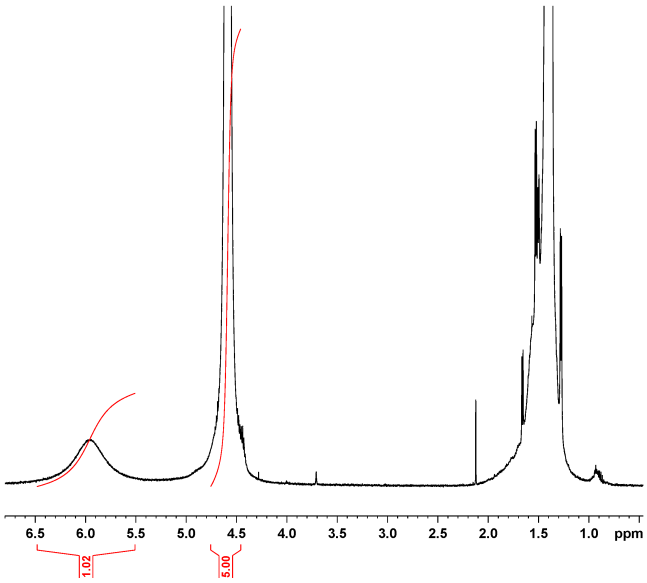

Fig. A.5 | ^{1}H NMR spectrum of zirconium isopropoxide isopropanol complex in $CDCl_3$.

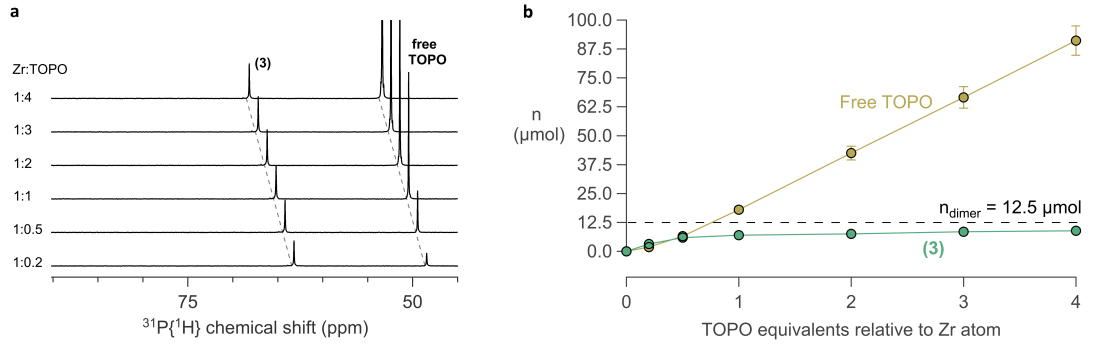

Fig. A.6 | **a** ^{31}P NMR of the titration of a solution of 0.05M Zr(O*i*Pr)$_4$.*i*PrOH in $CDCl_3$ with equivalents of TOPO relative to Zr. The spectra have a relative x-offset of 1 ppm to each other. **b** Variation in TOPO species over the course of the titration. The total amount of Zr dimer in the sample was 12.5 μmol.

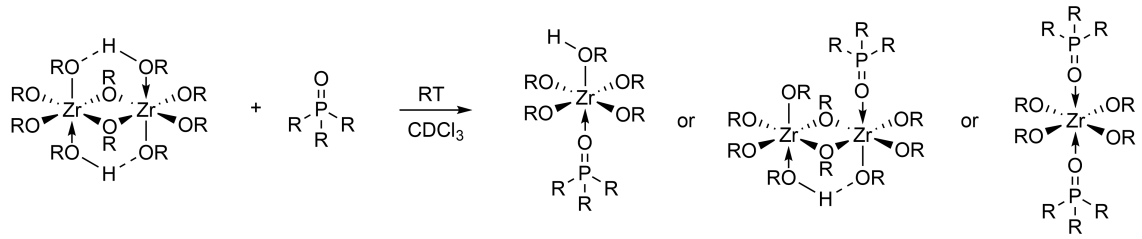

Fig. A.7 | Scheme for the reaction of Zr(O*i*Pr)$_4$.*i*PrOH with TOPO with three possible products.

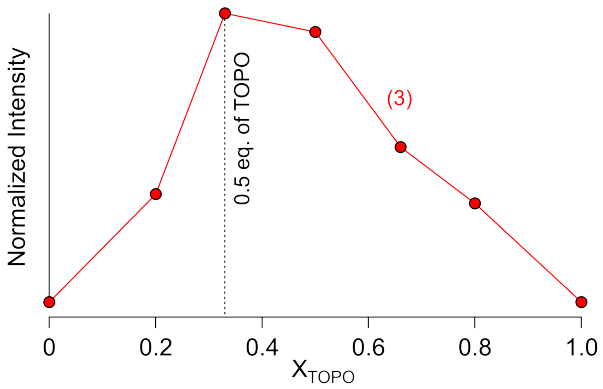

Fig. A.8 | Job plot analysis for the binding event between Zr(O*i*Pr)$_4$.*i*PrOH and TOPO. The total amount of species mixed for each data point is 0.15 mmol.

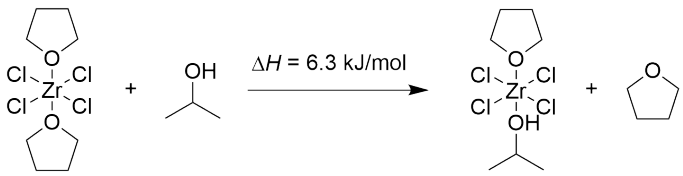

Fig. A.9 | ΔH of the exchange reactions for $ZrCl_4$.2THF with iPrOH.

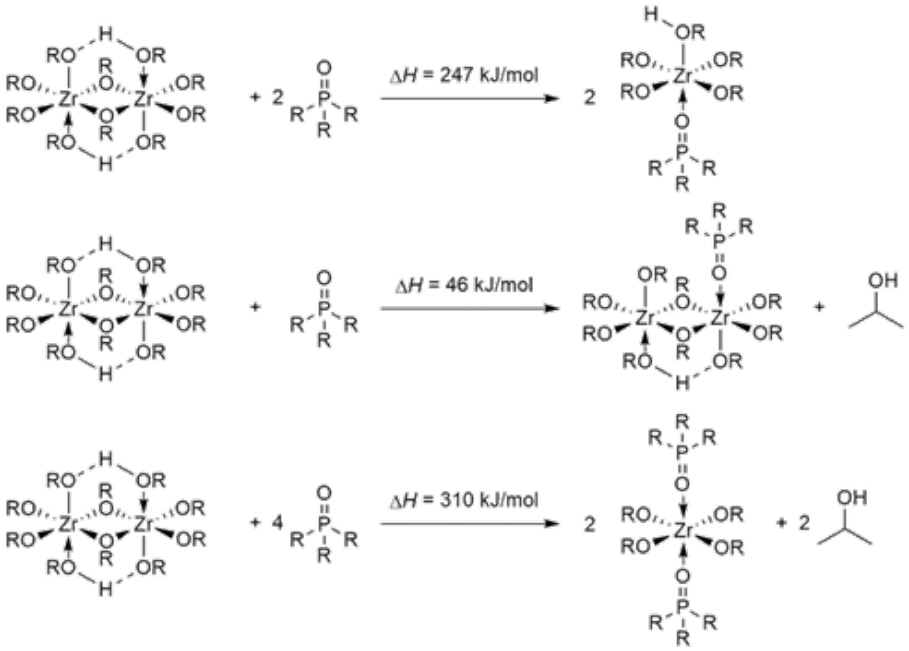

Fig. A.10 | ΔH of the exchange reactions for $Zr(OiPr)_4.i$PrOH with TPPO. (R = propyl).

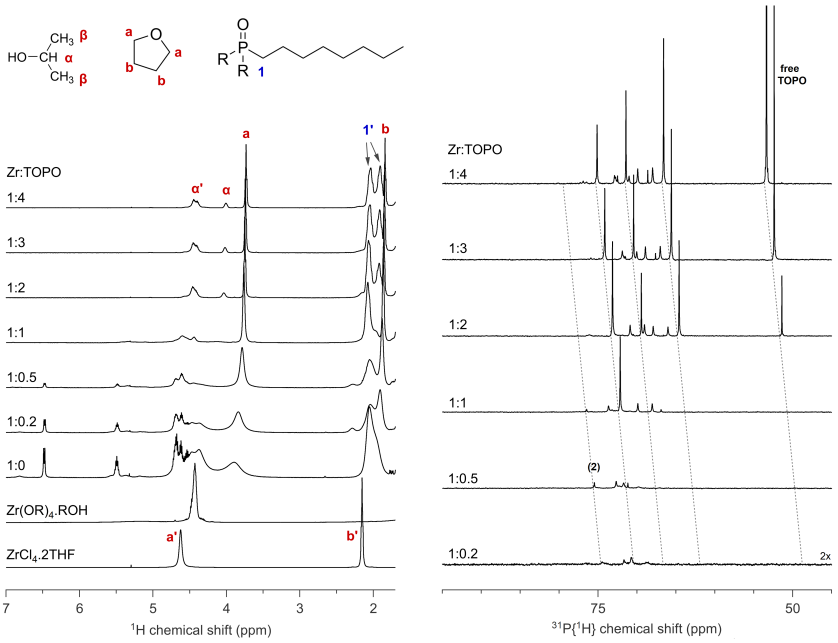

Fig. A.11 | ^{1}H and ^{31}P NMR for the titration of a 1.25 : 1 mixture of $ZrCl_4.2THF$: $Zr(OiPr)_4.i$PrOH with TOPO in $CDCl_3$ at room temperature. The ratio of TOPO to Zr is indicated.

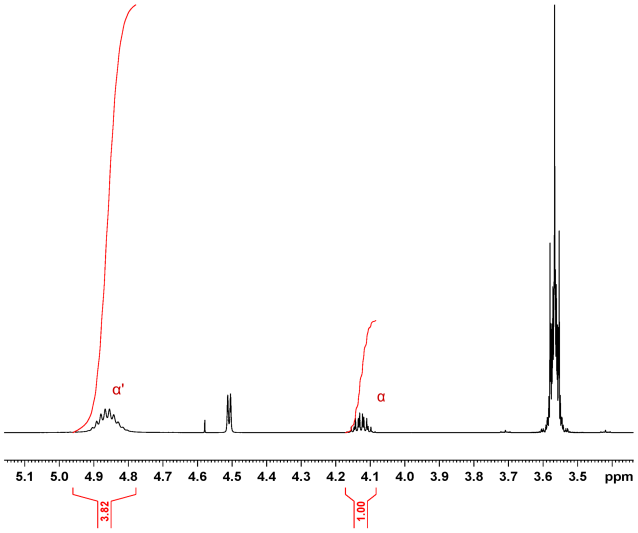

Fig. A.12 | ^{1}H NMR showing the integral ratio between free and coordinated isopropanol for 1.25 : 1 mixture of $ZrCl_4$.2THF : Zr(O*i*Pr)$_4$.*i*PrOH with 3 eq. of TOPO in C_6D_6.

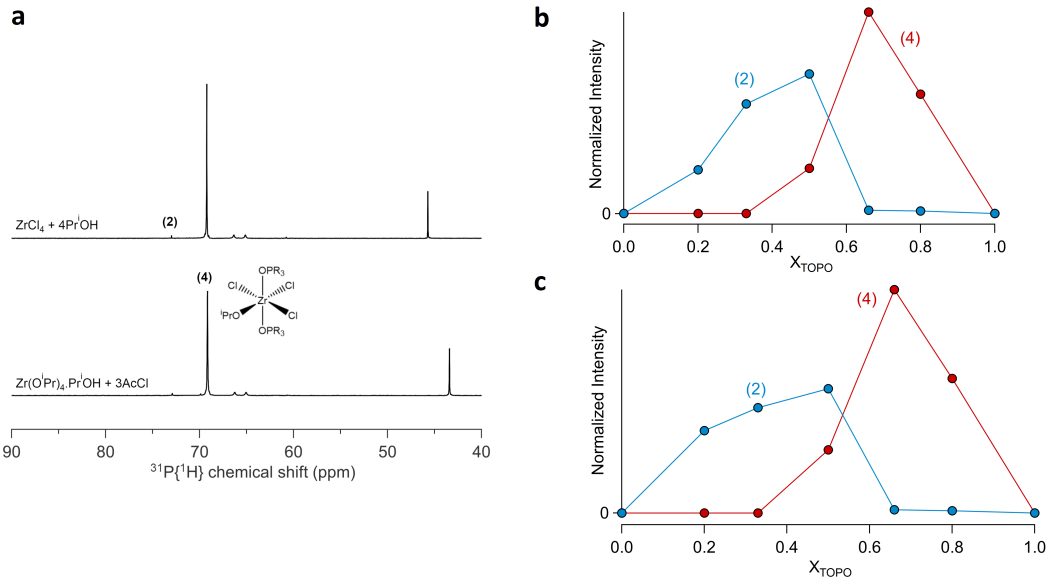

Fig. A.13 | **a** ^{31}P NMR in C_6D_6 for the corresponding reaction product mixed with two TOPO equivalents. The structures of identified intermediates are included next to their respective peaks. The total quantity of Zr in each sample is 100 μmol. Job plot describing the binding event between the product of reaction **b** Zr(O*i*Pr)$_4$.*i*PrOH + 3 AcCl, and **c** $ZrCl_4$ + 4 *i*PrOH and TOPO.

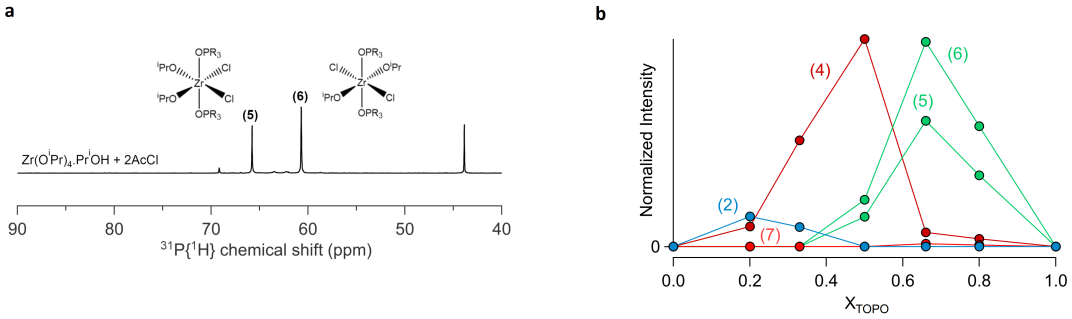

Fig. A.14 | **a** ^{31}P NMR in C_6D_6 for the corresponding reaction product mixed with two TOPO equivalents. The structures of identified intermediates are included next to their respective peaks. The total quantity of Zr in each sample is 100 μmol. **b** Job plot describing the binding event between the product of reaction Zr(O*i*Pr)$_4$.*i*PrOH + 2 AcCl and TOPO.

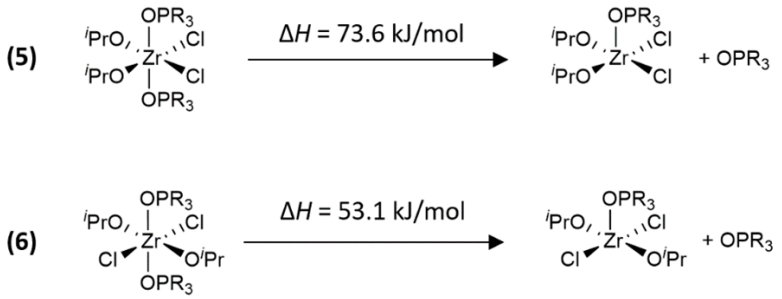

Fig. A.15 | ΔH after removing one TEPO molecule from species (5) and (6) (R=ethyl chain).

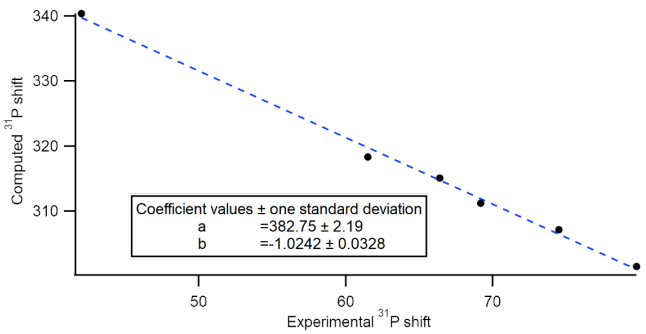

Fig. A.16 | The unscaled, computed ^{31}P NMR chemical shifts from the optimized structures at the DFT level of theory (B3LYP with aug-cc-pVDZ) shows a good linear correlation (R^2 = 0.996) with the experimental chemical shifts in $CDCl_3$. From the linear fit, we extracted an *ad hoc* scaling factor and rescaled the chemical shifts, see Supplementary Table A.3. Please note that this scaling factor is specific for our data set since we used triethylphosphine oxide in our computations and the experimental values belong to the species with trioctylphopshine oxide. The proton chemical shifts (scaled according to the reported scaling factor in Journal of Computational Chemistry 2014, 35 (18), 1388-1394) show also good agreement with experimental values (Supplementary Table A.4).

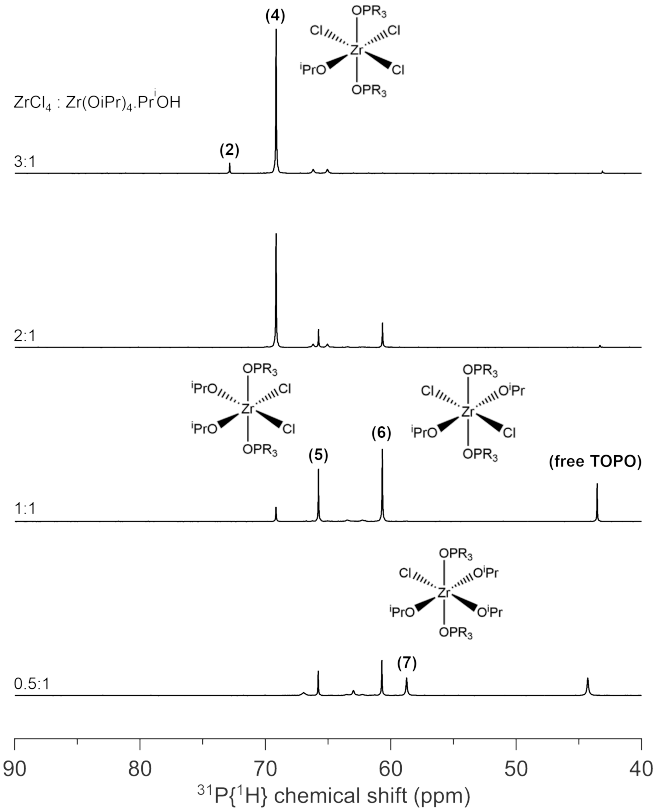

Fig. A.17 | ^{31}P NMR of $ZrCl_4$: $Zr(OiPr)_4.iPrOH$ mixture at room temperature in different ratios with two equivalents of TOPO in C_6D_6.

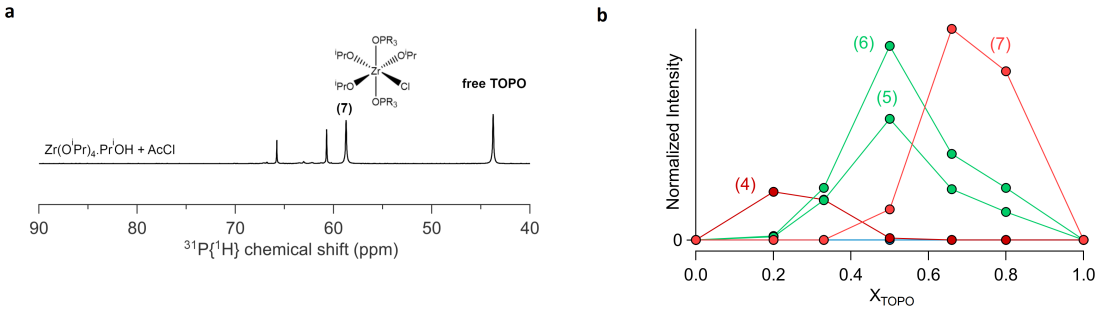

Fig. A.18 | **a** ^{31}P NMR in C_6D_6 for the corresponding reaction product mixed with two TOPO equivalents. The structures of identified intermediates are included next to their respective peaks. The total quantity of Zr in each sample is 100 μmol. **b** Job plot describing the binding event between the product of reaction $Zr(OiPr)_4.iPrOH$ + AcCl and TOPO.

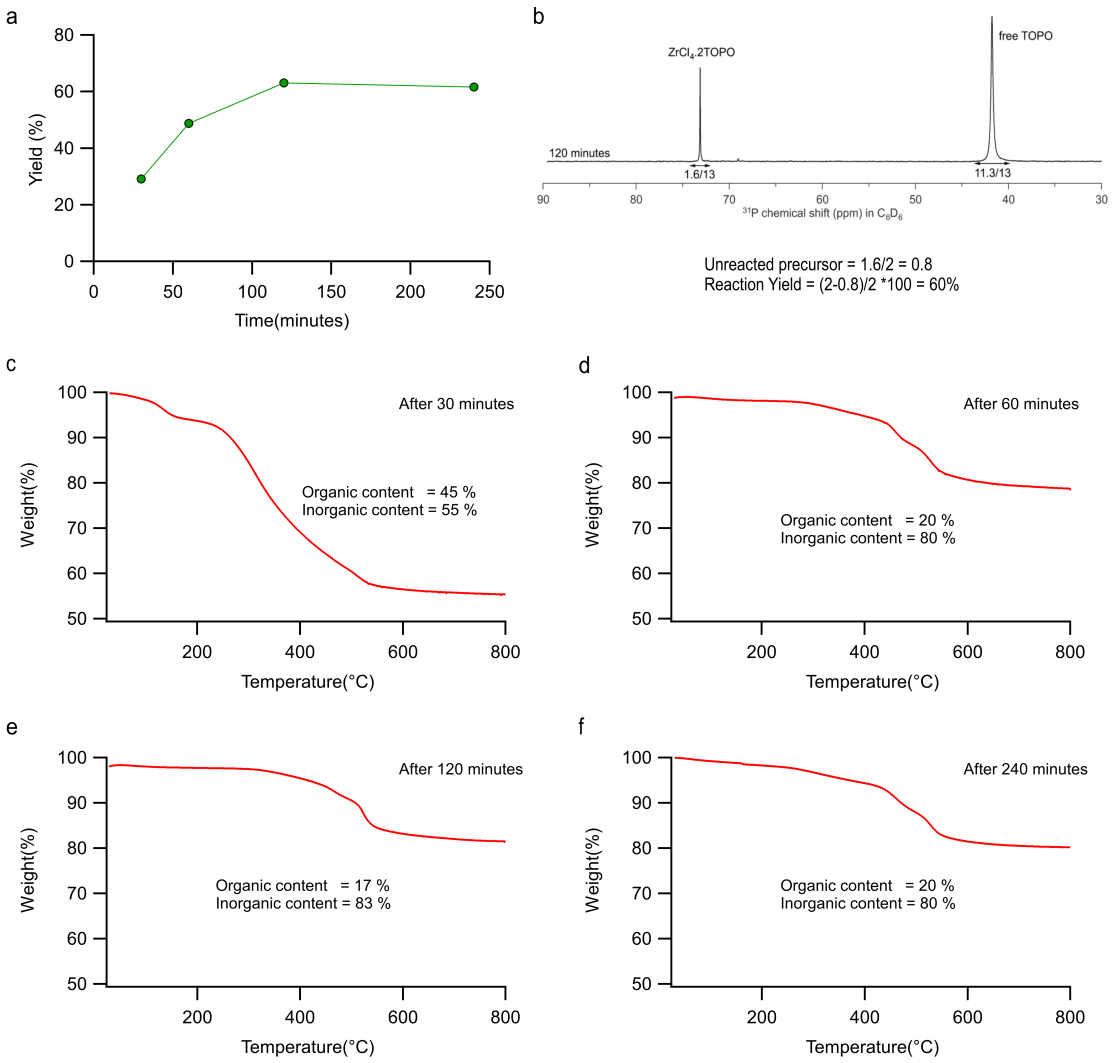

Fig. A.19 | **a** The chemical yield of the reaction was measured by weighing the purified nanocrystals (synthesized from $(ZrCl_4+Zr(O\mathit{i}Pr)_4.\mathit{i}PrOH$ in TOPO) and performing a TGA experiment to determine the inorganic fraction. **b** Calculation of yield with ^{31}P NMR at the end of the reaction. The TGA analysis of the purified sample after **c** 30 minutes **d** 60 minutes **e** 120 minutes and **f** 240 minutes. The determined organic and inorganic fraction are shown.

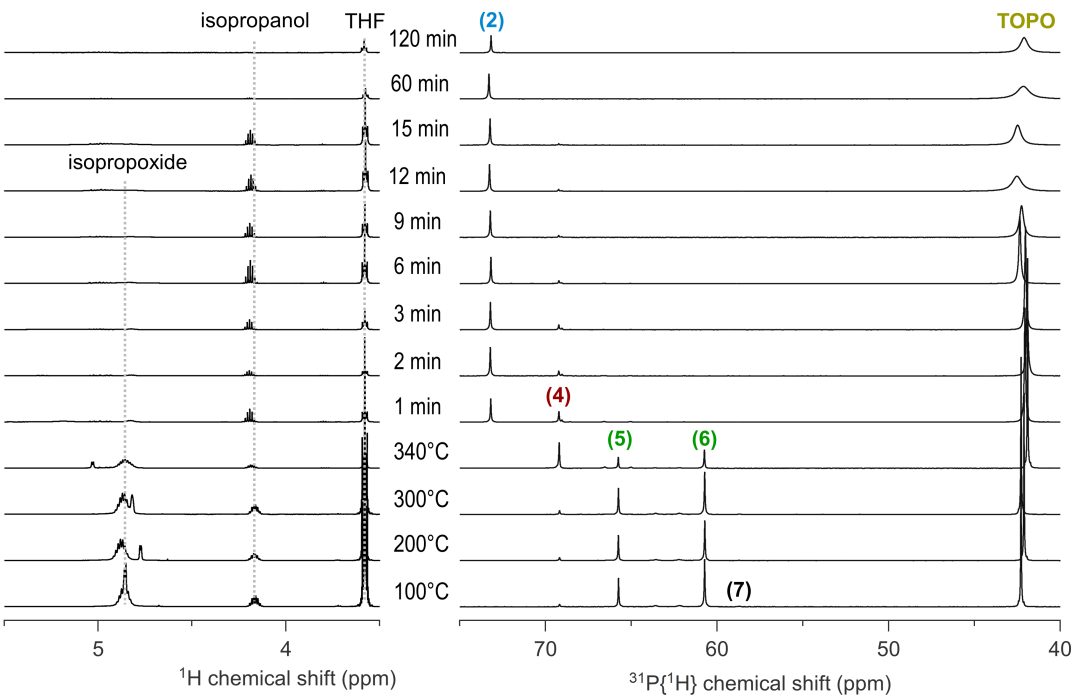

Fig. A.20 | ^{1}H and ^{31}P NMR of the reaction mixture with 1 equivalent of $ZrCl_4.2THF$ in C_6D_6. Aliquots were taken at different temperatures during the ramp and at different times at the final reaction temperature of 340 °C.

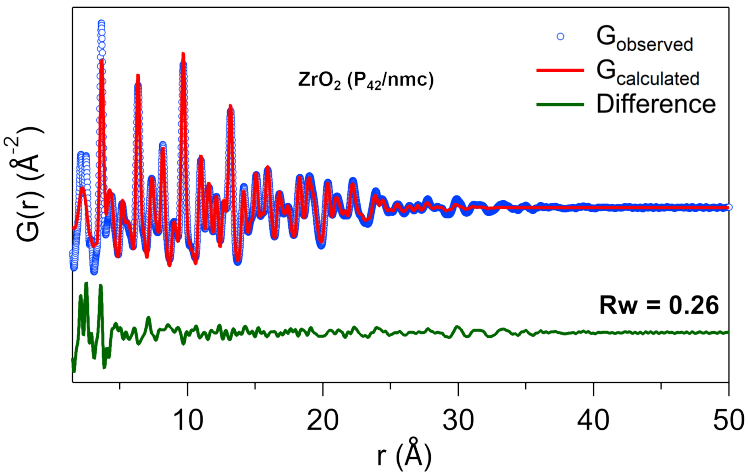

Fig. A.21 | PDF fit for the reaction crude product after 90 minutes of the reaction with the tetragonal ZrO_2 (P_{42}/nmc) single-phase model. Refined parameters are indicated in Supplementary Table A.1.

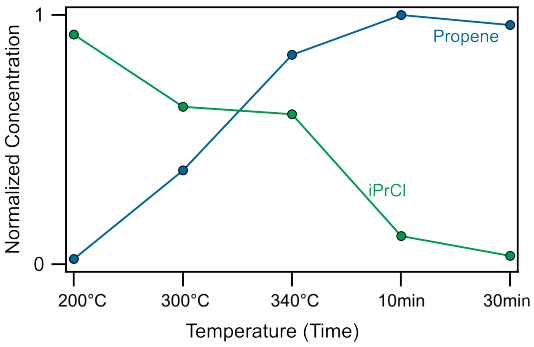

Fig. A.22 | The concentration of propene and isopropyl chloride in the gas phase during the decomposition of *i*PrCl in presence of TOPO and $ZrCl_4$ estimated with GC-FID.

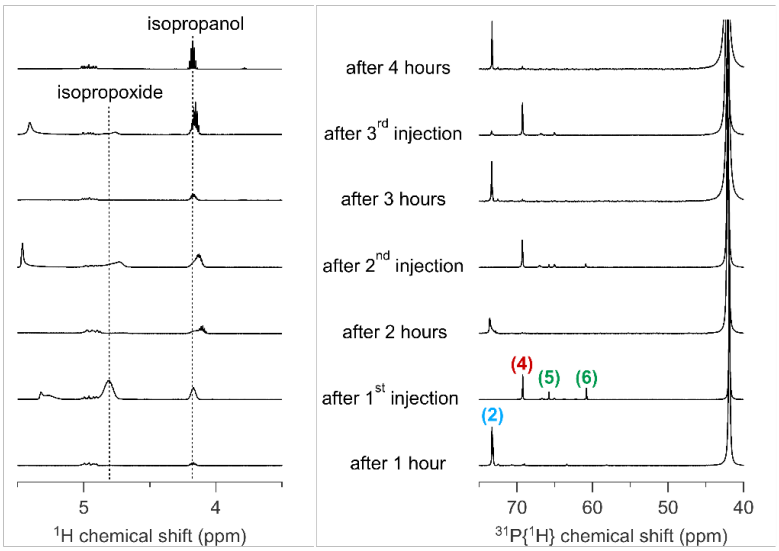

Fig. A.23 | ^{1}H and ^{31}P NMR of the reaction mixture in C_6D_6 before and 30 seconds after each injection. The amount of $ZrCl_4$.2TOPO left after every hour was calculated from ^{31}P NMR and is respectively 0.75, 0.59, 0.50, and 0.36.

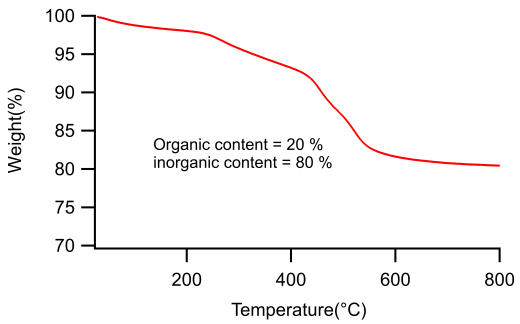

Fig. A.24 | TGA analysis for the final product after seeded growth. Organic and inorganic content is indicated.

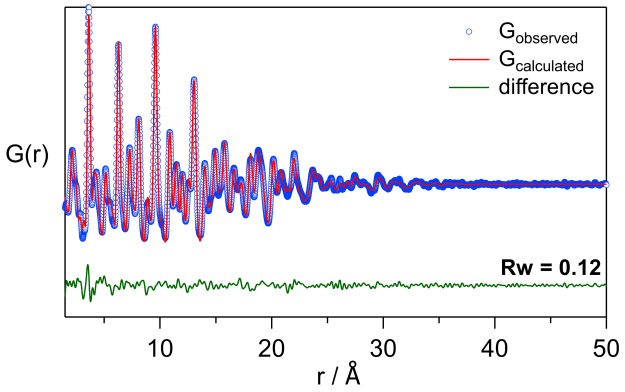

Fig. A.25 | PDF fit for the purified product with the tetragonal ZrO_2 (P_{42}/nmc) single-phase model. Refined parameters are indicated in Supplementary Table A.2.

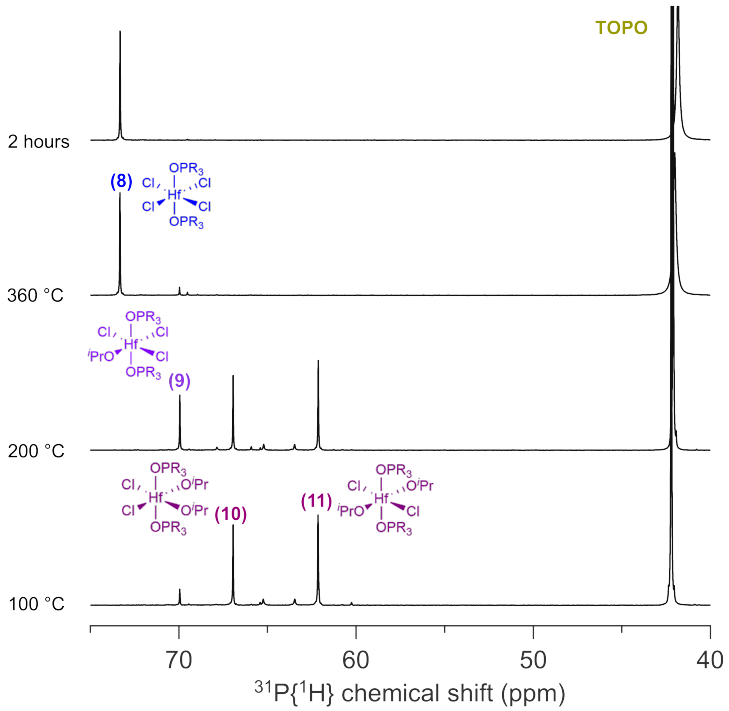

Fig. A.26 | ^{31}P NMR of the reaction mixture with 1 : 1 equivalent of $HfCl_4$: $Hf(OiPr)_4.iPrOH$ in C_6D_6. Aliquots were taken at different temperatures and 2 hours after reaching 360 °C.

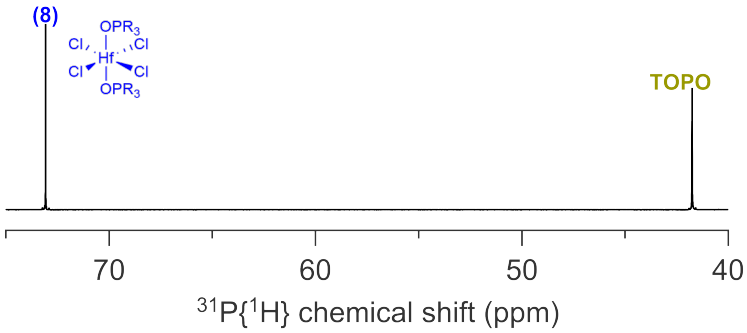

Fig. A.27 | ^{31}P NMR of $HfCl_4$ dissolved in C_6D_6 with four equivalents of TOPO.

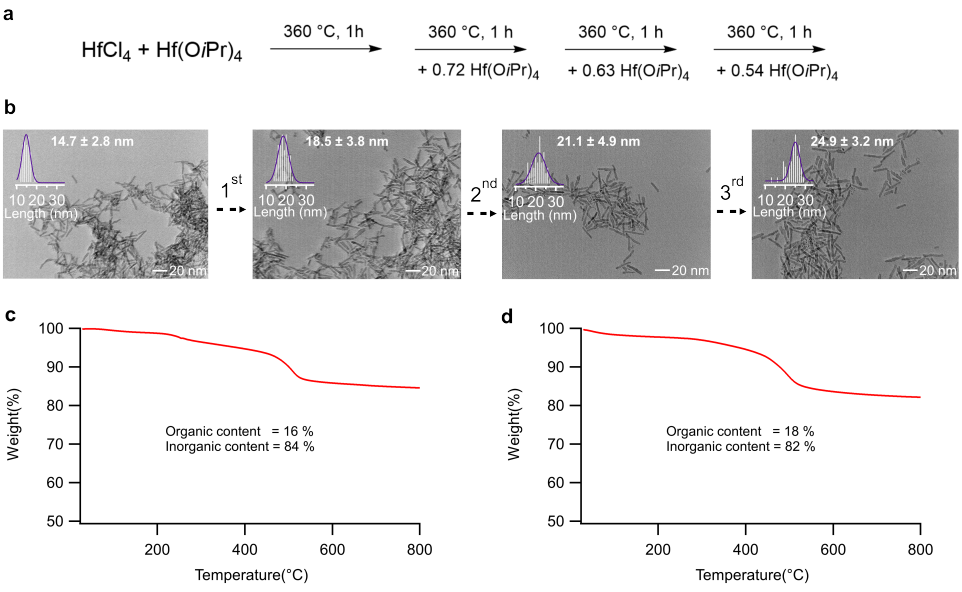

Fig. A.28 | **a** Scheme showing the Hf(O*i*Pr)$_4$.*i*PrOH injection strategy to increase particle size and yield. **b** TEM and histogram of particles before and after each injection. The average particle length is indicated. The width of the nanorod is 2-3 nm. **c** TGA analysis for the final product after two-hour synthesis. Organic and inorganic content is indicated. **d** TGA analysis for the final product after seeded growth. Organic and inorganic content is indicated.

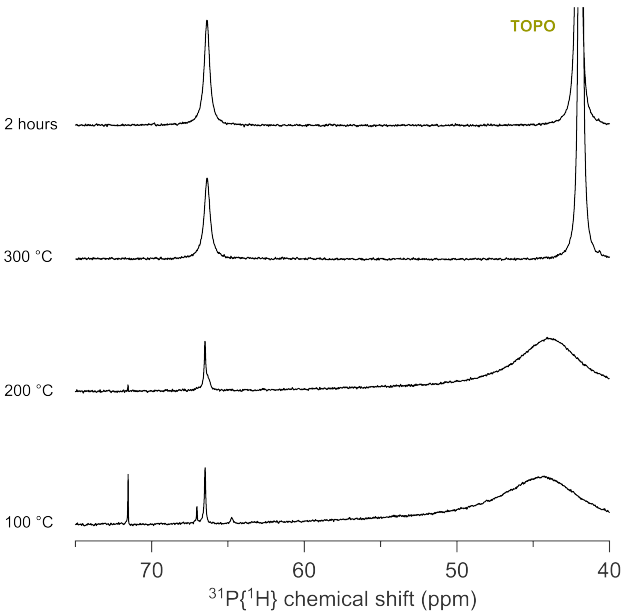

Fig. A.29 | ^{31}P NMR of the reaction mixture with 1 : 1 equivalent of $TiCl_4$: $Ti(OiPr)_4$ in C_6D_6. Aliquots were taken at different temperatures and 2 hours after reaching 300 °C.

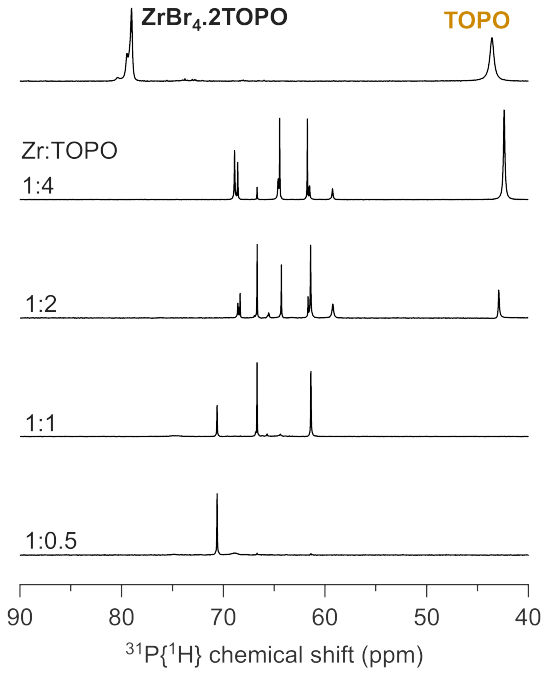

Fig. A.30 | Reaction scheme for the titration of a 1 : 1 mixture of $ZrBr_4$: $Zr(OiPr)_4.iPrOH$ with TOPO in C_6D_6 at room temperature. The reference spectrum for $ZrBr_4$.2TOPO is also shown.

A.2 Supplementary Tables

Table A.1 | Refined parameters after fitting the reaction crude product after 90 minutes of the reaction with the tetragonal ZrO_2 (P_{42}/nmc) single-phase model.

Parameter	Refined Value
Scale	0.6
a(Å)	3.62
c(Å)	5.22
Uiso O(Å^2)	0.029
Uiso Zr(Å^2)	0.008
psize(Å)	34.7

Table A.2 | Refined parameters after fitting the purified product after 90 minutes of the reaction with the tetragonal ZrO_2 (P_{42}/nmc) single-phase model.

Parameter	Refined Value
Scale	1.1
a(Å)	3.60
c(Å)	5.18
Uiso O(Å^2)	0.044
Uiso Zr(Å^2)	0.008
psize(Å)	41.1

Table A.3 | For the optimized structures, we present the unscaled, computed (using TEPO) ^{31}P shift (σ), the scaled computed shift (δ) and the experimentally measured shift (using TOPO).

Structure	Computed σ	Computed δ (ppm)	Experimental δ (ppm)	Goodness of fit (differnce)
TEPO	340.40	41.4	42	-0.60
$ZrCl_2(OiPr)_2$.2TEPO (trans)	318.34	62.9	61.5	1.40
$ZrCl_2(OiPr)_2$.2TEPO (cis)	315.10	66.1	66.4	-0.30
$ZrCl_3$(OiPr).2TEPO	311.18	69.9	69.2	0.70
$ZrCl_4$.2TEPO (trans)	307.14	73.8	74.5	-0.70
$ZrCl_4$.TEPO.THF (trans)	301.44	79.4	79.8	-0.40

Table A.4 | For the optimized structures, we present the unscaled, computed (using TEPO) ^{1}H shift (σ), the scaled computed shift (δ) and the experimentally measured shift (using TOPO).

Structure	Protons	Computed σ	Computed δ (ppm)	Experimental δ (ppm)	Goodness of fit (differnce)
$ZrCl_2(OiPr)_2$.2TEPO (cis)	Cα (OiPr)	26.86	4.60	4.20	0.40
$ZrCl_2(OiPr)_2$.2TEPO (trans)	Cα (OiPr)	26.94	4.50	4.20	0.30
$ZrCl_4$.2THF (trans)	Cα (THF)	26.69	4.75	4.63	0.12
$ZrCl_4$.2THF (trans)	Cβ (THF)	29.33	2.24	2.16	0.08
$ZrCl_4$.TEPO.THF (trans)	Cα (TPPO)	28.97	2.58	2.12	0.46
$ZrCl_4$.TEPO.THF (trans)	Cα (THF)	26.73	4.70	4.63	0.07
$ZrCl_4$.2TEPO (trans)	Cα (TPPO)	29.19	2.37	2.13	0.24

Table A.5 | Refined values after fitting the reaction crude product after 90 minutes of the reaction with a dual-phase model of the tetragonal ZrO_2 (P_{42}/nmc) and the $ZrCl_4$.2TPPO complex (2).

Parameter	Refined Value (Phase 1 - ZrO_2 (P_{42}/nmc)))	Refined Value (Phase 2 - $ZrCl_4$.2TEPO (2))
Scale	0.72	0.54
a(Å)	3.63	-
c(Å)	5.22	-
Uiso O(Å^2)	0.06	0.02
Uiso Zr(Å^2)	0.01	0.011
Uiso Cl(Å^2)	-	0.001
Uiso C(Å^2)	-	0.02
Uiso P(Å^2)	-	0.001
psize(Å)	40	-

Table A.6 | Refined values after fitting the purified product (after three injections) with the tetragonal ZrO_2 (P_{42}/nmc) single-phase model.

Parameter	Refined Value
Scale	1.1
a(Å)	3.60
c(Å)	5.19
Uiso O(Å^2)	0.046
Uiso Zr(Å^2)	0.007
psize(Å)	53.3

Appendix B

Supplementary Information of Chapter 3

B.1 Supplementary methods: SAXS data fitting

The normalized SAXS patterns are used to determine the particle size and concentration by fitting the experimental intensity. As mentioned in the manuscript, we use as a fitting function the sum of the scattering cross section of a distribution of polydisperse spheres and the experimental signal obtained at 300 °C for the $ZrCl_4$ reaction mixture multiplied by a fitting parameters (F) set between 0 and 1:

$$I_{fit} = I^{theoretical}_{Polydisperse\ spheres} + F * I^{experimental}_{ZrCl_4\ at\ 300\,^{\circ}C}$$

The theoretical scattering cross section of distribution of spheres of homogeneous electron density dispersed in a solvent is given by:

$$I^{theoretical}_{Polydisperse\ spheres} = n(\Delta\rho)^2 \int_0^{\infty} V(R)^2 D(R) P(q,R) dR$$

where n is the particle concentration, $\Delta\rho$ is the difference in scattering length density between the particles and the solvent (the contrast), V(R) is the volume of a sphere of radius R, D(R) is the radius distribution, and P(q,R) is the form factor of a sphere. Here, we use a Schultz distribution with

$$D(R) = (\frac{R}{R_0})(Z+1)^{(Z+1)} \frac{e^{-(Z+1)\frac{R}{R_0}}}{\Gamma(Z+1)}$$

Z is related to the polydispersity of the distribution as the polydispersity

$$P(\%) = \frac{100}{\sqrt{Z+1}}$$

The fit function can be written as

$$I_{fit} = I_{Schultz}(n, R_0, Z) + F * I^{experimental}_{ZrCl_4\ at\ 300\,°C}$$

with 4 fitting parameters (R, Z, n and F). In order to provide an estimation of the error bars for the desired parameters (R and n), we performed fits with a fixed value of Z. For each SAXS pattern, Z was varied using increments of 1 from 1 to 500 and we evaluated the quality of the fit using χ^2 within this Z range (Supplementary Fig. B.1a). We measure the χ^2 value for which the fit is minimal (χ^2_{min}) and extract the two Z values which correspond to an increase of χ^2 by 10%: $\chi^2 = \chi^2_{min} * 1.1$. We then use these two Z values, Z_- and Z_+, to extract the corresponding R_{min} and R_{max}, n_{min} and n_{max}, which serve as the limits of the error-bars (Supplementary Fig. B.1b-c).

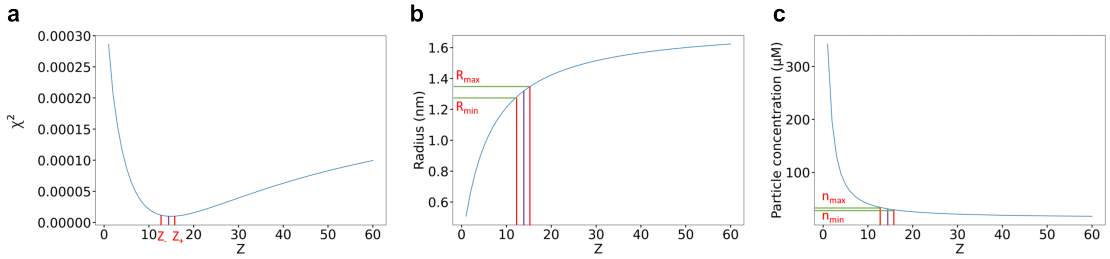

Fig. B.1 | Determination of the error-bar in SAXS data. **a** Example, for one sample, of the estimation of the quality of the fit, using χ^2, when varying the parameter Z, Z_- and Z_+ correspond to Z when χ^2 is 10% larger than its minimum. Variation of the radius **b** and concentration **c** given by the fit when Z is varied.

To account for the intensity of the SAXS signal resulting from the precursors ($I_{precursors}$), we used in our fits the experimental signal of the $ZrCl_4$ reaction at 300 °C ($F * I^{experimental}_{ZrCl_4\ at\ 300\,°C}$), even for the $ZrBr_4$ reaction, which may be surprising. First, all the fits were also performed using instead the SAXS signals of the respective precursors measured at room temperature. Although the fits were visually not as good, the final results were very similar (Supplementary Fig. B.2). Second, for the $ZrCl_4$ synthesis at 300 °C, NMR shows that there is no conversion of the precursors at this stage, confirming this signal can be appropriately used in the fitting. However, this was not the case for the $ZrBr_4$ synthesis which has a faster kinetics, explaining why the $ZrBr_4$ reaction at 300 °C could not be used in the fitting.

The synthesis yield is calculated by dividing the volume of synthesized particles at a given point by the total volume of particles possibly synthesized (estimated from the quantities of chemicals

used). The estimation of the yield by SAXS is obtained by multiplying the number of synthesized particles by the average particle volume $< V >$ with:

$$< V >= \frac{4}{3}\pi \int_0^\infty f(R)R^3 dR$$

and with f(R) given by the Schultz distribution:[1]

$$f(R) = \left[\frac{Z+1}{< R >}\right]^{Z+1} R^Z exp\left[-\left(\frac{Z+1}{< R >}R\right)\right]\frac{1}{\Gamma(Z+1)}$$

Here, Z is related to the width of the distribution and $< R >$ the mean sphere radius, both determined by the fits.

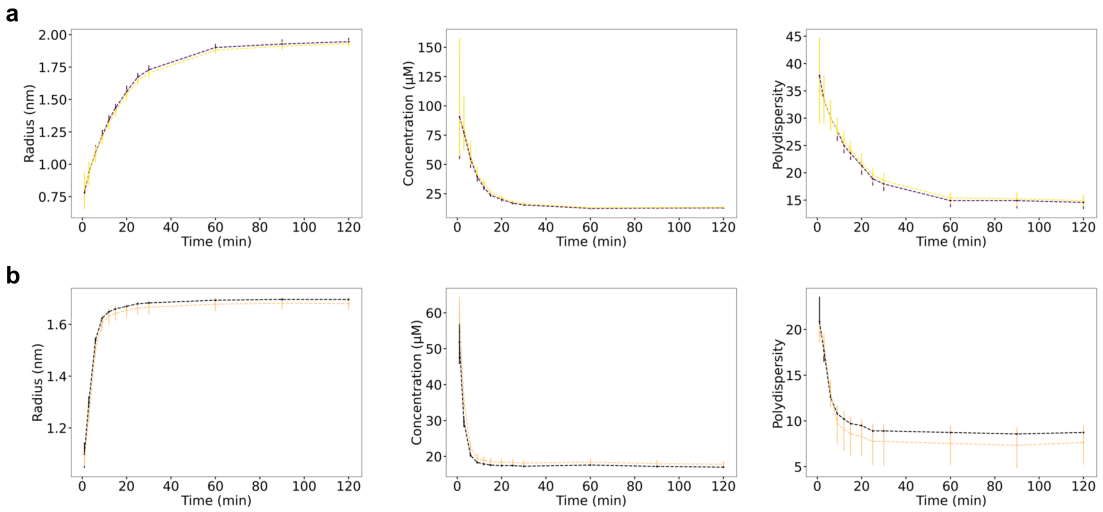

Fig. B.2 | Effect of the precursor signal used in the fitting of the ex situ SAXS measurements. Comparison of the time evolution of the particle size, concentration, and polydispersity for the **a** $ZrCl_4$: $Zr(OiPr)_4 \cdot iPrOH$ and **b** $ZrBr_4$: $Zr(OiPr)_4 \cdot iPrOH$ syntheses. The yellow lines were obtained using in the fits the signal of the corresponding precursors measured at room temperature. The dark lines were obtained using the signal from the $ZrCl_4$ reaction at 300 °C.

B.2 Supplementary Figures: PDF and NMR analysis

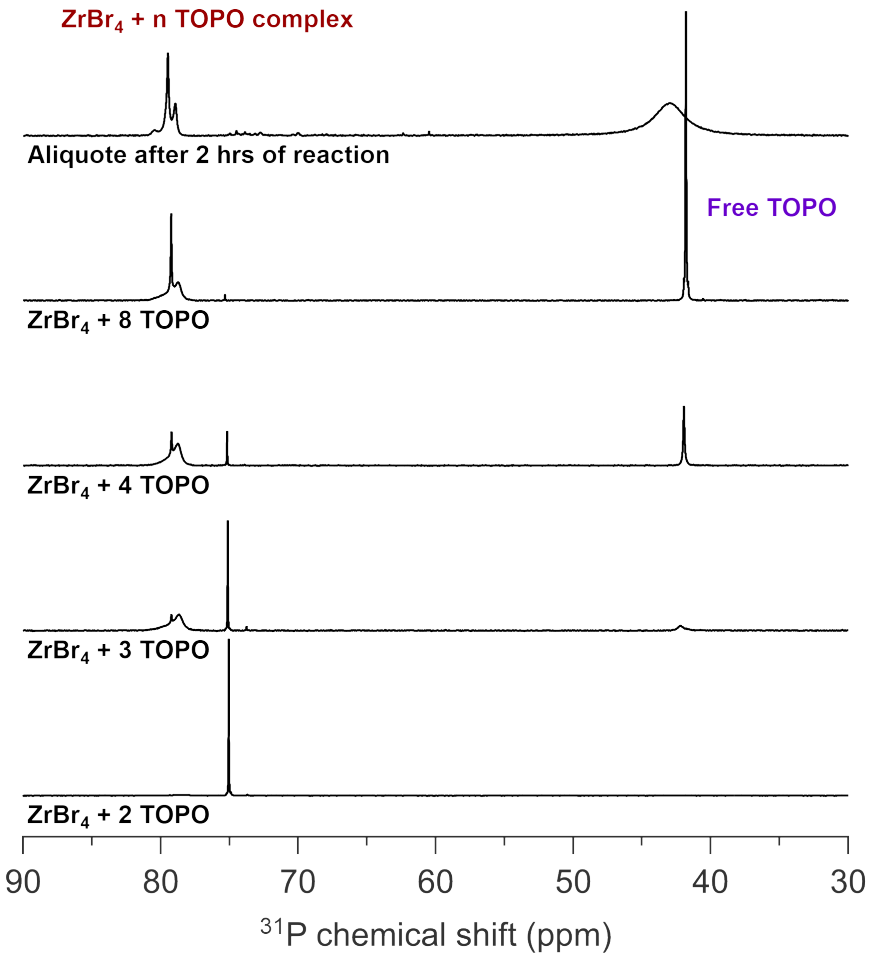

Fig. B.3 | Complexation of TOPO with $ZrBr_4$. ^{31}P NMR spectra in C_6D_6 for reaction aliquot after 2 hours for 1:1 mixture of $ZrBr_4$: $Zr(O\mathit{i}Pr)_4 \cdot \mathit{i}PrOH$ showing the formation of $ZrBr_4$ + n TOPO complex as a by-product. The NMR shift for the complexes is independently verified by mixing $ZrBr_4$ with different equivalents of TOPO. While two TOPO equivalents seem to cleanly yield the expected $ZrBr_4 \cdot 2$ TOPO complex, higher TOPO equivalents result in an unknown complex.

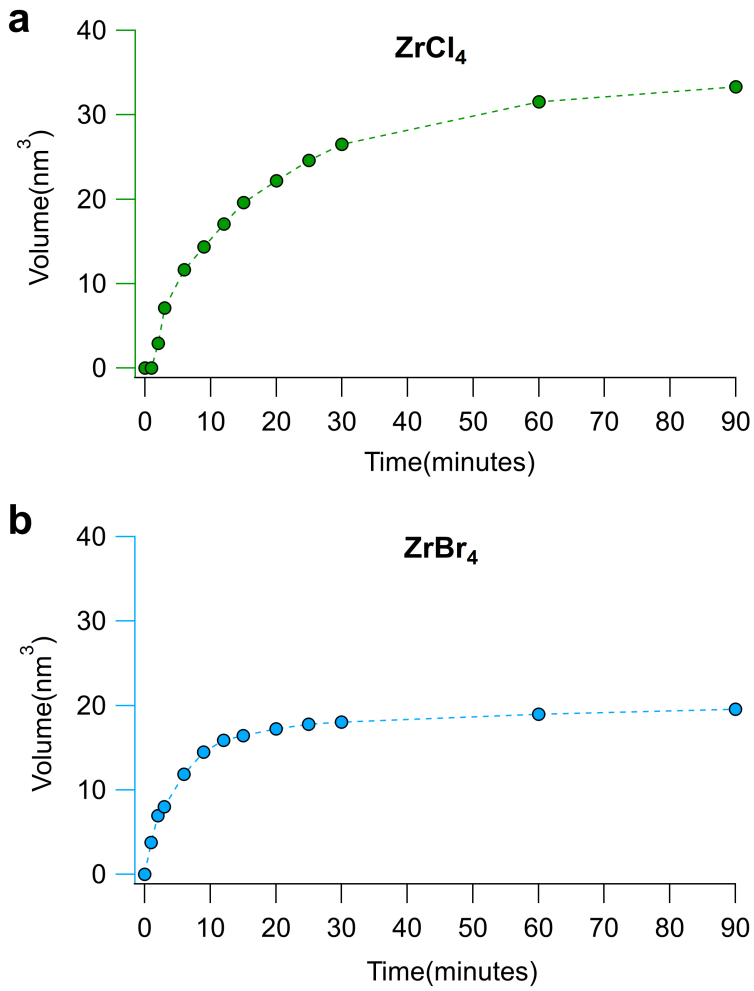

Fig. B.4 | **Volumetric changes during crystal growth.** Comparison of volumetric changes during crystal growth for the reaction with **a** 1:1 mixture of $ZrCl_4$: $Zr(OiPr)_4 \cdot iPrOH$. and **b** 1:1 mixture of $ZrBr_4$: $Zr(OiPr)_4 \cdot iPrOH$.

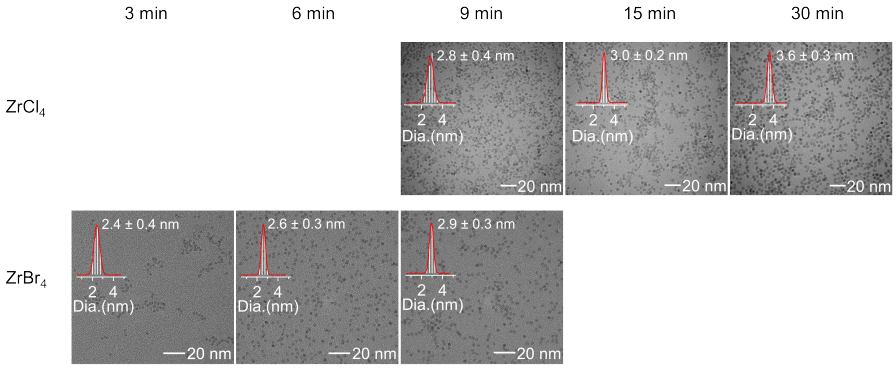

Fig. B.5 | **Nanocrystal size evolution with TEM.** TEM image and histogram of particles formed from 1:1 reaction mixture of $ZrCl_4$: $Zr(OiPr)_4 \cdot iPrOH$ (after 9, 15, and 30 minutes) and from 1:1 reaction mixture of $ZrBr_4$: $Zr(OiPr)_4 \cdot iPrOH$ (after 3, 6, and 9 minutes).

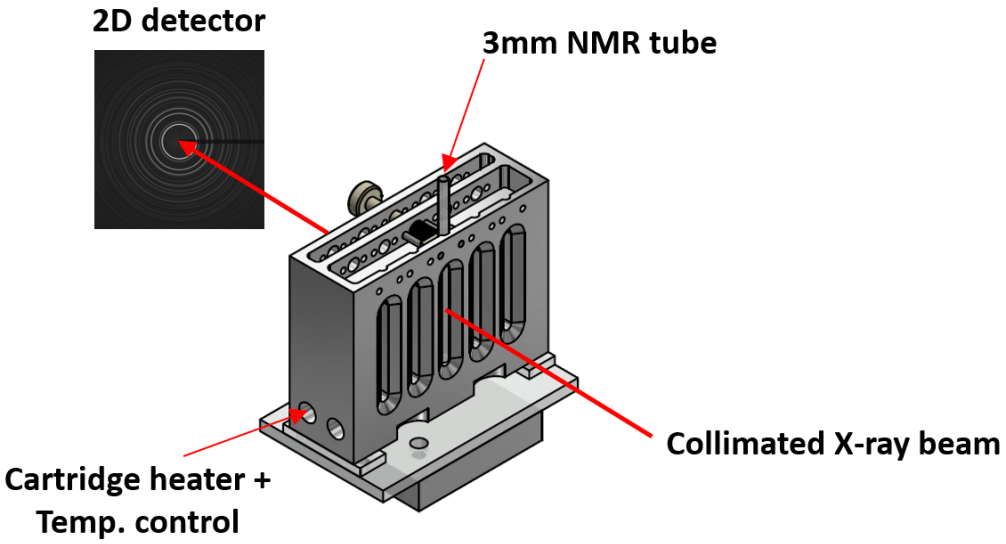

Fig. B.6 | **In situ PDF measurement setup.** Custom made experimental setup for *in situ* PDF measurement. The reaction mixture is inserted in a 3 mm NMR tube and placed inside the setup. Cartridge heaters are used to heat the block.

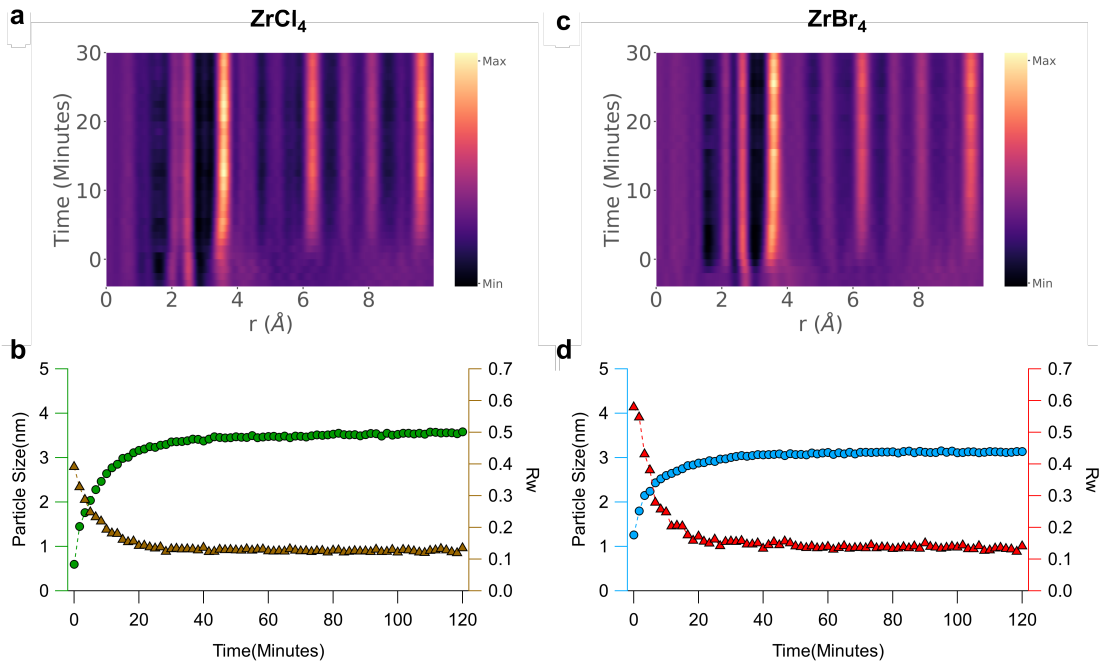

Fig. B.7 | **In situ PDF intensity plot and refined parameters.** *In situ* PDF data and refined parameters (size and *Rw*) for 1:1 mixture of **a-b** $ZrCl_4$: $Zr(OiPr)_4 \cdot iPrOH$ and 1:1 mixture of **c-d** $ZrBr_4$: $Zr(OiPr)_4 \cdot iPrOH$.

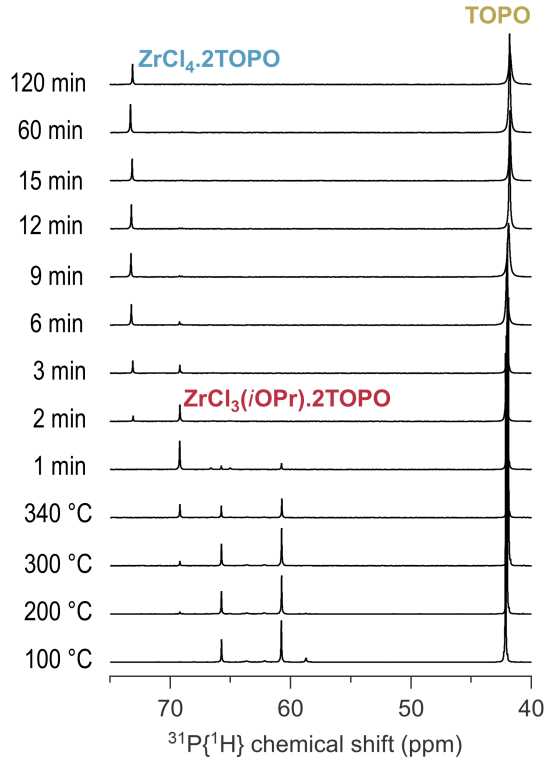

Fig. B.8 | **^{31}P NMR of reaction aliquots.** ^{31}P NMR of aliquotes from 1:1 reaction mixture of $ZrCl_4$: $Zr(O\textit{i}Pr)_4 \cdot \textit{i}PrOH$.

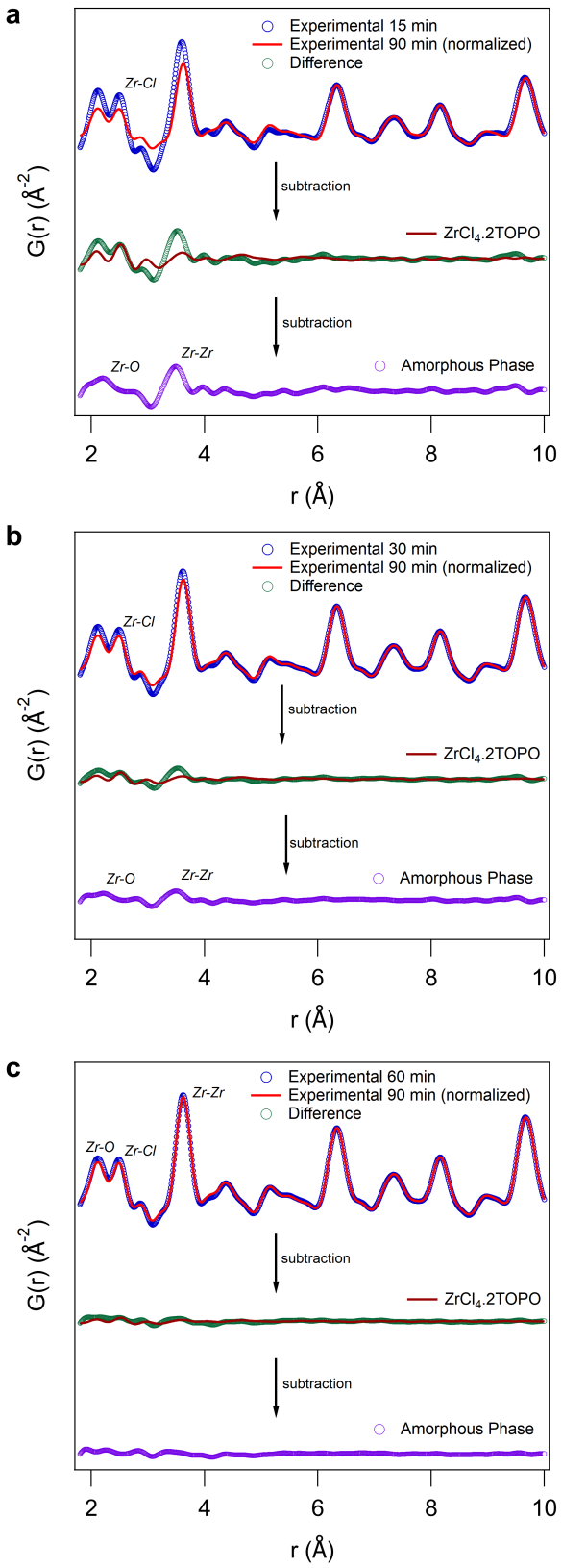

Fig. B.9 | **PDF of amorphous phase.** Extraction of the PDF of amorphous phase after **a** 15, **b** 30, and **c** 60 minutes for $ZrCl_4$: $Zr(O\mathit{i}Pr)_4 \cdot \mathit{i}PrOH$ reaction.

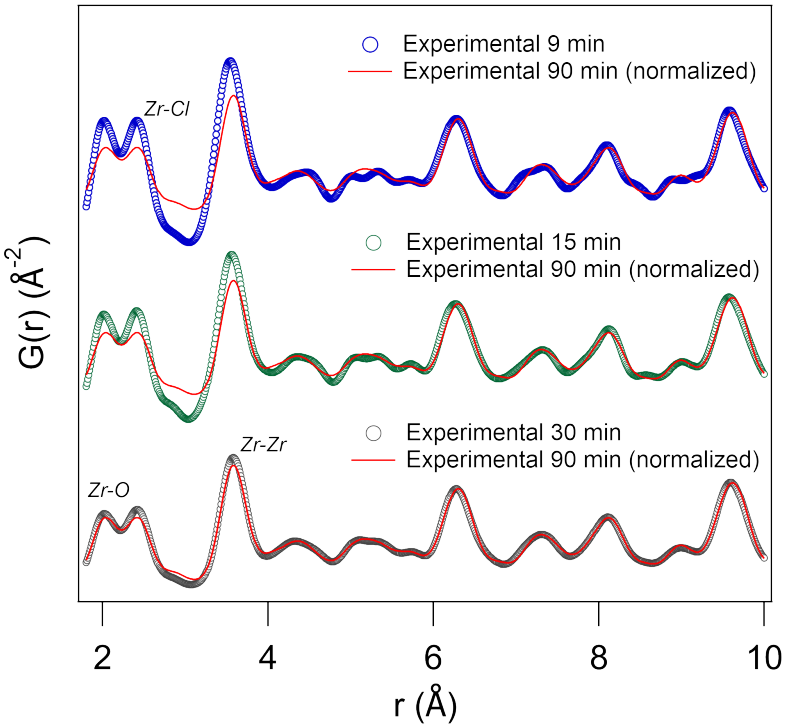

Fig. B.10 | Changes in the contribution of amorphous intermediates captured in situ after 9, 15, and 30 minutes of $ZrCl_4$: $Zr(OiPr)_4 \cdot iPrOH$ reaction. Each data point is normalized with reaction crude product (data point after 90 minutes) by scaling the peak intensity at 6.3 Å. The difference in the PDFs narrows with time, indicating the disappearance of amorphous intermediate. Unlike the *ex situ* data, the complete extraction of the amorphous PDF is not possible due to the unavailability of the experimental PDF of $ZrCl_4 \cdot 2\,TOPO$ under similar conditions.

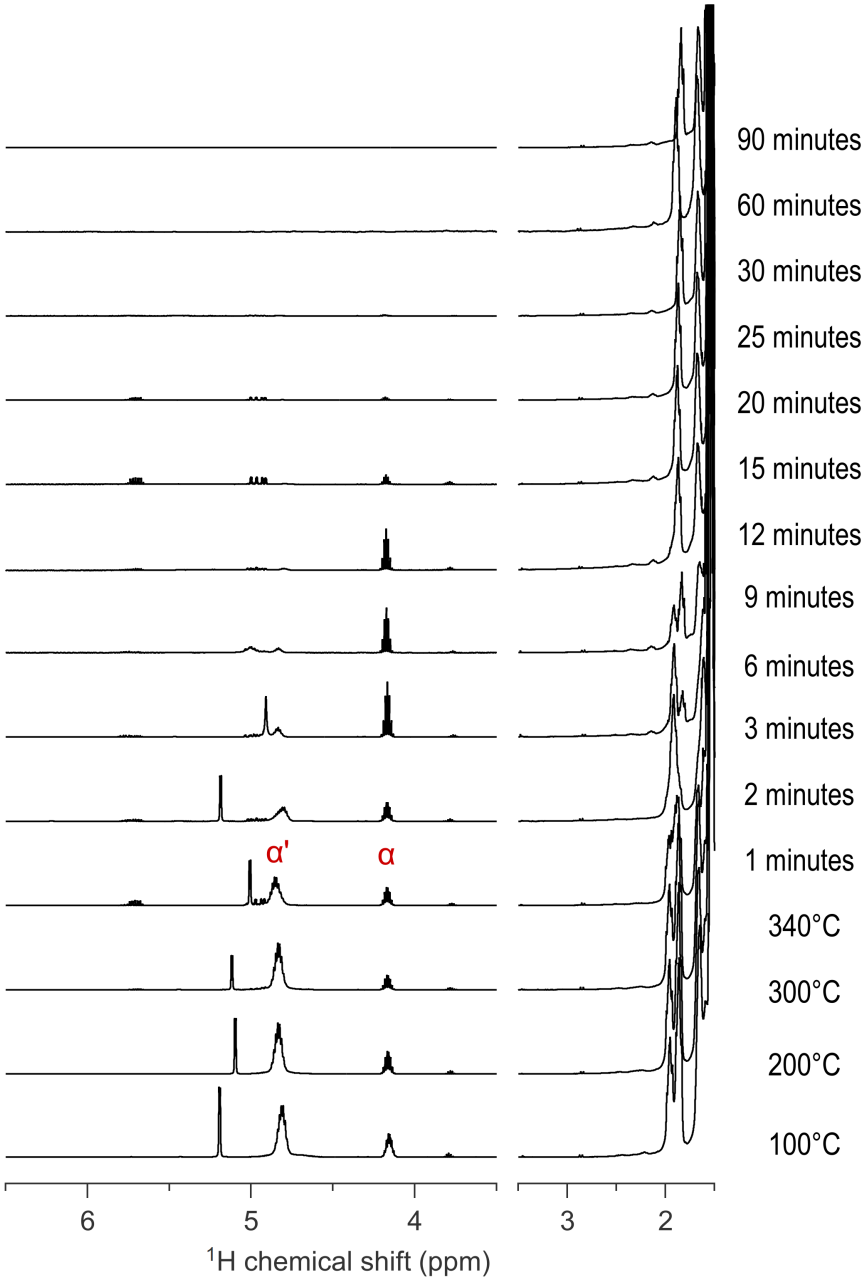

Fig. B.11 | ^{1}H NMR of $ZrCl_4$ reaction aliquots. ^{1}H NMR spectra of the reaction $ZrCl_4$: $Zr(OiPr)_4 \cdot iPrOH$ in C_6D_6. Aliquots were taken at different temperatures during the ramp and at different times at the final reaction temperature of 340 °C. The bound (α') and unbound (α) propoxide groups are indicated. The integral of α' was used for quantification.

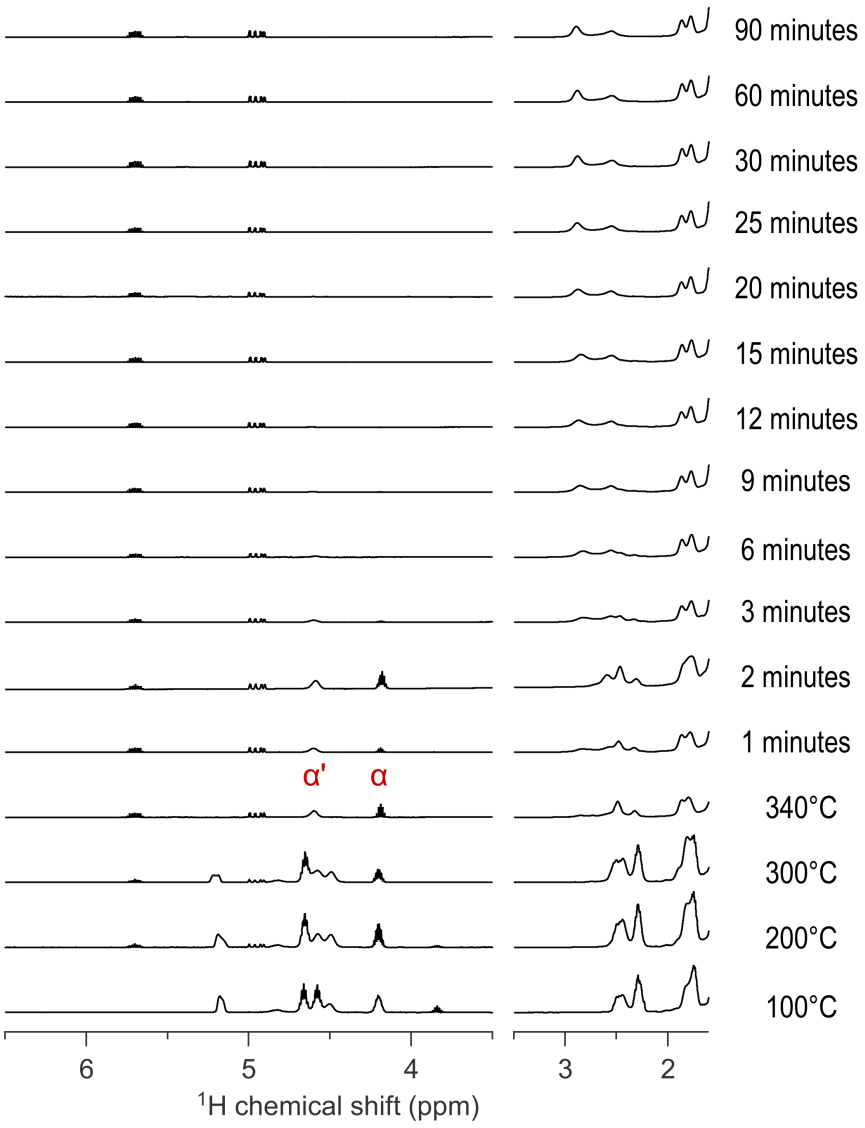

Fig. B.12 | **^{1}H NMR of $ZrBr_4$ reaction aliquots.** ^{1}H NMR spectra of the reaction $ZrBr_4$: $Zr(OiPr)_4 \cdot iPrOH$ in C_6D_6. Aliquots were taken at different temperatures during the ramp and at different times at the final reaction temperature of 340 °C. The bound (α') and unbound (α) propoxide groups are indicated. The integral of α' was used for quantification.

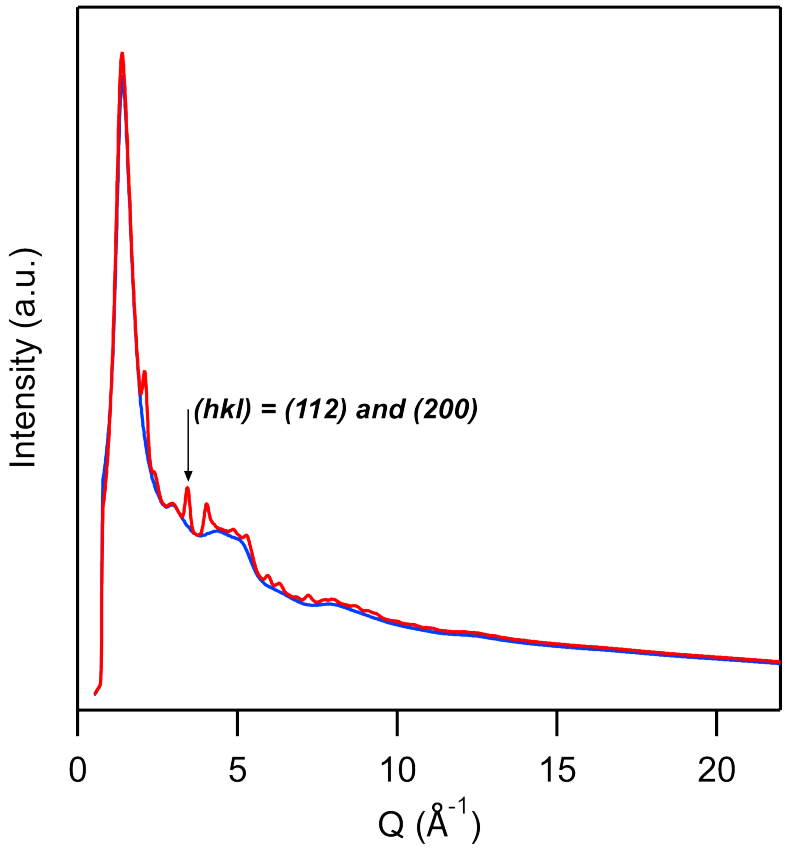

Fig. B.13 | Estimation of area under the Bragg peak for the calculation of crystalline yield. Calculation of area under the Bragg peak by subtracting the background (blue) from the reciprocal data (red). The Miller indices corresponding to the Bragg peak are indicated considering the crystal structure is tetragonal ZrO_2.

B.3 Supplementary Tables: PDF analysis

Table B.1 | Refined PDF parameters for the $ZrCl_4$ reaction. Refined parameters after fitting aliquots from 1:1 reaction mixture of $ZrCl_4$: $Zr(OiPr)_4 \cdot iPrOH$.

Time[min]	scale	psize[Å]	a[Å]	b [Å]	Uiso Zr[Å^2]	Uiso O[Å^2]	Rw	Amplitude	wasyn	λ	ϕ	θ	wsig
0	-	-	-	-	-	-	-	-	-	-	-	-	-
1	-	-	-	-	-	-	-	-	-	-	-	-	-
2	0.27	17.70	3.68	4.98	0.065	0.075	0.72	-	-	-	-	-	-
3	0.21	23.85	3.64	5.12	0.028	0.068	0.53	-	-	-	-	-	-
6	0.14	28.13	3.66	5.09	0.016	0.077	0.34	-	-	-	-	-	-
9	0.12	30.14	3.63	5.21	0.013	0.052	0.16	-	-	-	-	-	-
12	0.18	31.95	3.63	5.21	0.012	0.056	0.13	-	-	-	-	-	-
15	0.22	33.46	3.63	5.22	0.011	0.052	0.12	-	-	-	-	-	-
20	0.28	34.86	3.63	5.22	0.011	0.054	0.10	-	-	-	-	-	-
25	0.34	36.09	3.63	5.22	0.010	0.054	0.09	-	-	-	-	-	-
30	0.41	36.99	3.63	5.23	0.009	0.052	0.09	-	-	-	-	-	-
60	0.56	39.19	3.63	5.23	0.009	0.051	0.08	-	-	-	-	-	-
90	0.54	39.92	3.63	5.23	0.009	0.052	0.08	-	-	-	-	-	-

Table B.2 | Refined PDF parameters for the $ZrBr_4$ reaction. Refined parameters after fitting aliquots from 1:1 reaction mixture of $ZrBr_4$: $Zr(OiPr)_4 \cdot iPrOH$.

Time[min]	scale	psize[Å]	a[Å]	b [Å]	Uiso Zr[Å^2]	Uiso O[Å^2]	Rw	Amplitude	wasyn	λ	ϕ	θ	wsig
0	-	-	-	-	-	-	-	-	-	-	-	-	-
1	0.10	19.28	3.64	5.11	0.018	0.038	0.30	-0.303	1.615	4.837	0.050	5.154	1.899
2	0.12	23.65	3.62	5.20	0.014	0.051	0.25	-0.319	1.31	4.92	0.016	4.83	2.37
3	0.12	24.82	3.62	5.20	0.014	0.050	0.21	-0.455	1.876	4.804	0.064	0.557	2.49
6	0.12	28.29	3.62	5.21	0.011	0.057	0.15	-0.715	2.433	4.702	0.135	-7.468	2.498
9	0.17	30.02	3.62	5.21	0.011	0.061	0.12	-3.744	2.357	4.70	1.193	-20.049	3.462
12	0.18	31.17	3.62	5.21	0.010	0.058	0.12	-0.217	2.497	4.695	1.150	-14.485	2.873
15	0.14	31.55	3.62	5.21	0.010	0.057	0.12	-14.062	2.787	4.619	0.166	-30.887	3.228
20	0.14	32.04	3.62	5.21	0.010	0.057	0.11	-13.528	2.760	4.639	0.162	-30.346	3.234
25	0.15	32.38	3.62	5.21	0.010	0.054	0.11	-12.297	2.804	4.638	0.154	-30.286	3.241
30	0.15	32.54	3.62	5.21	0.010	0.057	0.11	-11.654	2.716	4.648	0.146	-28.363	3.202
60	0.16	33.09	3.62	5.21	0.010	0.055	0.11	-10.797	2.733	4.685	0.137	-28.056	3.186
90	0.19	33.42	3.62	5.21	0.010	0.053	0.11	-8.379	2.681	4.699	0.119	-25.516	3.141

B.4 Supplementary Figures: mechanism fitting

This experimental data in Fig. 3.3b,c was used for fitting in COPASI 4.35.[2] When preparing the date for the program, an x-shift of 0.7 min was given for $ZrCl_4$ and 1 min for $ZrBr_4$ to take the ramping into consideration. One cannot start at time = 0 with a precursor conversion that has already progressed by 80%.

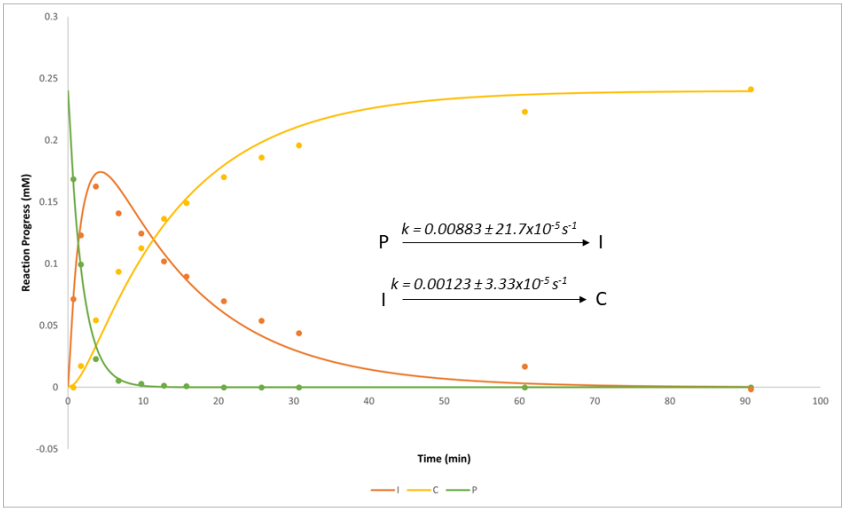

Fig. B.14 | Fitting for $ZrCl_4$: $Zr(OiPr)_4 \cdot iPrOH$ reaction data with mechanism (3). Fitting for the nanocrystal formation using $ZrCl_4$ as the precursor. The root mean square (RMS) value for the fit is 0.00498.

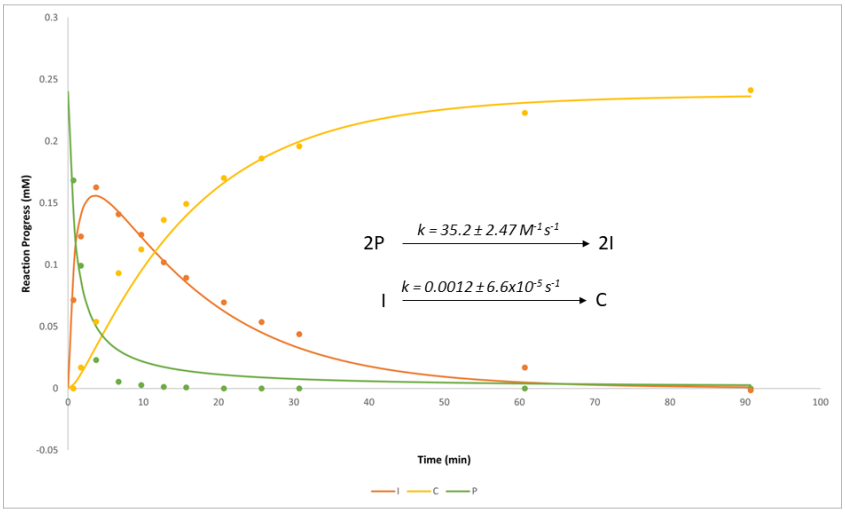

Fig. B.15 | Fitting for $ZrCl_4$: $Zr(OiPr)_4 \cdot iPrOH$ reaction data with mechanism (3) with second-order kinetics in step 1. Fitting for the nanocrystal formation using $ZrCl_4$ as the precursor. The root mean square (RMS) value for the fit is 0.01076.

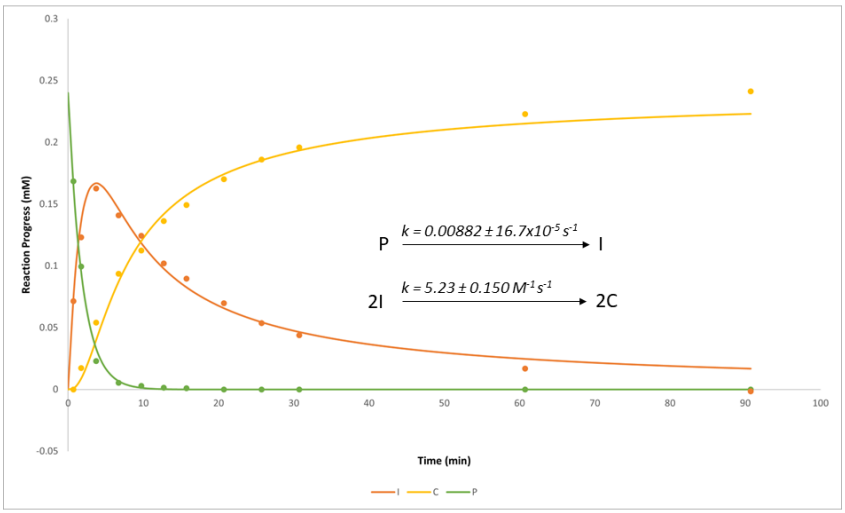

Fig. B.16 | Fitting for $ZrCl_4$: $Zr(OiPr)_4 \cdot iPrOH$ reaction data with mechanism (3) with second-order kinetics in step 2. Fitting for the nanocrystal formation using $ZrCl_4$ as the precursor. The root mean square (RMS) value for the fit is 0.00374.

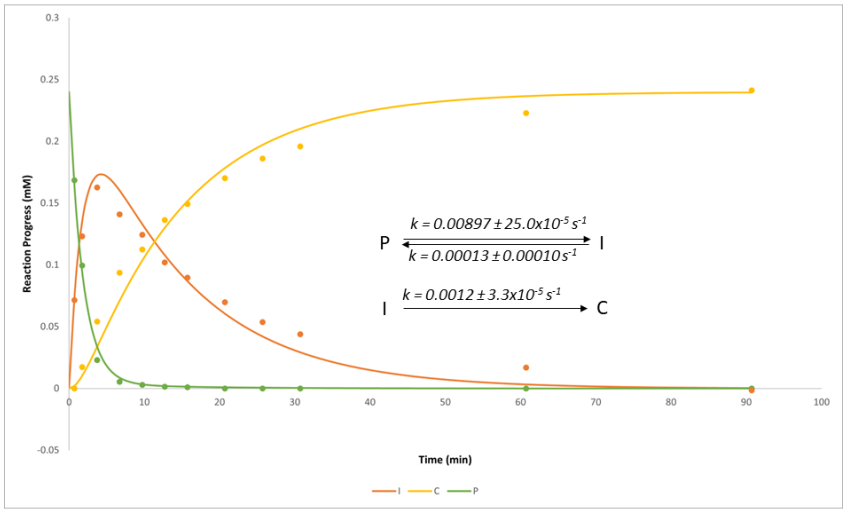

Fig. B.17 | Fitting for $ZrCl_4$: $Zr(OiPr)_4 \cdot iPrOH$ reaction data with mechanism (3) with reversible kinetics in step 1. Fitting for the nanocrystal formation using $ZrCl_4$ as the precursor. The root mean square (RMS) value for the fit is 0.00492.

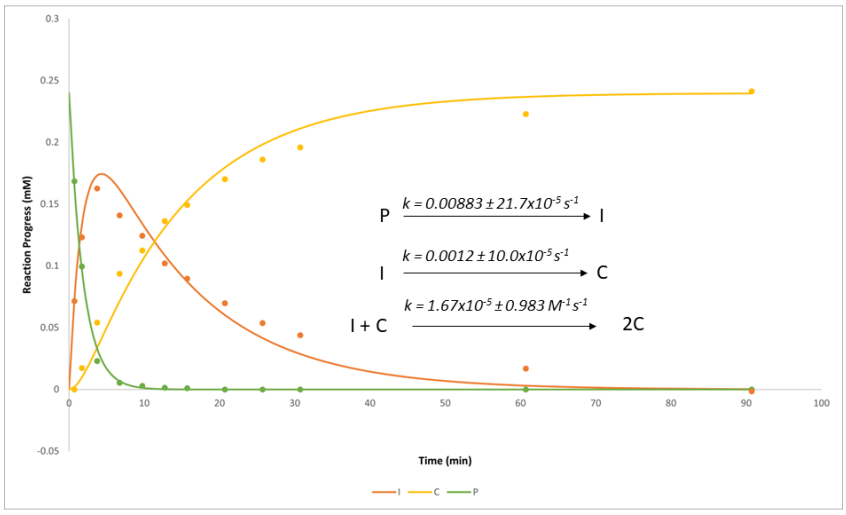

Fig. B.18 | Fitting for $ZrCl_4$: $Zr(OiPr)_4 \cdot iPrOH$ reaction data with mechanism (4) with first-order kinetics in step 2. Fitting for the nanocrystal formation using $ZrCl_4$ as the precursor. The root mean square (RMS) value for the fit is 0.00498.

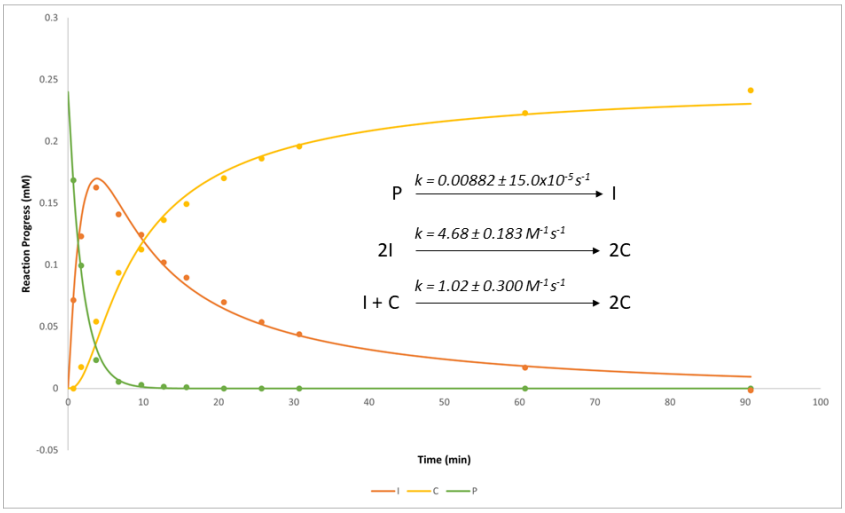

Fig. B.19 | Fitting for $ZrCl_4$: $Zr(OiPr)_4 \cdot iPrOH$ reaction data with mechanism (4). Fitting for the nanocrystal formation using $ZrCl_4$ as the precursor. The root mean square (RMS) value for the fit is 0.00337.

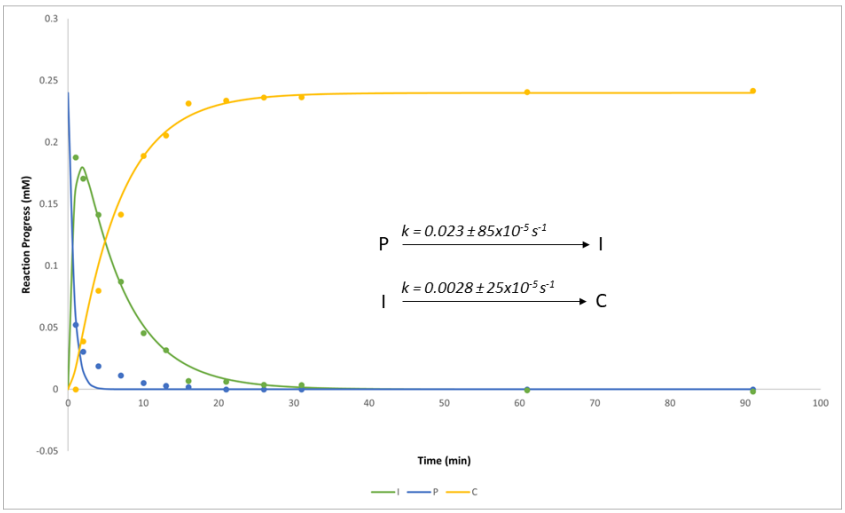

Fig. B.20 | Fitting for $ZrBr_4$: $Zr(OiPr)_4 \cdot iPrOH$ reaction data with mechanism (3). Fitting for the nanocrystal formation using $ZrBr_4$ as the precursor. The root mean square (RMS) value for the fit is 0.00480.

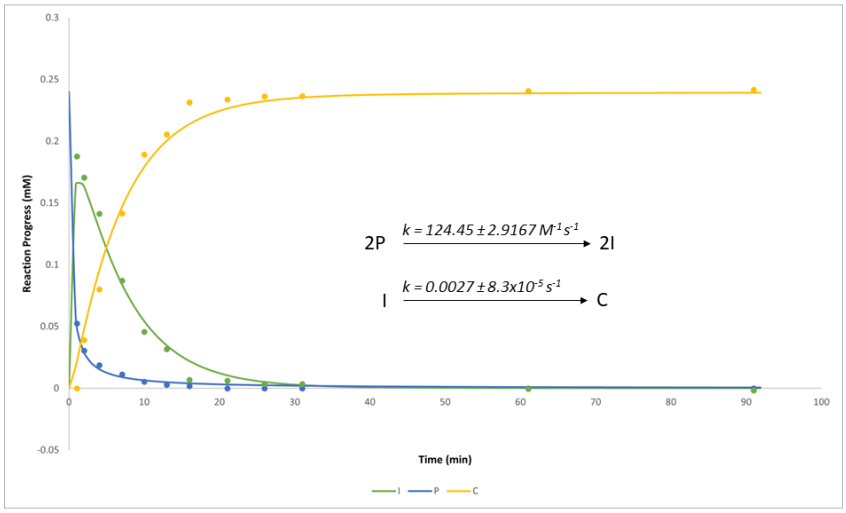

Fig. B.21 | Fitting for $ZrBr_4$: $Zr(OiPr)_4 \cdot iPrOH$ reaction data with mechanism (3) with second-order kinetics in step 1. Fitting for the nanocrystal formation using $ZrBr_4$ as the precursor. The root mean square (RMS) value for the fit is 0.00171.

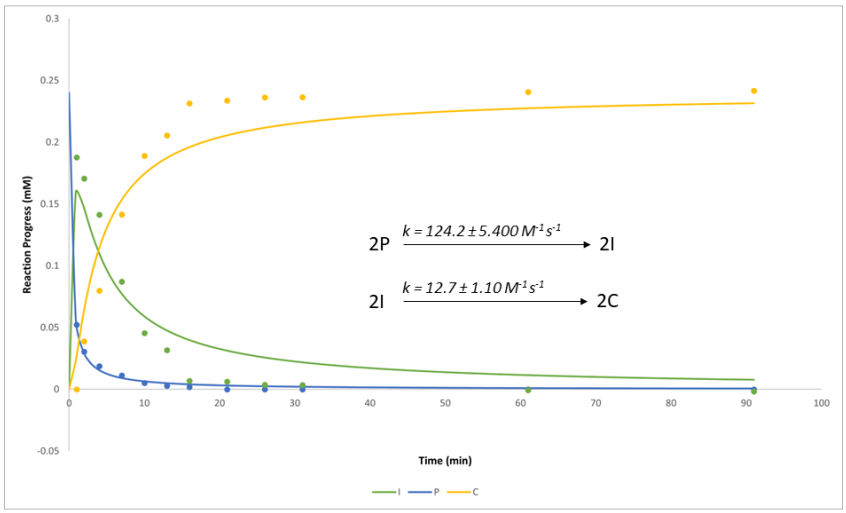

Fig. B.22 | Fitting for $ZrBr_4$: $Zr(OiPr)_4 \cdot iPrOH$ reaction data with mechanism (3) with second-order kinetics in both steps. Fitting for the nanocrystal formation using $ZrBr_4$ as the precursor. The root mean square (RMS) value for the fit is 0.00315.

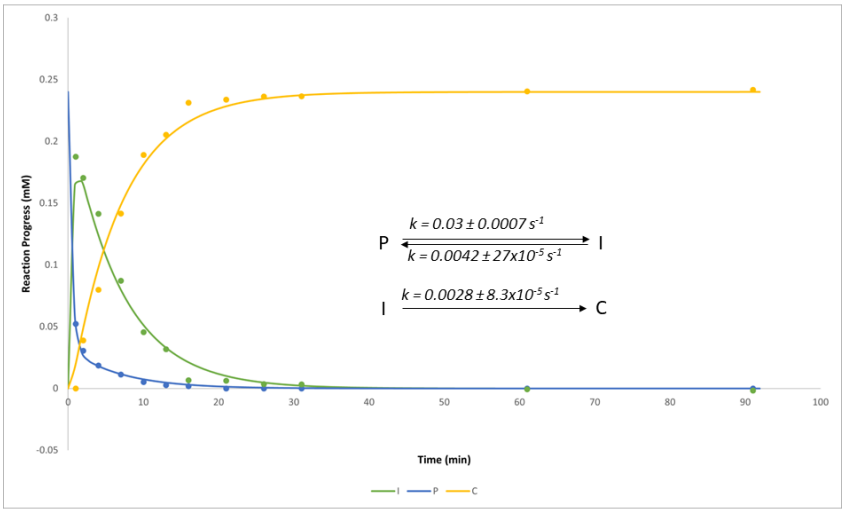

Fig. B.23 | Fitting for $ZrBr_4$: $Zr(OiPr)_4 \cdot iPrOH$ reaction data with mechanism (3) with reversible kinetics in step 1. Fitting for the nanocrystal formation using $ZrBr_4$ as the precursor. The root mean square (RMS) value for the fit is 0.00150.

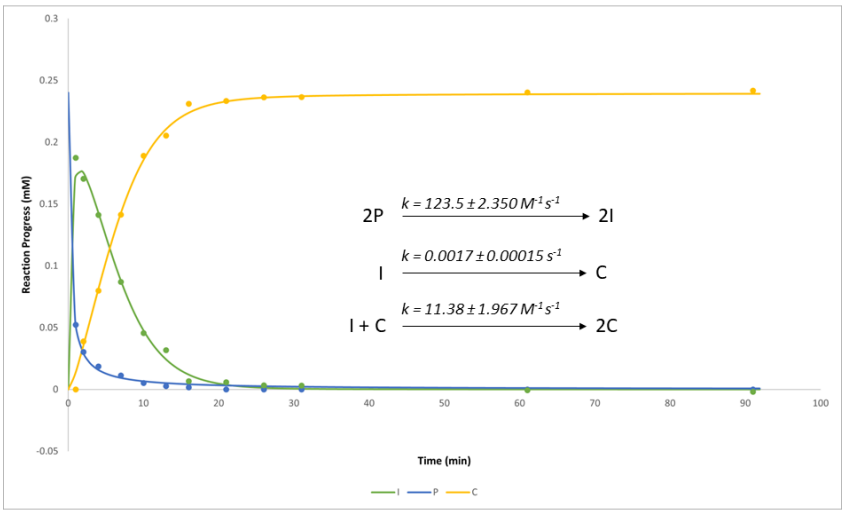

Fig. B.24 | Fitting for $ZrBr_4$: $Zr(OiPr)_4 \cdot iPrOH$ reaction data with mechanism (5) with first-order kinetics in step 1. Fitting for the nanocrystal formation using $ZrBr_4$ as the precursor. The root mean square (RMS) value for the fit is 0.00137.

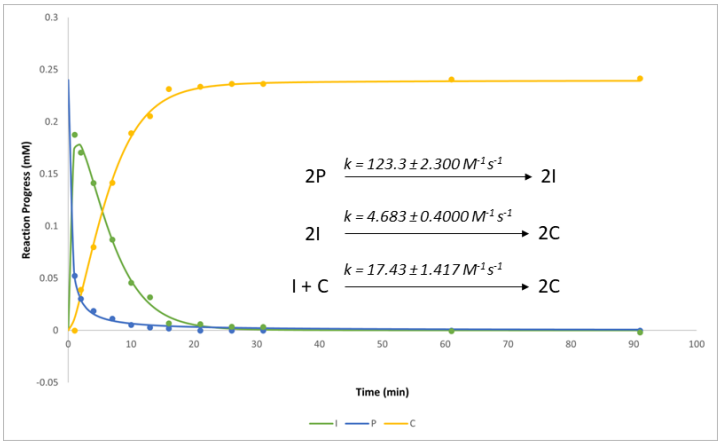

Fig. B.25 | Fitting for $ZrBr_4$: $Zr(OiPr)_4 \cdot iPrOH$ reaction data with mechanism (5). Fitting for the nanocrystal formation using $ZrBr_4$ as the precursor. The root mean square (RMS) value for the fit is 0.00134.

B.5 Supplementary Figures: size tuning

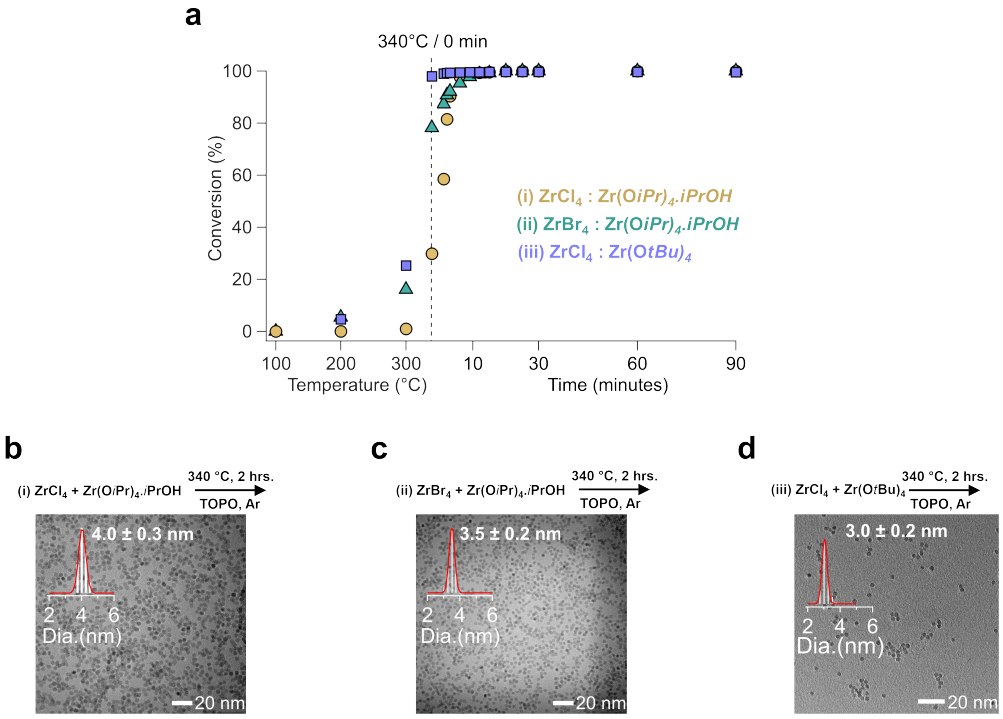

Fig. B.26 | **Correlation between precursor conversion rate and final crystal size. a** The precursor conversion trend in three different precursor combinations. TEM image and histogram of purified nanocrystals from reactions with **b** $ZrCl_4$: $Zr(OiPr)_4 \cdot iPrOH$, **c** $ZrBr_4$: $Zr(OiPr)_4 \cdot iPrOH$ and **d** $ZrCl_4$: $Zr(OtBu)_4$.

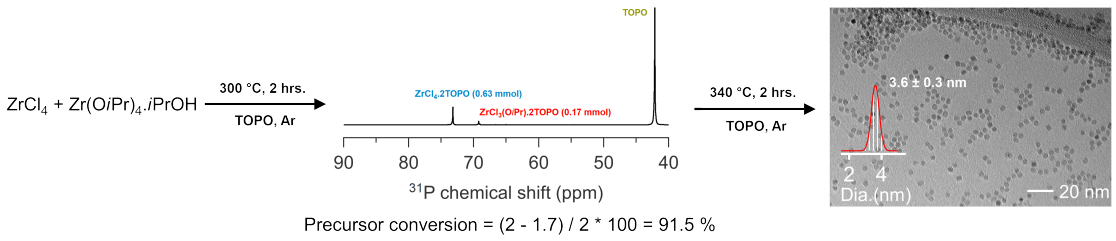

Fig. B.27 | **Modified $ZrCl_4$ reaction to reproduce conditions of faster precursor conversion.** The modified $ZrCl_4$: $Zr(OiPr)_4 \cdot iPrOH$ reaction. The ^{31}P NMR spectrum showing the extent of precursor conversion and TEM image of purified nanocrystals are shown.

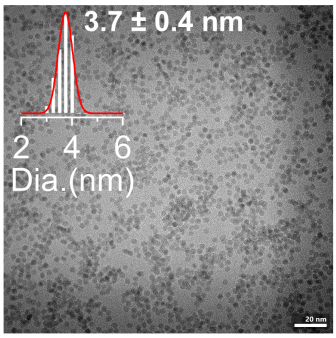

Fig. B.28 | **TEM images of mixed halide reaction.** TEM image and histogram of purified nanocrystals synthesized with a mixture of $ZrCl_4$ and $ZrBr_4$ (keeping the total amount of zirconium halide always constant).

Bibliography

[1] M. Kotlarchyk, R. B. Stephens, and J. S. Huang. Study of Schultz distribution to model polydispersity of microemulsion droplets. *The Journal of Physical Chemistry*, 92(6):1533–1538, 1988.

[2] S. Hoops, S. Sahle, R. Gauges, C. Lee, J. Pahle, N. Simus, M. Singhal, L. Xu, P. Mendes, and U. Kummer. COPASI: a COmplex PAthway SImulator. *Bioinformatics*, 22(24):3067–3074, 2006.

Appendix C

Supplementary Information of Chapter 4

C.1 Supplementary Figures

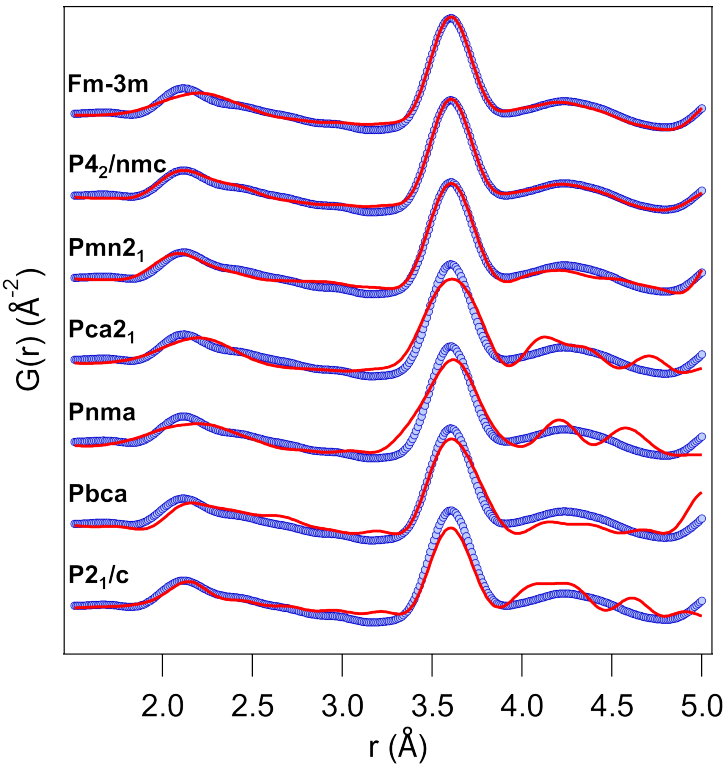

Fig. C.1 | Fitting the local structure of 4 nm ZrO_2 with various models. The spacegroups are indicated and the refined parameters are given in Table C.2.

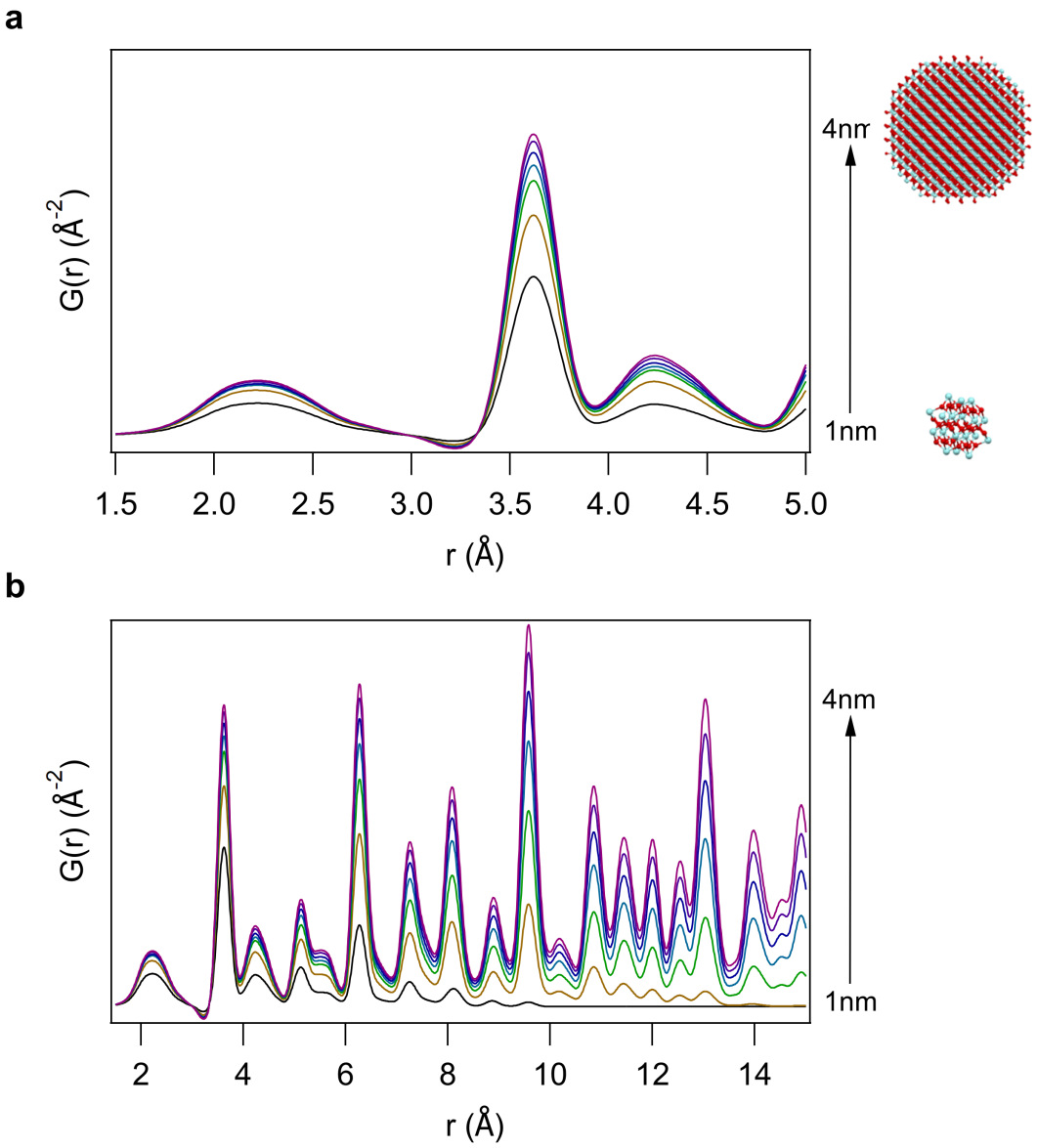

Fig. C.2 | **Simulated PDF of ZrO_2 size series.** **a** Simulated PDF of pure tetragonal nanocrystals of size from 1 nm to 4 nm. **b** The same simulated PDFs with a higher r-range.

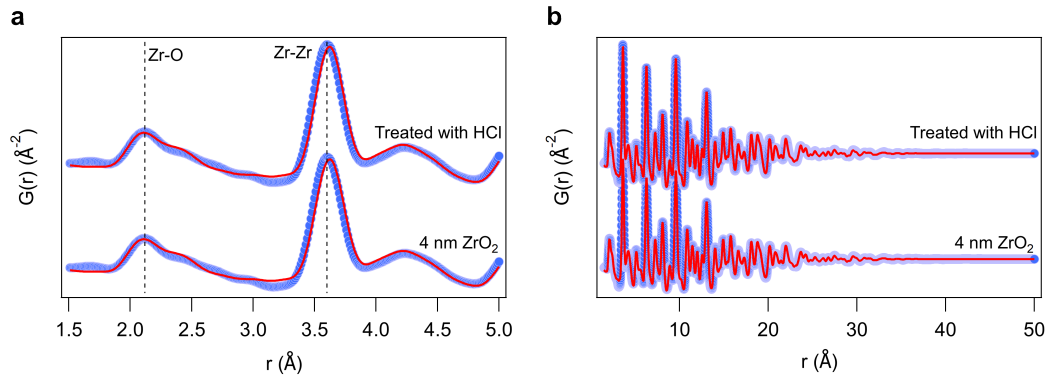

Fig. C.3 | **PDF analysis after surface treatment. a-b** The PDF of 4 nm nanocrystals before and after modifying the surface with HCl.

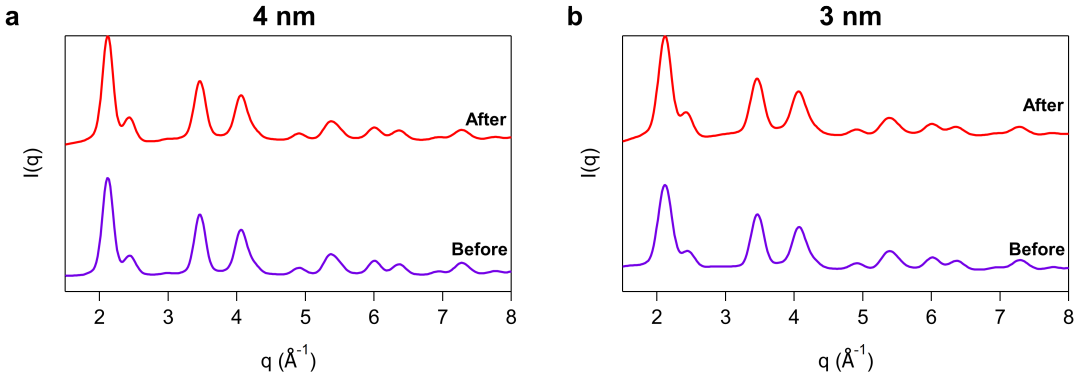

Fig. C.4 | **XRD after heat treatment.** The XRD pattern of **a** 4 nm and **b** 3 nm nanocrystals before and after annealing at 400 °C for 1 hour.

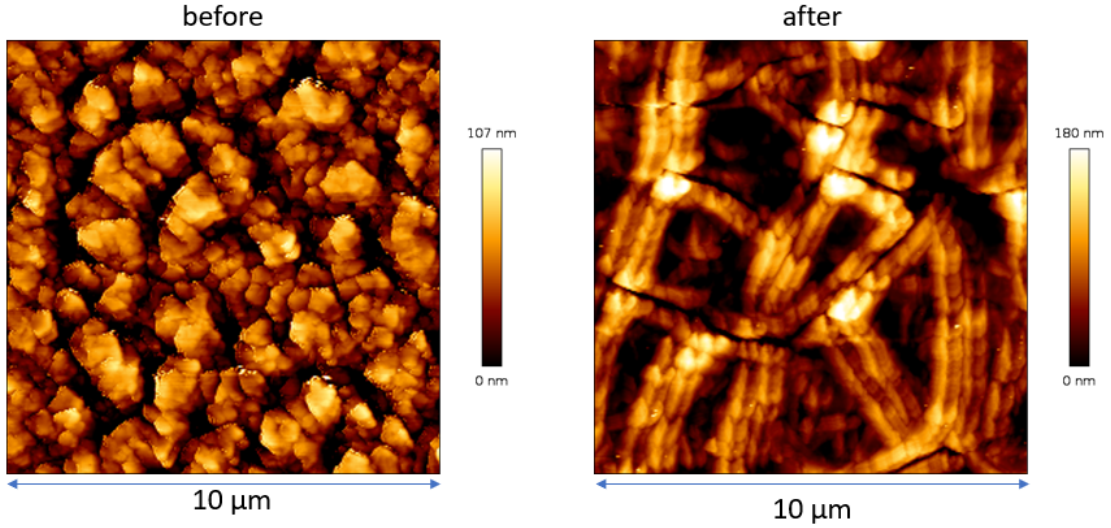

Fig. C.5 | **AFM images.** The AFM images of thin film made by spin coating ZrO_2 nanoparticle solution before and after annealing at 400°C for 1 hour.

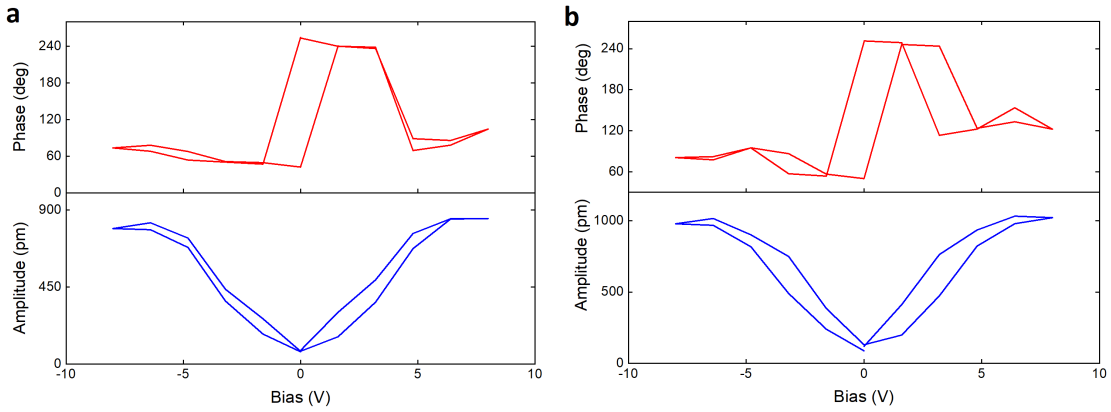

Fig. C.6 | **Hysteresis loop for ZrO_2 nanocrystal thin film.** On state hysteresis loop for **a** 4 nm and **b** 3 nm ZrO_2 nanocrystal thin films.

C.2 Supplementary Tables

Table C.1 | Refined parameters after fitting 4 nm ZrO_2 in various ranges.

Fit range	scale	psize[Å]	a[Å]	b[Å]	Uiso Zr[Å^2]	Uiso O[Å^2]	Rw
1.5-50 Å	0.76	40.15	3.60	5.18	0.008	0.049	0.11
1.5-5 Å	0.74	40.15	3.64	4.99	0.007	0.062	0.10
5-50 Å	0.76	40.15	3.60	5.18	0.008	0.048	0.08

Table C.2 | Refined parameters after fitting the local structure of 4 nm ZrO_2 with various structures.

Spacegroup	scale	psize[Å]	a[Å]	b[Å]	beta[°]	c[Å]	Uiso Zr[Å^2]	Uiso O[Å^2]	Rw
Fm-3m Å	0.74	40.15	5.09	-	-	-	0.007	0.080	0.13
$P4_2$/nmc	0.74	40.15	3.64	-	-	4.99	0.007	0.062	0.10
$Pmn2_1$	0.71	40.15	3.62	5.09	-	3.60	0.004	0.023	0.16
$Pca2_1$	0.95	40.15	4.70	5.35	-	5.55	0.002	0.007	0.30
Pnma	0.74	40.15	3.62	5.99	-	6.18	0.002	0.034	0.35
Pbca	0.99	40.15	5.31	5.71	-	9.18	0.004	0.110	0.35
$P2_1$/c	1	40.15	5.21	5.58	96.60	5.54	0.002	0.851	0.33

Table C.3 | Refined parameters after fitting 4 nm ZrO_2 for the range 1.5 -5 Åusing $P4_2$/nmc and $Pmn2_1$. In addition, Zr atom positions are refined maintaining the symmetry of the spacegroup.

Spacegroup	scale	psize[Å]	a[Å]	b[Å]	c[Å]	Uiso Zr[Å^2]	Uiso O[Å^2]	Rw
$P4_2$/nmc	0.74	40.15	3.64	-	4.98	0.007	0.058	0.09
$Pmn2_1$	0.74	40.15	3.57	5.24	3.54	0.005	0.027	0.08

Table C.4 | Refined parameters after fitting 4 nm ZrO_2 before and after surface treatment with HCl.

	scale	psize[Å]	a[Å]	b[Å]	Uiso Zr[Å^2]	Uiso O[Å^2]	Rw
Before	0.76	40.15	3.60	5.18	0.008	0.049	0.11
After	0.80	40.60	3.60	5.18	0.008	0.049	0.10

Table C.5 | Refined parameters after fitting 4 nm ZrO_2 before and after annealing at 400 °C for 1 hour.

	scale	psize[Å]	a[Å]	b[Å]	Uiso Zr[Å^2]	Uiso O[Å^2]	Rw
Before	0.76	40.15	3.60	5.18	0.008	0.049	0.11
After	0.85	38.09	3.60	5.18	0.011	0.054	0.12

Table C.6 | Refined parameters after fitting 3 nm ZrO_2 before and after annealing at 400 °C for 1 hour.

	scale	psize[Å]	a[Å]	b[Å]	Uiso Zr[Å^2]	Uiso O[Å^2]	Rw
Before	0.71	32.53	3.60	5.17	0.010	0.048	0.14
After	0.86	30.70	3.60	5.17	0.014	0.054	0.16

Appendix D

Scientific Output

D.1 Publications in peer-reviewed journals

1. An Amorphous Phase Precedes Crystallization: Unraveling the Colloidal Synthesis of Zirconium Oxide Nanocrystals. **Rohan Pokratath**, Lermusiaux Laurent, Jikson Pulparayil Mathew, Stefano Checchia, Susan Rudd Cooper, Jette Katja Mathiesen, Guillaume Landaburu, Soham Banarjee, Songsheng Tao, Nico Reichholf, Simon J. L. Billinge, Benjamin Abécassis, Kirsten M. Ø. Jensen, Jonathan De Roo*; **ACS Nano**, **2023**, 17(9), 8796-8806, 10.1021/acsnano.3c02149.

2. Mechanistic Insight into the Precursor Chemistry of ZrO_2 and HfO_2 Nanocrystals; towards Size-Tunable Syntheses. **Rohan Pokratath**, Dietger Van den Eynden, Susan Rudd Cooper, Jette Katja Mathiesen, Valérie Waser, Mike Devereux, Simon J. L. Billinge, Markus Meuwly, Kirsten M. Ø. Jensen, Jonathan De Roo*; **JACS Au, 2022**, 2, 4, 827-838, 10.1021/jacsau.1c00568.

3. Nonaqueous Chemistry of Colloidal Group 4 Oxo Clusters and Metal Oxide Nanocrystals. Dietger Van den Eynden, **Rohan Pokratath**, Jonathan De Roo*; **Chemical Reviews, 2022**, 122, 11, 10538–10572, 10.1021/acs. chemrev.1c01008.

4. Monoalkyl Phosphinic Acids as Ligands in Nanocrystal Synthesis. Evert Dhaene, **Pokratath, Rohan**, Olivia Aalling-Frederiksen, Kirsten M. Ø. Jensen, Smet, P. F., Klaartje De Buysser, Jonathan De Roo*; **ACS Nano, 2022**, 16, 5, 7361–7372, 10.1021/acsnano.1c08966.

5. The Chemistry of Cu_3N and Cu_3PdN Nanocrystals. Mahsa Parvizian, Alejandra Duràn Balsa, **Rohan Pokratath**, Curran Kalha, Seungho Lee, Dietger Van den Eynden, Maria Ibáñez, Anna Regoutz, Jonathan De Roo; **Angewandte Chemie International Edition, 2022**, 61, e2022070,

10.1002/anie.202207013.

6. Mapping out the Aqueous Surface Chemistry of Metal Oxide Nanocrystals: Carboxylate, Phosphonate, and Catecholate Ligands. Loren Deblock, Eline Goossens, **Rohan Pokratath**, Klaartje De Buysser, Jonathan De Roo*; **JACS Au, 2022**, 2, 711-722, 10.1021/jacsau.1c00565.

7. Fatty Acid Capped, Metal Oxo Clusters as the Smallest Conceivable Nanocrystal Prototypes. Dietger Van den Eynden, **Rohan Pokratath**, Jikson Pulparayil Mathew, Eline Goossens, Klaartje De Buysser, Jonathan De Roo*; **Chemical Science, 2022**, 10.1039/D2SC05037D.

8. Ligand Conversion in Nanocrystal Synthesis: The Oxidation of Alkylamines to Fatty Acids by Nitrate. Mariano Calcabrini, Dietger Van den Eynden, Sergi Sánchez Ribot, **Rohan Pokratath**, Jordi Llorca, Jonathan De Roo*, Maria Ibáñez*; **JACS Au, 2021**, 1, 1898-1903, 10.1021/jacsau.1c00349.

9. Local Structure Distortion and Origin of Local Diploe in Nanoscale Zirconia. **Rohan Pokratath**, Kumara Cordero-Edwards, Ajmal Roshan Unniram Parambil, Simon J. L. Billinge, Gustau Catalan, Jonathan De Roo*; **in preparation**

10. Lewis Acid-Base Chemistry in the Group 4: Complexation and Disproportionation of Metal Alkoxy Halides. Carlotta Seno, **Rohan Pokratath**, Dietger Van den Eynden, Alessandro Prescimone, Jonathan De Roo*; **in preparation**

11. Surface chemistry of zirconium and hafnium metal oxo clusters. Ajmal Roshan Unniram Parambil, **Rohan Pokratath**, Evert Dhaene, Dietger Van den Eynden, Alessandro Prescimone, Patrick Shahgaldian, Jonathan De Roo*; **in preparation**

12. Adapting the Synthesis of Tuneable Metal-oxo Clusters for Catalysis of Peptide Bond Hydrolysis. Kilian Declerck, Nada D. Savic, Angelo Mullaliu, Mhamad Aly Moussawi, Carlotta Seno, **Rohan Pokratath**, Jonathan De Roo, Tatjana N. Parac-Vogt*; **in preparation**

13. A Parametric Approach to Unravelling the Bifunctionality of Capping Agents in Bimetallic Nanoparticle Syntheses. Jette K. Mathiesen, Hannah M. Ashberry, **Rohan Pokratath**, Jocelyn T. L. Gamler, Baiyu Wang, Andrea Kirsch, Emil T. S. Kjær, Soham Banerjee, Jonathan De Roo, Kirsten M. Ø. Jensen*, Sara E. Skrabalak*; **in preparation**

14. Nonaqueous Formation Mechanism of Zirconium and Hafnium Oxo Clusters. Dietger Van

den Eynden, Angelo Mullaliu, Carlotta Seno, Jikson Pulparayil Mathew, **Rohan Pokratath**, Christopher B. Whitehead, Adam Hugh Clark, Olga Safonova, Tatjana N. Parac-Vogt, Jonathan De Roo*; **in preparation**

D.2 Awards

1. **Travel Award**: Swiss Society of Crystallography (SSCr) Travel Award, 2023.
2. **Travel Award**: Royal Society of Chemistry (RSC) Researcher Development and Travel Grant, 2023.
3. **Travel Award**: Rideal Travel Bursary Award, 2023.
4. **Travel Award**: European Chemical Society (EuChemS) Travel Grant, 2022.
5. **Best Poster Award**: 8^{th} European Chemical Society (EuChemS) Chemistry Congress (ECC8), Lisbon, 2022.
6. **Best Poster Award**: Internet NanoGe Conference on Nanocrystals (iNCNC), 2021.